**Analytical Framework for Evaluating Wind Hazard Vulnerability of Light Wood-Frame Buildings**

by

Brandon Michael Rittelmeyer

A dissertation submitted to the Graduate Faculty of
Auburn University
in partial fulfillment of the
requirements for the Degree of
Doctor of Philosophy

Auburn, Alabama
August 9, 2025



Approved by

David B. Roueche, Chair, Gottlieb Associate Professor of Structural Engineering
Robert W. Barnes, Arthur H. Feagin Chair Professor of Structural Engineering
James S. Davidson, Professor of Structural Engineering
Matthew T. Yarnold, Associate Professor of Structural Engineering

Abstract

Light wood-frame construction constitutes most of the residential building inventory in the United States. The vulnerability of wood-frame buildings to wind hazards and a wide variability in observed performance have motivated research efforts toward understanding precisely how and why wood-frame structural failures occur and how wind damage can be effectively and economically mitigated in future events. Probabilistic analysis of wind performance has been an important strand within these efforts. The wind performance of a structure is essentially a function of structural resistance and wind load intensity, with sources of epistemic and stochastic uncertainty present in both resistance and load. This dissertation aims at a systematic examination of structural and aerodynamic factors that contribute uncertainty to wood-frame wind performance. The analysis framework is composed of two complementary models. (1) A structural vulnerability model evaluates wind uplift resistance by a Monte Carlo method in which probability distributions are assigned to factors like framing member spacing, wood species, and fastener measurements. (2) An aerodynamic vulnerability model, composed of regression neural networks trained on wind tunnel data, evaluates wind uplift intensity in terms of factors like roof shape, roof slope, and wind direction. Separately, these models provide a rational basis for comparing (1) system-level resistance across different wood-frame load paths and (2) expected wind uplift intensities across different low-rise geometries. The third element of the framework is a sensitivity analysis that operates on the models independently — to examine how structural and aerodynamic factors respectively influence resistance and load — as well as on a combined model that allows uncertainty in wind performance to be traced back to fundamental building characteristics. The framework lends itself to a range of applications, including wind-resistant design and wind speed estimation.

Acknowledgments

Much of the work presented in this dissertation was sponsored by the National Science Foundation under research grant CMMI-1944149. I am grateful to my advisor, Dr. David Roueche, for entrusting this work to me and offering me the guidance and encouragement I needed throughout my studies. I also thank my committee — Dr. Robert Barnes, Dr. Jim Davidson, and Dr. Matthew Yarnold — whose questions and recommendations helped to refine my own thinking and strengthened this dissertation. My time at Auburn University has been a great gift.

I would also like to thank my parents and my sister Rebecca for their love and constant support during these years of study. I could not have done this without them. And I am deeply thankful for my friends at Lakeview Baptist Church in Auburn — too many to name — who followed my progress with excitement and continually encouraged me in the Lord all along the way.

*Soli Deo Gloria*

Table of Contents

Abstract . . . . . 2

Acknowledgments . . . . . 3

List of Tables . . . . . 6

List of Figures . . . . . 7

**1 Introduction** . . . . . 9

**2 Evaluating Wind Resistance in Wood-Frame Structural Load Paths** . . 15

2.1 Analysis Method . . . . . 16

2.1.1 Connection Capacities . . . . . 18

2.1.2 Evaluating System Resistance . . . . . 24

2.2 Comparison to Experimental Capacities . . . . . 27

2.2.1 Roof Sheathing . . . . . 27

2.2.2 Roof-to-Wall Connections . . . . . 29

2.2.3 Wall-to-Slab Connections . . . . . 32

2.3 Resistance Model Results . . . . . 33

2.3.1 Comparison to Experimental System-Level Resistance . . . . . 34

2.3.2 Analysis of Archetype A . . . . . 36

2.3.3 Analysis of Archetype B . . . . . 38

2.3.4 Field Study Examples . . . . . 40

2.4 Summary and Applications . . . . . 43

**3 Indexing Aerodynamic Vulnerability in Low-Rise Buildings** . . . . . 46

3.1 Analysis Method . . . . . 49

3.1.1 Defining Building Geometry and Identifying Upwind Sections 49

3.1.2 Wind Tunnel Databases . . . . . 52

3.1.3 Pressure Prediction . . . . . 54
3.1.4 Spatial Averaging and Indexing Approaches . . . . . 70
3.2 Comparison to Design Values . . . . . 72
3.3 Analysis Results . . . . . 75
3.3.1 Parameter Dependence . . . . . 79
3.3.2 Vulnerability Indexes . . . . . 83
3.4 Comparison to Wind Tunnel Studies . . . . . 85
3.5 Summary . . . . . 87

**4 Sensitivity Analysis of Structural and Aerodynamic Vulnerability** . . . 90
4.1 Variance-Based Sensitivity Analysis . . . . . 92
4.2 Analysis of Structural Factors . . . . . 94
4.2.1 Roof Sheathing Resistance . . . . . 95
4.2.2 Roof-to-Wall Connection Resistance . . . . . 98
4.2.3 System Resistance . . . . . 100
4.3 Analysis of Aerodynamic Factors . . . . . 103
4.3.1 Analysis Conditioned on Wind Direction . . . . . 107
4.3.2 Unconditioned Analysis . . . . . 109
4.4 Analysis of Wind Performance . . . . . 112
4.4.1 Roof Sheathing Performance . . . . . 114
4.4.2 Roof-to-Wall Connection Performance . . . . . 116
4.4.3 System Performance . . . . . 119
4.5 Summary . . . . . 121

**5 Concluding Summary** . . . . . 123

References . . . . . 128

List of Tables

1.1 EF Scale Degrees of Damage: One and Two-Family Residences . . . . 11

2.1 Comparison to Roof Sheathing Uplift Tests . . . . . 28
2.2 Roof Sheathing Comparison: Correlation Coefficients . . . . . 29
2.3 Comparison to Toe-Nailed Connection Uplift Tests . . . . . 30
2.4 Comparison to Hurricane Tie Uplift Tests . . . . . 31
2.5 Concrete Anchorage Capacities . . . . . 33

3.1 Aerodynamic Database Cases: No Eaves . . . . . 52
3.2 Aerodynamic Database Cases: Varied Eaves . . . . . 53
3.3 Regression Models . . . . . 55
3.4 Regression Model Training Summary . . . . . 60
3.5 Robustness of Optimized Hyperparameter Combinations . . . . . 65
3.6 Example Building Geometries . . . . . 75
3.7 Suggested Vulnerability Indexes . . . . . 85

4.1 Roof Sheathing Parameters: Normal Distributions . . . . . 95
4.2 Roof-to-Wall Parameters: Normal Distributions . . . . . 98
4.3 Probabilistic Wind Load Parameters . . . . . 112

List of Figures

1.1 EF Scale Degrees of Damage: One and Two-Family Residences . . . . 12

2.1 Structural Load Path Archetypes . . . . . 17
2.2 Load Path Failures . . . . . 18
2.3 Comparison to Load Path Uplift Tests . . . . . 35
2.4 Analysis of Archetype A . . . . . 37
2.5 Analysis of Archetype B . . . . . 39
2.6 Case Study: Lake Charles, Louisiana . . . . . 42
2.7 Case Study: Cookeville, Tennessee . . . . . 43

3.1 Aerodynamic Vulnerability Analysis Procedure . . . . . 50
3.2 Upwind Roof Sections . . . . . 51
3.3 Building Geometry Definitions . . . . . 54
3.4 Regression Model Generalization Curves . . . . . 63
3.5 Gable Roof Surface-Averaged $C_p(\theta)$ . . . . . 66
3.6 Hip Roof Surface-Averaged $C_p(\theta)$ . . . . . 67
3.7 Surface-Averaged $C_p(\theta)$ for Roof Overhangs . . . . . 68
3.8 Pressure Contour Development . . . . . 69
3.9 Comparing Roof Sheathing Predicted $C_p$ to Design $GC_p$ . . . . . 74
3.10 Gable Roof $\bar{C}_p(\theta)$ Predictions . . . . . 76
3.11 Hip and Gable-Hip Roof $\bar{C}_p(\theta)$ Predictions . . . . . 77
3.12 Dependence of $\bar{C}_p(\theta)$ on Roof Slope and Eave Height . . . . . 80
3.13 Roof Overhang Depth Effects . . . . . 81
3.14 Summary of Predicted Uplift Intensity Distributions . . . . . 84
3.15 Predictions Compared to Wind Tunnel Tests of Irregular Buildings . 86

4.1 Sensitivity Analysis of Roof Sheathing Resistance . . . . . 97
4.2 Sensitivity Analysis of Roof-to-Wall Resistance . . . . . 99
4.3 Sensitivity Analysis of System Resistance . . . . . 102
4.4 Roof Structure $\bar{C}_p(\theta)$ Profiles . . . . . 105
4.5 Roof Sheathing $\bar{C}_p(\theta)$ Profiles . . . . . 106
4.6 Sensitivity Analysis of $\bar{C}_p$ Conditioned on Wind Direction . . . . . 108
4.7 Unconditioned Sensitivity Analysis of $\bar{C}_p$ . . . . . 111
4.8 Fragility Function Development . . . . . 113
4.9 Sensitivity Analysis of Roof Sheathing Performance . . . . . 115
4.10 Sensitivity Analysis of Roof-to-Wall Performance . . . . . 117
4.11 Sensitivity Analysis of System Performance . . . . . 120

# Chapter 1

## Introduction

Residential construction in the United States is primarily light wood-frame, encompassing more than 90% of single-family homes and more than 70% of multi-family homes according to construction survey data. [1] The prevalence of light wood-frame construction in every region of the country means that the performance limits of wood-frame structures are routinely tested by all manner of natural hazards, not least by wind hazards. The combined annual cost of severe storms and tropical cyclones is estimated by the National Centers for Environmental Information to be $46.2 billion. [2] High winds are a principal cause of damage in these events, though other hazards, especially flooding and storm surge, are also reflected in this annual cost estimate. It is difficult to determine the cost associated strictly with high winds, in part because structures often sustain damage from multiple hazards in the same event, but the NCEI events dataset offers a broad sense of the cost of wind damage. For example, the dataset includes more than forty severe storms involving tornado outbreaks between 2020 and 2024. Each of these storms caused at least $1.1 billion in damage, and the total estimated cost of these events surpasses $140 billion. This figure does not include the cost of damage associated with more than twenty tropical cyclones during the same period.

The vulnerability of wood-frame structures to high winds is well known. The events noted above furnish abundant evidence of the wind damage that residential

[1] Percentages are from the annual characteristics tables for framing available at `census.gov`.

[2] Cost data are available at `ncei.noaa.gov`. The annual cost estimate is for events between 1980 and 2024 that are believed to have caused at least $1 billion in damage. All dollar amounts in this discussion include inflation adjustment to 2025.

buildings are liable to sustain. Henderson *et al.* (2021), to take one example, document structural failures observed after the Putnam County, Tennessee tornado of March 3, 2020, which destroyed more than thirty homes. Damage observations from this event and other recent hurricanes and tornadoes have been compiled into a unified wind performance dataset by Roueche *et al.* (2024). Because of its frequent occurrence, residential structure damage is often used to assign intensity ratings to tornadoes using the Enhanced Fujita scale. The EF scale method provides a descriptive list of degrees of damage for twenty-eight damage indicators. Each degree of damage is associated with a range of three-second wind speeds determined according to expert judgment. The degrees of damage applicable to one and two-family residences are summarized in Table 1.1, and Figure 1.1 plots the corresponding expected and upper and lower-bound wind speeds. Field personnel first identify the degree of damage that most closely matches the observations and subsequently select a wind speed from the associated range; evidence of strong construction may justify a wind speed estimate above the expected value, while structural defects or unfavorable aerodynamic characteristics like large roof overhangs warrant a lower estimate. [3] The selected wind speed determines the tornado EF rating. The EF scale method illustrates the two areas of primary concern to the present work, which are also two principal aims of the wind engineering discipline more broadly, namely:

1. *Damage mitigation:* what steps can be taken to move the failure wind speed of a structure effectively toward the upper bound? Or equivalently, how can the expected failure wind speed be raised across all degrees of damage?

[3] See "A Recommendation for an Enhanced Fujita Scale" (2006), p. 9.

**Table 1.1.** EF Scale Degrees of Damage for One and Two-Family Residences

| | |
|---|---|
| 1 | Threshold of visible damage. |
| 2 | Loss of $< 20\%$ of roof covering material; loss of vinyl or metal siding. |
| 3 | Broken glass in doors and windows. |
| 4 | Uplift of roof deck and loss of $> 20\%$ of roof covering material. |
| 5 | Entire house shifts off foundation. |
| 6 | Large sections of roof structure removed; most walls remain standing. |
| 7 | Exterior walls collapsed. |
| 8 | Most walls collapsed, except small interior rooms. |
| 9 | All walls collapsed. |
| 10 | Destruction of engineered or well-constructed residence; slab swept clean. |

2. *Wind intensity estimation:* how can the true failure wind speed be most precisely determined from post-event observations? Or equivalently, how can the margin between the upper and lower bound wind speeds be most effectively reduced?

The equivalent motivating question in each of these points imagines that the wind speed curves in Figure 1.1, which apply to a wide array of residences, are updated for a specific residence as field data are collected.

*Probabilistic Analysis*

Probabilistic models of wind performance have been a central means of addressing the questions stated above, beginning especially with the work of Ellingwood and Tekie (1999). The landscape of probabilistic studies of light wood-frame structures includes component-level analyses of roof sheathing performance as in Lee and Rosowsky (2005) and uncorrelated performance of roof sheathing and roof-to-wall connections as in Rosowsky and Cheng (1999), Ellingwood *et al.* (2004), and Standohar-Alfano and van de Lindt (2016). System-level analyses of partial load path models composed of roof sheathing and roof-to-wall connections have been carried out by van de Lindt and Dao (2009) in terms of building performance expectations, as well as by Amini and van de

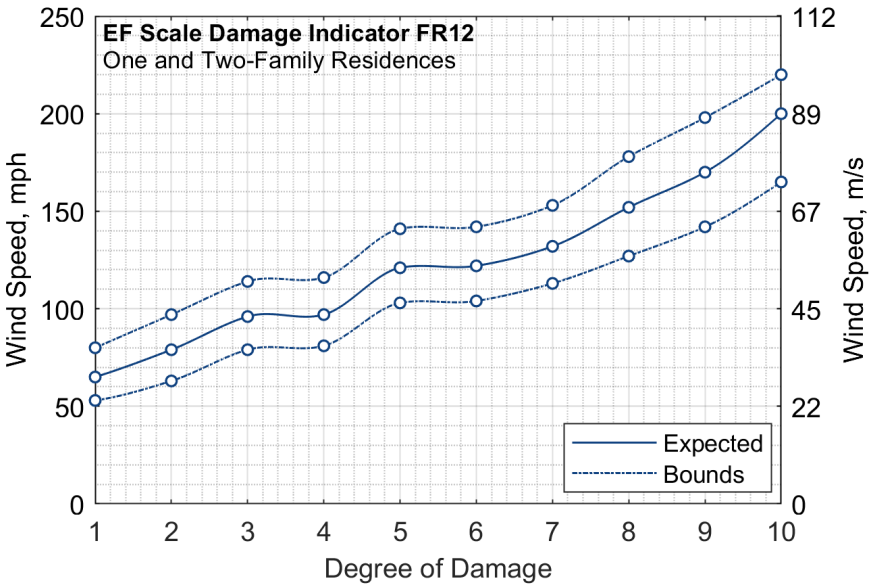


**Figure 1.1.** Wind speeds corresponding to the degrees of damage defined in Table 1.1 for one and two-family residences. Wind speeds are from McDonald *et al.* (2009).

Lindt (2014) and Masoomi *et al.* (2018) on the basis of combined fragility functions for various damage states. Standohar-Alfano *et al.* (2017) have also conducted a failure-event tree analysis of roof sheathing, roof-to-wall, and wall-to-foundation connections as a series system. The common features of these studies are:

($a$) Structural resistance models are developed from representative experimental tests, such as the uplift tests of Mizzell (1994) for roof substrate and Reed *et al.* (1997) for roof-to-wall connections.

($b$) Wind pressure models are developed from ASCE 7 design load provisions, either Chapter 27 for framing loads or Chapter 30 for roof substrate loads. The studies follow the approach of Ellingwood and Tekie to define the nominal ASCE 7 wind load parameters as random variables. External pressure coefficients $C_p$ are based on one or a few specific building archetypes.

Beyond this conventional approach, other studies have adopted connection resistance models that account for nonlinear load-displacement behavior, as Guha and Kopp

(2014) and Enajar *et al.* (2023) have done for roof-to-wall toe nails, for example. Fusco and Zhu (2023) have developed a system-level finite-element model to evaluate wind performance in terms of roof and wall sheathing removal and compressive failure of roof framing members. Computational expense has so far constrained the use of finite-element approaches in probabilistic studies, placing practical limits on the scope and complexity of the structural model and the number of variables involved.

*Scope and Outline*

The studies surveyed above, as well as others, recognize that the wind performance of a structure is fundamentally a function of resistance and load, with epistemic and stochastic uncertainties arising from numerous factors on both sides of the equation. This dissertation proposes and demonstrates a framework for systematic examination of the uncertainties bound up in these factors, advancing the classic approach of earlier probabilistic studies along two lines:

(*a*) Structural resistance is evaluated solely in terms of observable building characteristics, primarily by means of empirical design equations. Further, the system-level resistance model is generalized to take account of all reasonable failure modes in each connection in the load path. (Failure within structural members is not considered.)

(*b*) Wind pressure models are developed from ASCE 7 provisions, except that external pressure coefficients are instead evaluated directly from wind tunnel data by means of regression neural networks. By this approach, external pressure becomes a continuous function of building geometry and wind direction.

At this stage, the framework considers only wind uplift, regarding uplift performance as the bellwether of overall wind vulnerability. Throughout this work, *resistance* refers

to uplift resistance in the vertical load path, and *load* refers to wind uplift forces acting on the roof. The developed resistance and load models provide rational bases for comparing ($a$) system-level resistance across various wood-frame load paths and ($b$) wind uplift intensities across various low-rise building geometries, all in terms of fundamental structural and aerodynamic factors.

This dissertation presents the structural resistance model in Chapter 2 and the wind uplift intensity model in Chapter 3. A method for indexing low-rise buildings according to their relative aerodynamic vulnerability is proposed in Chapter 3 as well. Chapter 4 then applies a variance-based sensitivity analysis method to the structural and aerodynamic vulnerability models. The analysis separately examines the sensitivity of uplift resistance to various structural factors and the sensitivity of uplift intensity to various aerodynamic factors, and subsequently combines the resistance and load models to examine the uncertainty that both structural and aerodynamic factors contribute to wind performance. The dissertation closes with a concluding summary and recommendations for future work in Chapter 5.

# Chapter 2

## Evaluating Wind Resistance in Wood-Frame Structural Load Paths

The vulnerability of a structural system to wind damage is a function of its wind resistance and the intensity of the wind load applied to it. [1] System resistance is determined by the resistances of the various components that make up the structural load path, and component resistances are themselves determined by an array of parameters that describe the assemblage and properties of structural members and the connections between them. Uncertainty in these parameters, both epistemic and aleatory, propagates to system-level structural resistance. This chapter examines the structural resistance of light wood-frame buildings along these lines, developing a method for evaluating resistance that takes a comprehensive and granular view of the underlying uncertainties beyond what prior wind performance studies have considered. The conventional approach — represented in the work of Amini and van de Lindt (2014), Standohar-Alfano and van de Lindt (2016), and Masoomi *et al.* (2018), among others — has been to derive resistance models from representative experimental test results, like the roof-to-wall connection capacities of Reed *et al.* (1997). This approach serves well if, for example, the analysis does not intend to consider different connection configurations other than what was tested. Moreover, system-level analyses like those cited above typically model structure performance in terms of two or three connections. Because the present study is interested in a more exhaustive picture of uncertainty in structural resistance, the proposed modeling approach departs from the conventional strategy by ($a$) formulating resistance in terms of observable structural parameters like

[1] This chapter is a revised edition of Rittelmeyer and Roueche (2024).

wood species and fastener diameter and ($b$) taking account of uncertainty associated with each connection in the load path.

This chapter first describes the analysis method and its implementation in Section 2.1, with special attention to connection uplift capacity models. Several capacity models are evaluated against the results of experimental studies in Section 2.2 as a validation of the capacity modeling approach. The weight of the experimental data is from uplift tests of roof sheathing and roof-to-wall connections. Section 2.3 then applies the method to two load path archetypes to explore how parameter variations affect system-level resistance. The chapter closes with comments on the practical applications of the method and areas for further development.

## 2.1. Analysis Method

The proposed method evaluates wind resistance with respect to uplift pressures. In general, an accurate estimate of resistance in absolute terms requires consideration of combined lateral and uplift loads. But for purposes of comparison across different load path cases, both in terms of median resistance and uncertainty in resistance, it is reasoned here that uplift alone provides an adequate basis for relative evaluation. Uplift pressures are transferred from the roof to the foundation through the structural members and connections that constitute the vertical load path. The diagrams in Figure 2.1 illustrate two vertical load paths that are representative of residential construction in North America. Structural failure occurs when the demand placed on any load path element exceeds its capacity. As the post-event damage observations in Figure 2.2 indicate, it is usually connections that fail rather than members, since connections tend to be the weakest points in the load path. This is especially true of connections like roof-to-wall toe-nails, pictured at upper left in Figure 2.2, whose inherent weakness occasioned the development of the hurricane tie. It is also often true

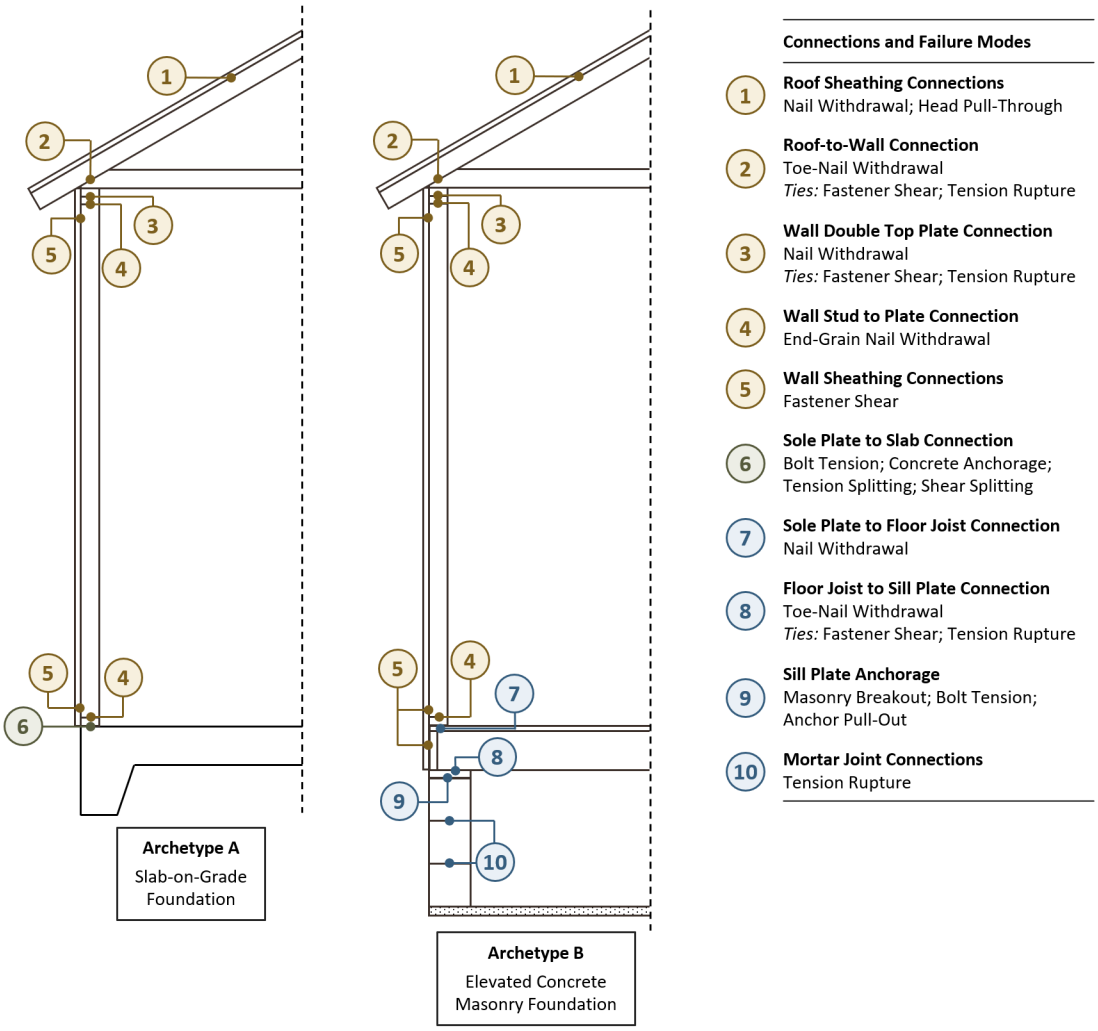


**Figure 2.1.** Structural load path archetypes considered in this study. Connections that resist uplift loads are labeled. The legend lists associated failure modes.

in cases of poor construction quality. The foundation wall pictured at lower right in Figure 2.2, in which the anchor bolt is embedded in a head joint instead of a grouted cell, is one example. This section catalogues the uplift capacity models adopted in this analysis for the connections noted in Figure 2.1 and describes the steps involved in evaluating system resistance.


**Figure 2.2.** Various load path failures observed during field surveys.

### 2.1.1. Connection Capacities

Uplift capacity models for connections between wood structural members are based on design equations provided in the *National Design Specification for Wood Construction* (2018). Withdrawal capacity $C_w$ of smooth-shank nails, which applies to most framing connections, is computed according to:

$$C_w = 3.32 K_w G^{2.5} dl \tag{2.1}$$

for a nail of diameter $d$ embedded a length $l$ into lumber with specific gravity $G$. The empirical constant $K_w$, which equals 9.51 MPa in NDS, is drawn from numerous nail withdrawal tests and includes a factor of safety suitable for structural design. Here the result is multiplied by 3.32 to raise the design value nearer to the expected ultimate

capacity. [2] The withdrawal capacity $C_{wd}$ of deformed-shank nails is similarly:

$$C_{wd} = 3.32 K_{wd} G^2 dl \tag{2.2}$$

where $K_{wd}$ is 12.4 MPa. [3] For toe-nails, the applicable withdrawal capacity is multiplied by the 0.67 toe-nail factor required in NDS, and the embedment length $l$ assumes that the toe-nail is driven at 30° at the location that NDS stipulates. [4] In the case of end-nails, although NDS allows no design capacity in withdrawal, laboratory testing has found end-grain withdrawal capacity to be 50–75% of normal-to-grain capacity across all wood species. [5] In this analysis, end-nail withdrawal capacity is reduced by an end-grain factor, which is sampled from a truncated normal distribution centered on 0.63 and bounded between 0.50 and 0.75 with a 10% coefficient of variation.

*Roof Sheathing Capacity*

Roof sheathing connections fail either by fastener withdrawal from framing or by fastener head pull-through. Depending on nail type, withdrawal capacity is computed from Eq. (2.1) or (2.2) and compared to the head pull-through capacity $C_{pt}$ given by:

$$C_{pt} = 3.32 K_{pt} \pi d_h G_s^2 \tag{2.3}$$

for a nail with head diameter $d_h$ driven into sheathing with specific gravity $G_s$. [6] The

[2] The 3.32 value corresponds to the format conversion factor prescribed in NDS to adjust reference withdrawal design values for use in LRFD design; see Table 2.3.5 in NDS.

[3] For Eqs. (2.1) and (2.2), see Eqs. 12.2-3 and 12.2-5 in NDS.

[4] See Fig. 12A in NDS.

[5] This observation is found in the Forest Products Laboratory *Wood Handbook*, p. 8-5.

[6] For Eq. (2.3), see Eq. 12.2-6 in NDS.

empirical constant $K_{pt}$ is $4.76t_s$ N/mm for sheathing panel thicknesses $t_s \leq 2.5d_h$ or $11.9d_h$ N/mm for $t_s > 2.5d_h$. Since sheathing nails are often overdriven during construction, leaving the nail head recessed into the panel, this analysis introduces an overdriving factor modeled by a normal distribution centered on 0.90 and truncated at 0.75 and 1.00 with a 0.18 standard deviation. The overdriving factor is applied as a reduction coefficient on $t_s$ in Eq. (2.3) and is implicitly present in the withdrawal capacity calculation by increasing the effective embedment length $l$. Three additional steps are taken in order to model roof sheathing as a series element in the load path:

1. Panel failure is assumed to coincide with failure of the critical fastener — that is, the fastener with the largest tributary area. The controlling capacity of a single fastener, taken as the lesser of withdrawal and head pull-through capacity, is divided by an effective tributary area equal to $1.08A_g^2 + A_g$, where the geometric tributary $A_g$ in $\text{m}^2$ is the product of roof framing member spacing and sheathing fastener field spacing. [7]

2. Because roof sheathing panels are subject to higher spatially averaged pressures than the other load path connections, panel capacity is multiplied by a pressure demand ratio $\Delta GC_{p27}/\Delta GC_{p30}$ derived from ASCE 7-22, where:

   (*a*) $\Delta GC_{p27}$ refers to $GC_p - GC_{p_i}$ obtained following the Chapter 27 directional procedure. The controlling roof pressure coefficient $C_p < 0$ is found by interpolation in Fig. 27.3-1 for winds normal to ridge. The gust-effect factor $G$ and internal pressure coefficient $GC_{p_i}$ are 0.85 and 0.18 respectively.

   (*b*) $\Delta GC_{p30}$ refers to $GC_p - GC_{p_i}$ obtained from Chapter 30. $GC_p$ are computed

[7] This tributary area definition is from NAHB Research Center (2002), "Roof Framing Connections in Conventional Residential Construction," p. 8.

for an effective wind area of 2.23 $m^2$ (24 $ft.^2$) as a function of roof shape and slope. [8] The controlling panel is assumed in Zone 3 for hip roofs with slopes $> 7°$ and in Zone 2 otherwise. $GC_{p_i}$ is taken as 0.18.

The ratio thus approximately aligns the available uplift capacity of roof sheathing with that of the main wind force resisting system in a way that takes account of roof geometry.

3. Panel capacity is also multiplied by the along-slope distance between the roof eave and the roof ridgeline, which is the assumed depth of the tributary area of the underlying roof-to-wall connection. This operation reformulates roof sheathing capacity in terms of force per length of wall and allows direct numerical comparison to the other load path connections.

*Shear Capacity: Wall Sheathing and Hurricane Ties*

Connections involving fasteners primarily subject to shear forces are modeled using the single-shear yield limit equations provided in NDS. [9] Wall sheathing connections and hurricane ties belong to this category.

($a$) For wall sheathing, the model follows the procedure of NDS Section 12.3 to determine the lateral design capacity of an individual sheathing nail, where the dowel bearing strengths of framing and sheathing are computed as functions of specific gravity $G$. [10] At this stage the model does not consider tear-out of edge

[8] Szilagyi (2022) finds 2.23 $m^2$ an appropriate effective wind area for standard 1.22 m by 2.44 m roof sheathing panels independent of fastener spacing.

[9] For the yield limit equations, see Table 12.3.1A in NDS.

[10] The empirical dowel bearing strength relationship is found in the second note under Table 12.3.3 in NDS. Since all shear connections considered in this analysis involve fasteners less than 0.64 cm in diameter, no distinction is made with respect to wood grain direction.

nails as a distinct failure mode, though this would occur in practice if nails are installed near enough to the panel edge.

(*b*) Hurricane tie capacity is based on the same NDS procedure. The analysis assumes ties to be ASTM A653 Grade 33 steel plates with an 18 gage thickness. [11] Because tension rupture of hurricane ties is occasionally observed in field surveys, the model includes a check of ultimate tension capacity on an approximate net section of 49 $mm^2$, and the lesser of tension and group shear capacity controls.

As with fastener withdrawal and pull-through, lateral design values obtained from the yield limit equations are multiplied by 3.32 so that the model results more closely represent expected ultimate strength levels. The lateral capacity of an individual fastener is also multiplied by the number of fasteners that must fail together in order to permit separation of the connected structural members. For wall sheathing panels, which resist stud-plate separation as well as separation of the top plates if the panel is fastened to the upper top plate, the analysis considers uplift capacity to be limited by the edge nails. The model divides the shear capacity of one sheathing nail by the edge nail spacing to determine the wall sheathing capacity as a force per length. For hurricane ties, the limiting number of fasteners may be either four or five depending on the installation and which underlying connection is in view. A typical roof-to-wall connection employing an H2.5A or H8 hurricane tie would require that no less than five fasteners fail in shear, but an H8 tie that is used to reinforce the face-nail connection between the top plates is likely to be secured to the lower top plate by only four fasteners.

[11] Representative of Simpson Strong-Tie H2.5A and H8 hurricane ties.

*Masonry Connection Capacities*

The capacity model for anchor bolts embedded in masonry is taken from the strength design provisions of TMS 402-13, *Building Code Requirements for Masonry Structures* (2013). For an anchor bolt with diameter $d$, ultimate tensile strength $f_{bt}$, and hook length $l_h$ embedded a length $l$ into concrete masonry with compressive strength $f'_c$, anchor capacity $C_a$ is the minimum of anchor tension rupture, masonry tension breakout, and anchor pullout according to:

$$C_a = \min \begin{cases} (\pi/4)d^2 f_{bt} \\ 4A_{pt}\sqrt{f'_c} \\ 1.5f'_c d l_h + 300\pi(l + l_h + d)d \end{cases} \tag{2.4}$$

where $f'_c$ is in psi and bolt measurements are in inches. The projected tension breakout area $A_{pt}$ is nominally $\pi l^2$, but any portion of the projected area that falls outside the masonry unit is excluded. The tension capacity of mortar joints between the courses of masonry stem walls is evaluated as $A_n f_r$, where $A_n$ is the net joint area and rupture strength $f_r$ is a function of mortar type and joint area.

*Concrete Slab Connection Capacity*

Following ACI 318-14, *Building Code Requirements for Structural Concrete* (2014), the strength of anchor bolts embedded in concrete slabs is the lesser of concrete anchorage capacity and anchor tension capacity. These limit states, which are described by the first and second entries in Eq. (2.4), ordinarily do not control wall-to-slab connection failure — typically the sole plate splits around the installed anchor bolts in shear or tension. Sole plate capacity $C_s$ is computed from:

$$C_s = \min \begin{cases} 2.88 A_v f_v \\ \\ 2.70 \dfrac{4 I_p f_t}{d_p (b_p - d_w)} \end{cases} \tag{2.5}$$

The first entry is an approximate shear capacity as a function of wood shear strength $f_v$ parallel-to-grain and shear area $A_v$, which is assumed in this study to be the product of the anchor bolt spacing and depth of the sole plate. The second entry is an approximate tension capacity for weak-axis flexure as a function of sole plate breadth $b_p$ and depth $d_p$, anchor washer diameter $d_w$, and wood shear strength $f_t$ perpendicular-to-grain. [12] The area moment of inertia $I_p$ is computed about the longitudinal axis of the sole plate over an effective length which is here assumed to be one-third the anchor bolt spacing. The adjustment factors applied to the shear and tension capacities serve the same purpose as the 3.32 factor in the capacity models described above, bringing the design values nearer to ultimate capacity. [13]

### 2.1.2. Evaluating System Resistance

The analysis procedure begins by defining the structural members and connections that make up the load path under study and compiling a parameter set encompassing every variable that contributes to connection capacity or structural dead load. The assigned probability distributions reflect the nature of the parameters and the uncertainties presupposed in the analysis case. As an example, roof-to-wall connection resistance is

[12] NDS does not provide design values for tension perpendicular to grain since wood is known to be weak under this load condition, but Section C3.8.2 of the NDS commentary notes that the design value may be considered about one-third the value for shear parallel to grain for the same species, based on tests of clear specimens. For this reason $f_t$ is estimated as $f_v/3$ in Eq. (2.5), though much lower values of $f_t$ are possible due to lumber defects.

[13] The adjustment factors are from Table 2.3.5 in NDS. The 2.70 factor applies to tension parallel to grain; its use here for tension perpendicular to grain is an approximation.

evaluated as a function of the following twelve parameters:

($a$) Roof slope, the size and spacing of roof framing members, and the number and size of toe-nails are sampled from multinomial distributions, in which outcomes may be weighted or unweighted. The type of hurricane tie installed, if any, is also discretely sampled.

($b$) Dowel bearing strength and tensile strength of the hurricane tie are sampled from normal distributions.

($c$) Specific gravities of roof and wall framing are separately sampled from mixtures of normal distributions corresponding to several wood species options. The weight of roof components is similarly sampled from a mixture distribution of roof cover weight, sheathing density, and sheathing thickness.

($d$) Roof member span is sampled from a continuous uniform distribution.

Similar parameter lists apply to the other load path connections. The analysis adopts distribution statistics that broadly reflect the range of conventional practices in North American residential construction. The number, size, and spacing of fasteners largely follow the requirements of the *International Building Code* for instance. [14] But distributions also take account of above-code features like hurricane ties that are typically found in high-wind environments, as well as below-code conditions representative of older buildings or poor construction quality. Reference values supplied in NDS for specific gravities, shear strength, and dowel bearing strength are taken as the mean of the corresponding distributions. [15]

[14] Fastener requirements are found in Table 2304.10.1 in IBC 2018.

[15] Specific gravities $G$ are from NDS Table 12.3.3A for wood framing and Table 12.3.3B for sheathing

The uplift resistance of each connection is the sum of its capacity and the cumulative dead load of the structure supported at that point in the load path, where the capacity and dead load terms are first reformulated in terms of force per length of wall. Taking the roof-to-wall connection as an example again, this operation involves the following steps:

1. The distributed weight of roof components is multiplied by the along-slope distance between the eave and ridgeline. The roof structure weight is the roof framing density multiplied by the volume of each repetitive framing member within half the roof span, divided by the roof member spacing. The sum of these is the roof-to-wall dead load.

2. The roof-to-wall capacity is the sum of toe-nail and hurricane tie capacities, divided by the roof member spacing.

In general, the capacity of a single fastener is multiplied by the number of fasteners installed per unit length of wall to obtain the equivalent linear capacity. [16] Further, wherever two or more connectors are installed in parallel, meaning that they cannot displace independently, the capacities of the constituent connectors are added together to obtain the composite capacity for the group. [17] Combining parallel connectors reduces the load path to a series system, where system resistance is defined by the minimum series connection resistance. The analysis results are obtained by evaluating

panels. Mean shear strength $f_v$ is from the NDS Supplement. Mean dowel bearing strength for hurricane ties is taken from the second footnote to NDS Table 12P.

[16] The one exception is roof sheathing, which is handled as described in Section 2.1.1.

[17] This operation assumes that the constituent connectors reach their ultimate loads at the same displacement, which is not generally true of all possible parallel connections. For toe-nails reinforced by a hurricane tie, however, Edmonson *et al.* (2012) have found the constituent uplift capacities to be statistically additive.

system resistance for $n$ random sample combinations of the underlying parameters within a Monte Carlo simulation framework.

## 2.2. Comparison to Experimental Capacities

Before examining system-level analysis results, a comparison to experimental uplift data will help establish the credibility of the capacity modeling approach described in Section 2.1.1. The high volume of test data available for roof sheathing and roof-to-wall connections, including toe-nailed and hurricane tie connections, supports a robust validation of these capacity models. Though uplift test data are more scant for other load path connections, available test results allow for a limited validation of several wall-to-slab connection capacity models.

### 2.2.1. Roof Sheathing

The test parameters of several roof sheathing uplift studies are summarized in Table 2.1, which encompass various combinations of nail type and size, nail field spacing, wood species, and sheathing type and thickness. [18] $\bar{R}_{exp}$ denotes the mean uplift resistance found in each test series. Fastener capacity is computed from Eqs. (2.1)–(2.3) for the reported parameter values, where embedment length $l$ is nail length $l_0$ less sheathing thickness $t_s$. The capacity calculation includes a deterministic overdriving factor of 0.90. The effective tributary area is based on the reported nail field spacing $s$ and the framing member spacing, which is 0.61 m in all tests. The sheathing weight is added to the capacity to obtain the predicted uplift resistance $R$.

The ratio $R/\bar{R}_{exp}$ in Table 2.1 expresses the level of agreement between the model

[18] Table 2.1 is based on a summary compiled by Datin *et al.* (2011). Tests conducted by Datin *et al.* have been added here.

**Table 2.1.** Comparison to Roof Sheathing Uplift Tests

| Reference | Nail Type | $d$ | $d_h$ | $l_0$ | $s$ | $G$ | $G_s$ | $t_s$ | Tests | $R/\bar{R}_{exp}$ |
|---|---|---|---|---|---|---|---|---|---|---|
| | | *mm* | *mm* | *mm* | *cm* | | | *mm* | | |
| Cunningham | Common | 2.87 | 6.76 | 50.8 | 30 | 0.50 | 0.42 | 11.9 | 1 | 1.08 |
| (1993) | | 3.32 | 7.14 | 63.5 | 30 | | 0.42 | 11.9 | 1 | 0.48 |
| | | 2.87 | 6.76 | 50.8 | 30 | | 0.50 | 11.1 | 1 | 0.94 |
| | | 3.32 | 7.14 | 63.5 | 30 | | 0.42 | 15.9 | 1 | 0.80 |
| | | 2.87 | 6.76 | 50.8 | 15 | | 0.42 | 11.9 | 1 | 1.08 |
| | | 3.32 | 7.14 | 63.5 | 15 | | 0.42 | 15.9 | 1 | 0.84 |
| | Annular | 3.32 | 7.14 | 63.5 | 15 | | 0.42 | 15.9 | 1 | 0.46 |
| Mizzell | Common | 2.87 | 6.76 | 50.8 | 30 | 0.42 | 0.42 | 11.9 | 4 | 1.56 |
| (1994) | | 3.32 | 7.14 | 63.5 | 30 | | 0.42 | 11.9 | 10 | 0.97 |
| | | 3.32 | 7.14 | 63.5 | 15 | | 0.42 | 11.9 | 10 | 1.21 |
| | | 3.32 | 7.14 | 63.5 | 15 | | 0.42 | 15.1 | 10 | 1.07 |
| | | 3.32 | 7.14 | 63.5 | 15 | | 0.50 | 15.1 | 10 | 1.59 |
| Jones (1998) | Common | 3.32 | 7.14 | 63.5 | 30 | 0.49 | 0.50 | 15.1 | 10 | 0.93 |
| | | 3.32 | 7.14 | 63.5 | 30 | | 0.42 | 11.9 | 9 | 0.78 |
| Sutt (2000) | Common | 3.32 | 7.14 | 63.5 | 30 | 0.55 | 0.42 | 12.7 | 7 | 0.85 |
| | | 3.32 | 7.14 | 63.5 | 30 | | 0.50 | 11.1 | 7 | 1.24 |
| Datin *et al.* | Common | 2.87 | 7.11 | 60.3 | 30 | 0.55 | 0.50 | 12.7 | 15 | 1.25 |
| (2011) | | 2.87 | 6.76 | 50.8 | 30 | | 0.50 | 12.7 | 5 | 1.22 |
| | | 2.87 | 6.76 | 50.8 | 15 | | 0.50 | 12.7 | 5 | 1.51 |
| | | 3.32 | 7.16 | 63.5 | 30 | | 0.50 | 12.7 | 15 | 0.74 |
| | | 3.32 | 7.16 | 63.5 | 20 | | 0.50 | 12.7 | 15 | 0.86 |
| | | 3.32 | 7.16 | 63.5 | 15 | | 0.50 | 12.7 | 15 | 1.01 |
| | Annular | 3.32 | 7.95 | 63.5 | 30 | | 0.50 | 12.7 | 25 | 0.62 |
| | | 3.32 | 7.95 | 63.5 | 20 | | 0.50 | 12.7 | 15 | 0.78 |
| | | 3.32 | 7.95 | 63.5 | 15 | | 0.50 | 12.7 | 13 | 0.91 |
| | | | | | | | | | *Mean* | 0.99 |

and the experimental average. Across these test series, $R/\bar{R}_{exp}$ is 0.99 on average with a 0.29 standard deviation. Differences in test procedure and aleatory uncertainty in some parameters, especially framing and sheathing density, undoubtedly drive much of the scatter in the prediction error, though some degree of systemic modeling error cannot be ruled out. Pearson correlation coefficients $\rho$, reported in Table 2.2, suggest

**Table 2.2.** Roof Sheathing: Correlation with $R/\bar{R}_{exp}$

| | Type | $d$ | $d_h$ | $l_0$ | $s$ | $G$ | $G_s$ | $t_s$ |
|---|---|---|---|---|---|---|---|---|
| $\rho$ | −0.44 | −0.52 | −0.45 | −0.48 | −0.15 | −0.30 | +0.20 | −0.17 |

a moderate inverse correlation between $R/\bar{R}_{exp}$ and nail size and type, meaning the model may tend to overpredict resistance for smaller or smooth nails and underpredict for larger or deformed nails, but the inference is not conclusive. In any case, the test results compare favorably to the model on average.

### 2.2.2. Roof-to-Wall Connections

Model results for toe-nailed connections are compared to a selection of experimental failure loads in Table 2.3. The predicted uplift capacity $C$ is the withdrawal capacity from Eq. (2.1) or (2.2) multiplied by the number of toe-nails and a deterministic adjustment factor of 0.67. [19] The mean experimental capacity $\bar{C}_{exp}$ includes no dead load. The $C/\bar{C}_{exp}$ distribution — 0.93 on average with a 0.33 standard deviation — is comparable to what was found above for roof sheathing, but the ratio is far more consistent within each study in Table 2.3 than in Table 2.1. The consistency can be seen by comparing, for example, the distribution of $C/\bar{C}_{exp}$ for the nine series in Cheng (2004) to the distribution of $R/\bar{R}_{exp}$ across the nine series in Datin *et al.* (2011). This pattern in Table 2.3 seems to indicate that factors related to experimental design largely drive variability in the prediction error for toe-nailed connections.

The same type of comparison is presented in Table 2.4 for hurricane ties. $C$ is the lateral capacity of a single nail evaluated as a function of nail diameter, framing

[19] Annular nails were used in the fourth series listed under Canfield *et al.* and in Alhawamdeh and Shao, and the first series under Morrison and Kopp used twisted nails. $C$ for these cases is computed from Eq. (2.2). The remaining studies used smooth nails.

**Table 2.3.** Comparison to Toe-Nailed Connection Uplift Tests

| Reference | Nails | $d$ | $l_0$ | $G$ | Tests | $C/\bar{C}_{exp}$ |
|---|---|---|---|---|---|---|
| | | *mm* | *mm* | | | |
| Canfield *et al.* (1991) | 3 | 3.32 | 63.5 | 0.48 | 21 | 1.38 |
| | 3 | 3.51 | 88.9 | | 10 | 1.28 |
| | 3 | 3.51 | 88.9 | | 30 | 1.03 |
| | 3 | 4.19 | 88.9 | | 20 | 1.49 |
| Reed *et al.* (1997) | 3 | 3.32 | 63.5 | 0.55 | 16 | 0.97 |
| Jones (1998) | 3 | 3.32 | 63.5 | 0.55 | 20 | 0.97 |
| | 3 | 3.32 | 63.5 | 0.42 | 20 | 0.62 |
| Riley and Sadek (2003) | 3 | 4.09 | 88.9 | 0.42 | 1 | 0.54 |
| | 3 | 4.09 | 88.9 | | 1 | 0.55 |
| Cheng (2004) | 2 | 3.43 | 88.9 | 0.42 | 10 | 0.79 |
| | 2 | 3.43 | 88.9 | 0.42 | 16 | 0.58 |
| | 2 | 3.43 | 88.9 | 0.45 | 10 | 0.75 |
| | 3 | 2.87 | 63.5 | 0.43 | 10 | 0.77 |
| | 2 | 4.09 | 88.9 | 0.45 | 12 | 0.57 |
| | 2 | 3.43 | 88.9 | 0.54 | 14 | 0.60 |
| | 2 | 3.43 | 88.9 | 0.55 | 11 | 0.64 |
| | 2 | 3.43 | 88.9 | 0.57 | 14 | 0.73 |
| | 2 | 3.43 | 88.9 | 0.56 | 14 | 0.70 |
| Shanmugam *et al.* (2009) | 2 | 4.09 | 88.9 | 0.55 | 81 | 1.40 |
| | 3 | 4.09 | 88.9 | | 19 | 1.62 |
| Morrison and Kopp (2011) | 3 | 3.43 | 82.6 | 0.50 | 63 | 1.29 |
| | 2 | 3.43 | 82.6 | | 16 | 1.26 |
| | 2 | 3.43 | 82.6 | | 16 | 1.09 |
| Edmonson *et al.* (2012) | 2 | 4.06 | 88.9 | 0.55 | 10 | 0.71 |
| Alhawamdeh and Shao (2020) | 3 | 2.87 | 60.3 | 0.50 | 5 | 0.99 |
| | | | | | *Mean* | 0.93 |

specific gravity, and hurricane tie thickness $t_p$, multiplied by the controlling number of nails. [20] Where the tested connection includes toe-nails, $C$ is the sum of hurricane

[20] Nail quantity reported in Table 2.3 is the minimum number of nails that must fail in shear to

**Table 2.4.** Comparison to Hurricane Tie Uplift Tests

| Reference | Nails | $d$ | $t_p$ | $G$ | Tests | $C/\bar{C}_{exp}$ |
|---|---|---|---|---|---|---|
| | | *mm* | *mm* | | | |
| Canfield *et al.* (1991) | 5 | 3.63 | 1.22 | 0.48 | 16 | 1.40 |
| | 4 | 3.63 | 1.24 | | 15 | 1.36 |
| | 4 | 3.07 | 0.91 | | 21 | 1.86 |
| | 4 | 3.07 | 0.94 | | 15 | 1.67 |
| | 3 | 3.12 | 1.17 | | 15 | 1.61 |
| | 4 | 3.07 | 1.27 | | 20 | 1.12 |
| | 6 | 3.63 | 1.24 | | 15 | 1.70 |
| | 5 | 3.63 | 1.22 | | 16 | 1.82 |
| | 5 | 3.12 | 1.27 | | 21 | 1.47 |
| | 4 | 3.63 | 1.17 | | 21 | 1.22 |
| | 8 | 3.63 | 1.52 | | 15 | 0.88 |
| | 4 | 3.63 | 1.52 | | 17 | 0.51 |
| Reed *et al.* (1997) | 5 | 3.32 | 1.22 | 0.55 | 19 | 1.29 |
| | 5 | 3.32 | | | 16 | 1.11 |
| Edmonson *et al.* (2012) | 9 | 3.32 | 1.22 | 0.55 | 10 | 1.12 |
| | 9 | 3.32 | | | 13 | 1.39 |
| | 9 | 3.32 | | | 7 | 1.25 |
| Alhawamdeh and Shao (2020) | 5 | 3.32 | 1.22 | 0.50 | 5 | 2.28 |
| | | | | | *Mean* | 1.39 |

tie capacity and toe-nail withdrawal capacity. [21] As a whole, the $C/\bar{C}_{exp}$ distribution suggests that the model consistently overpredicts hurricane tie capacity. The results of Reed *et al.* (1997), however, point to the considerable influence test configuration may be exerting in this comparison. Between the two series reported for Reed *et al.* in Table 2.4, the only difference is that the hurricane tie is installed on the inside of the wall in the first series and on the outside in the second series. The four studies cited

allow separation of framing members.

[21] Toe-nails are present in both series listed under Reed *et al.* and in Alhawamdeh and Shao, as well as the third series under Edmonson *et al.*

here employed substantially different experimental setups. Aside from uncertainty associated with test configuration, one possible source of systemic error in the model is the neglect of tearing failure. Both Reed *et al.* and Canfield *et al.* (1991) observed ties tearing in some tests. But even in this event, a bias toward overpredicting hurricane tie capacity is not of much consequence in a system-level analysis, since a connection reinforced by a hurricane tie is still likely to be the strongest connection in the load path even if its true capacity is somewhat less than predicted.

### 2.2.3. Wall-to-Slab Connections

Beyond roof sheathing and roof-to-wall connections, which have received far more attention in experimental studies than other load path connections, the work of Standohar-Alfano *et al.* (2017) provides a basis for local validation of two wall-to-slab connection capacity models. Standohar-Alfano *et al.* conducted uplift tests of four stud wall specimens, two with reinforcing stud-plate ties and two without ties. The specimens without ties failed by withdrawal of end-nails from the studs at an average uplift load of 1.90 kN/m. In the two reinforced specimens, the sole plates split around the anchor bolts at an average load of 2.80 kN/m. The mean experimental capacity observed for the unreinforced specimens is closely matched by Eq. (2.1), which finds the withdrawal capacity to be 1.97 kN/m. [22] The mean experimental capacity of the reinforced specimens can be approximated with similar accuracy by Eq. (2.5), where the second entry corresponding to tension capacity perpendicular to grain evaluates to 2.76 kN/m. [23] Additionally, pull-out tests of concrete-embedded anchor

[22] This result is for two end-nails measuring $4.11 \times 88.9$ mm, an estimated specific gravity $G$ of 0.40, and an end-grain strength reduction factor of 0.60, normalized by the 0.41 m stud spacing.

[23] This evaluation assumes a tension strength $f_t$ of 0.32 MPa and a washer diameter $d_w$ of 38.1 mm. The sole plate depth and breadth are 38.1 and 88.9 mm, and moment of inertia $I_p$ is based on an

**Table 2.5.** Concrete Anchorage Capacities

| Reference | Capacity | Tests | $d_s$ | $f'_c$ | $C/\bar{C}_{exp}$ |
|---|---|---|---|---|---|
| | | | $m$ | $MPa$ | |
| Nilforoush *et al.* (2017) | $4\pi l^2\sqrt{f'_c}$ | 3 | 0.33 | 41.0 | 1.00 |
| | | | 0.44 | 38.9 | 0.93 |
| | | | 0.66 | 40.1 | 0.85 |
| | | | 0.44 | 81.7 | 0.94 |

bolts conducted by Nilforoush *et al.* (2017) provide benchmark wall-to-slab anchorage capacities, summarized in Table 2.5. Concrete strength $f'_c$ and slab depth $d_s$ varied across the test series. The anchorage capacity model $4\pi l^2\sqrt{f'_c}$ compares most favorably to the mean experimental result $\bar{C}_{exp}$ for a 0.33 m slab depth, with underprediction apparently correlated with increasing slab depth. [24]

### 2.3. Resistance Model Results

Having judged the capacity modeling approach to be reasonable, the load path resistance model is now applied to several analysis cases. The first case recreates the conditions of two full-scale uplift tests of a load path similar to Archetype A in Figure 2.1. The analysis then addresses Archetypes A and B in more general terms, examining the relationship between system-level resistance and certain structural factors. The section concludes by considering the same load path archetypes in the context of post-event field studies.

effective length equal to $s_b/3$ for a bolt spacing of 1.83 m. The result is normalized by $s_b$.

[24] Anchor embedment length $l$ is 22 cm in these four test series.

### 2.3.1. Comparison to Experimental System-Level Resistance

The first analysis case is tailored to the roof-and-wall specimens tested by Riley and Sadek (2003). This study tested only two specimens in uplift, but the results provide a suitable basis for informal validation of system-level model predictions. For the test specimen constructed with toe-nailed truss-to-wall connections, Riley and Sadek observed toe-nail withdrawal at a mean roof-to-wall load of 2.73 kN, or equivalently 6.71 kN/m. [25] In the other specimen, the truss-to-wall connections were composed of two toe-nails and a hurricane tie secured to each member by four fasteners. The truss-to-wall connection remained intact in this case — instead, separation of the top plates was observed at a mean roof-to-wall load of 4.14 kN or 10.19 kN/m. [26]

The model results are presented in Figure 2.3, where the first and second rows correspond to the two uplift test cases in Riley and Sadek. [27] The left-hand column depicts connection resistance distributions; the bars indicate 5th and 95th percentile resistances and markers indicate median values. The failure probabilities in the center column report how many times out of $n$ simulations each connection is the weakest in the load path. The right-hand column reports the system-level resistance distribution, defined by the resistance of the weakest series connection. Accounting for uncertainty in wood density and other factors that are not reported in Riley and Sadek, the model results for the toe-nailed case identify the roof-to-wall connection as the system failure

[25] The 2.73 kN failure load is an average of the uplift forces observed in two truss-to-wall connections at ultimate failure. These uplift capacities are included in Table 2.3, where an estimated roof structure dead load of 133 N has been subtracted from the measured forces. The equivalent force per length is the failure load divided by the 0.41 m roof truss spacing.

[26] This is based on an average of three measured values in the second test, after the specimen was initially tested and repaired.

[27] Riley and Sadek supply roof sheathing specifications, although the uplift load application system they employed precluded roof sheathing failure; roof sheathing is included in the model results here only to offer a sense of what the expected resistance to wind uplift pressures would be.

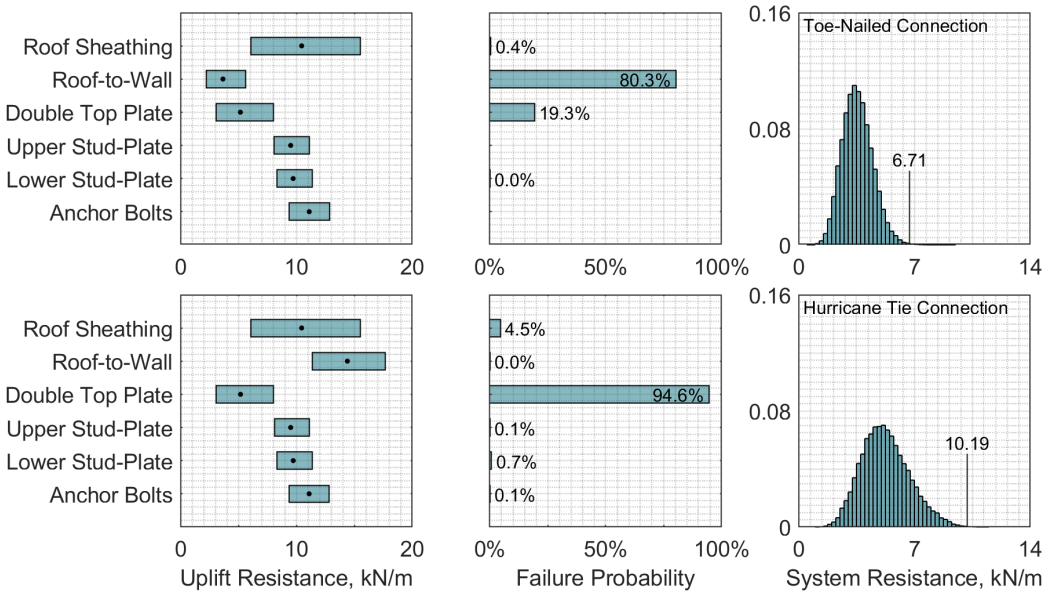


**Figure 2.3.** Resistance model results for the load path tested in uplift by Riley and Sadek (2003). Histogram annotations indicate the mean experimental uplift resistance in each test. Results are based on 50,000 simulations.

point in 80% of outcomes. For the hurricane tie case, the reinforced roof-to-wall connection becomes the statistically strongest connection in the load path, while the face-nailed top plate connection becomes statistically weakest and separates in $> 90\%$ of outcomes. [28] The median system resistance predicted by the model is 48–50% less than the mean experimental failure load for both cases. This consistency in the relative error may signal bias in one of the model parameters; it is possible, for example, that the lumber used in the test specimens was denser than the model assumes. [29] But in both cases, the model clearly agrees with the experiment as to the probable failure location.

[28] As the previous note states, since the experimental setup did not permit roof sheathing uplift failure, the model results would place the double top plate failure rate in the neighborhood of 99%.

[29] The model samples $G$ from a normal distribution centered on 0.42 with a 0.05 standard deviation, where the mean corresponds to spruce-pine-fir lumber.

### 2.3.2. Analysis of Archetype A

The structure tested by Riley and Sadek was a specific instance of the Archetype A load path defined in Figure 2.1. The results in Figure 2.4 depict variations on the same archetype but with higher degrees of epistemic uncertainty. Where the cases in Figure 2.3 reflect the uncertainty contributed by 15 structural parameters, the baseline case in the first row of Figure 2.4 preserves uncertainty in 49 parameters. Two of the most influential of these parameters are the hurricane tie installation variable and the anchor bolt washer diameter. The baseline uncertainty case assumes that the roof-to-wall connection may be composed of toe-nails only or toe-nails in conjunction with either an H2.5A or an H8 hurricane tie, with all three options equally probable. The washer diameter is uniformly sampled from five discrete values between 25 and 76 mm. The subsequent rows represent progressive strengthening of the load path by adjusting these two factors as follows:

($a$) The case in the second row limits the roof-to-wall connection to toe-nails. The absence of any hurricane tie reduces the median resistance of the roof-to-wall and double top plate connections. [30]

($b$) In the third row, the roof-to-wall connection always includes an H2.5A tie. Roof-to-wall failures are eliminated, but median system resistance rises only 15% due to conspicuous weaknesses remaining in the double top plate and wall-to-slab connections.

($c$) The roof-to-wall connection is upgraded to an H8 hurricane tie in the fourth row, precluding double top plate separation and attaining a 39% increase in median

[30] The face-nail connection between the wall top plates would otherwise be reinforced by an H8 hurricane tie.

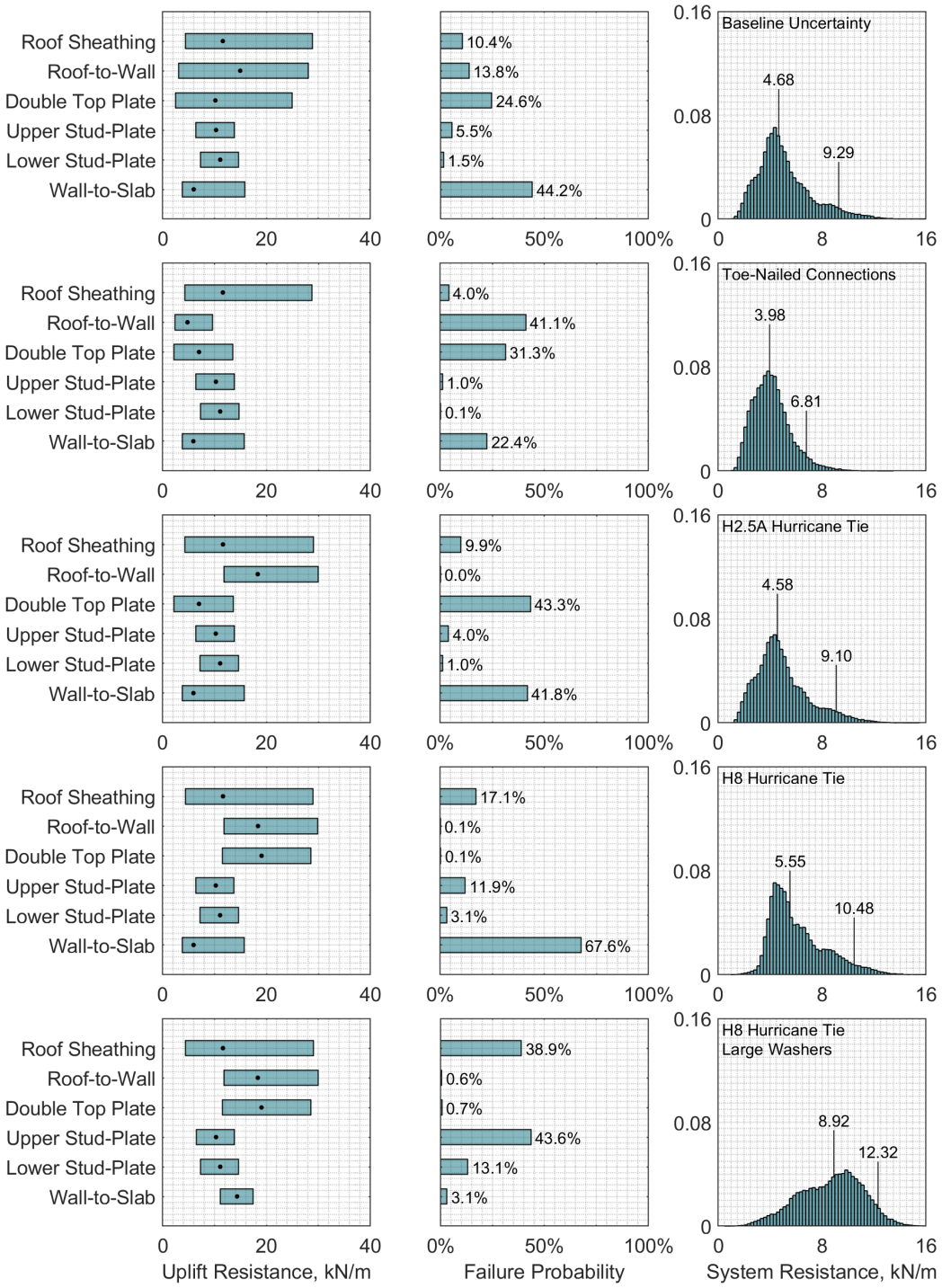


**Figure 2.4.** Uplift resistance in an Archetype A load path for various hurricane tie installations and anchor bolt washer diameters. System resistance annotations indicate the 50th and 95th percentile values. Results are based on 50,000 random samples.

system resistance over the toe-nailed case.

($d$) The fifth case relieves the weakness in the wall-to-slab connection by constraining the washer diameter to 76 mm. Combined with the advantages of the H8 tie, large washers raise median system resistance by 124% relative to the toe-nailed case. The roof sheathing and stud-to-plate connections would need to be addressed next to strengthen the load path further.

The results in Figure 2.4 also make clear that uncertainty in system resistance is not necessarily diminished by fixing a parameter at its true value, even a parameter that strongly influences resistance in one or more connections. The system resistance histograms, in which the 50th and 95th percentile resistance values are reported as a gauge of uncertainty, illustrate that knowing the hurricane tie installation state, for example, may not reduce system resistance uncertainty by itself, all else being equal. The reason is that uncertainty at the system level is driven by the level of uncertainty in the weaker connections. Constraining a parameter that applies only to a stronger connection will not have a substantial effect on load path resistance as a whole. The examples in the following sections demonstrate that system resistance inevitably becomes less uncertain once a sufficient subset of parameters is known.

### 2.3.3. Analysis of Archetype B

The load path defined as Archetype B in Figure 2.1 replaces the slab-on-grade foundation of Archetype A with a concrete masonry stem wall foundation. As in the preceding analysis, the results in Figure 2.5 represent several variations on an Archetype B load path. The baseline case in the first row is formed by retaining uncertainty in 61 structural parameters. The cases depicted in the subsequent rows cumulatively improve system resistance by selective parameter constraints.

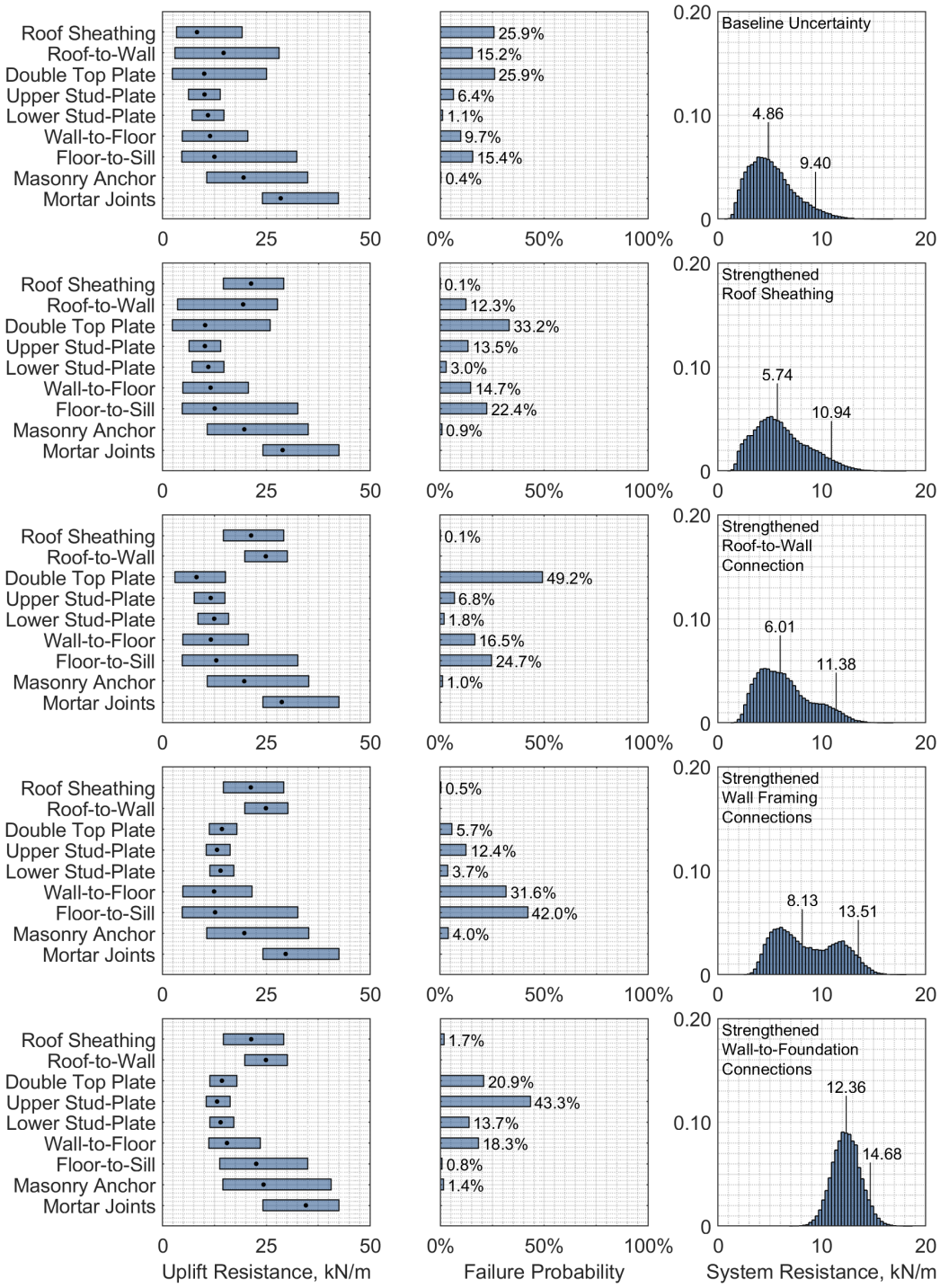


**Figure 2.5.** Uplift resistance in an Archetype B load path for various cases. System resistance annotations indicate the 50th and 95th percentile values. Results are based on 50,000 random samples.

(*a*) The second case favors roof sheathing resistance by constraining sheathing type and thickness, fastener type and size, and fastener field spacing to stronger options and limiting roof member spacing to 0.41 m. The roof framing wood species is also limited to Southern pine, the densest of the species considered in the baseline case.

(*b*) The third case retains the settings of the second case and similarly favors the roof-to-wall connection by constraining the wall framing wood species to Southern pine and requiring an H2.5A hurricane tie in all outcomes.

(*c*) Wall framing connections are addressed in the fourth case by weighting wall sheathing type and fastener edge spacing, double top plate face-nail spacing, and stud-to-plate nail size toward stronger options. Sheathing is also fastened to the upper top plate in all outcomes to reinforce the face-nail connection.

(*d*) The fifth case assumes continuous wall sheathing to the rim joist to strengthen the wall-to-floor connection. The toe-nailed connection between the floor joists and sill plate is also reinforced by an H2.5A tie in all outcomes, and the diameter and embedment length of masonry anchor bolts are improved.

System resistance variability does not substantially decline until all the characteristic weaknesses of the baseline uncertainty case have been resolved. The same would be true if the stronger outcomes within the baseline case had been eliminated instead, since the key to reducing system-level uncertainty is to minimize uncertainty in the controlling connections.

### 2.3.4. Field Study Examples

The analysis concludes here with two examples demonstrating how the load path resistance model can be leveraged as a resource for post-event field studies. The first

example is based on several residences in Lake Charles, Louisiana that were impacted by Hurricane Laura on August 27, 2020. These homes match the Archetype A load path. Field surveys found a typical rafter spacing of 0.41 m, toe-nailed roof-to-wall connections, a typical anchor bolt spacing of 1.52 m, and anchor bolt washers less than 38 mm in diameter. Southern pine was observed to be the typical wood species used in framing. Figure 2.6 reports the model results when evaluated for this set of field observations. Starting from a baseline uncertainty case like that considered in the preceding section, the field data reduce uncertainty in the system resistance distribution by 79%. [31] The second example involves a number of homes located in Cookeville, Tennessee that were surveyed after the March 3, 2020 tornado outbreak. These homes correspond to Archetype B and were found to have spruce-pine-fir wall framing, typical roof truss and floor joist spacings of 0.61 and 0.41 m respectively, fully sheathed double top plate connections, a typical anchor bolt spacing of 1.22 m, and ungrouted cells in the foundation wall. Roughly three out of four buildings had H2.5A hurricane ties installed at the roof-to-wall connection. Supplying these data to the model yields the results presented in Figure 2.7. System resistance uncertainty is reduced by 25% relative to a baseline case in which these parameters are still uncertain.

Case studies like these underscore the practical value of the proposed modeling approach in the context of field assessments. Rapidly generated data-driven resistance distributions could be useful, for example, in applying the Enhanced Fujita tornado intensity scale. [32] The EF scale method requires personnel to consider such factors as weaker-than-typical or stronger-than-typical construction practices when assigning

[31] This calculation and the next use $R_{95} - R_{50}$ as the measure of uncertainty, where $R_p$ is the $p$th percentile resistance value.

[32] For an introduction to the development of the EF scale, see Mehta (2013).

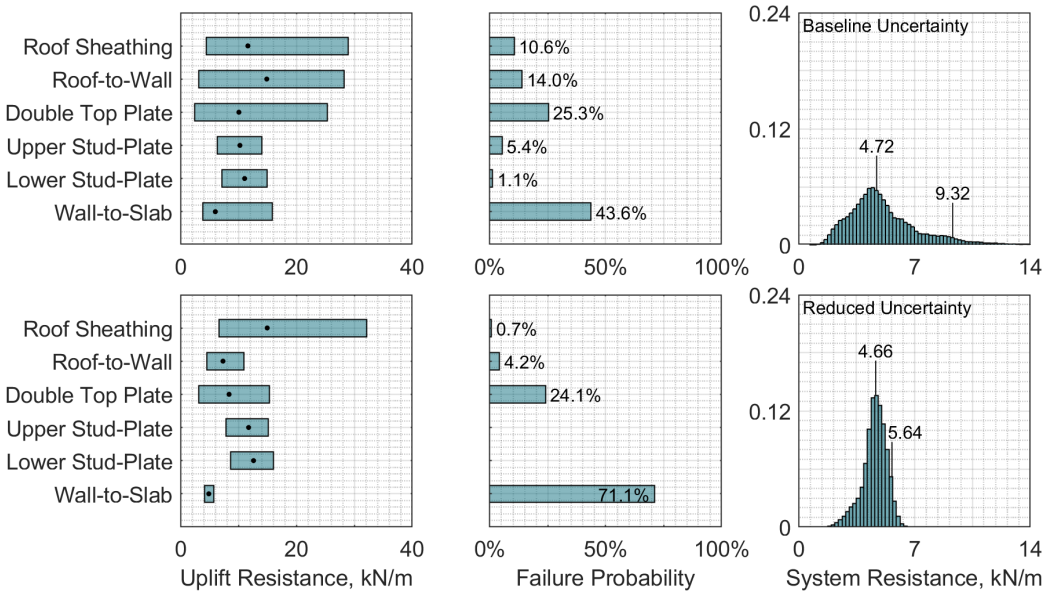


**Figure 2.6.** Uplift resistance in an Archetype A load path. The reduced uncertainty case is informed by field data collected for several homes in Lake Charles, Louisiana impacted by Hurricane Laura on August 27, 2020. System resistance annotations indicate the 50th and 95th percentile values. Results are based on 50,000 random samples.

intensity ratings from observed damage. The method presented in this chapter provides a rational basis for resolving cases of mixed evidence — for instance, a home constructed with hurricane ties at the roof-to-wall connections but small-diameter washers at the sole plate anchors. The modeling approach can also be marshaled to demonstrate the importance of load path continuity for wind damage mitigation. While elements like hurricane ties and anchor bolts have received a great deal of attention as damage mitigation measures, the model clearly illustrates that the value of improvements like these is marginal without equitable strengthening of the rest of the load path.

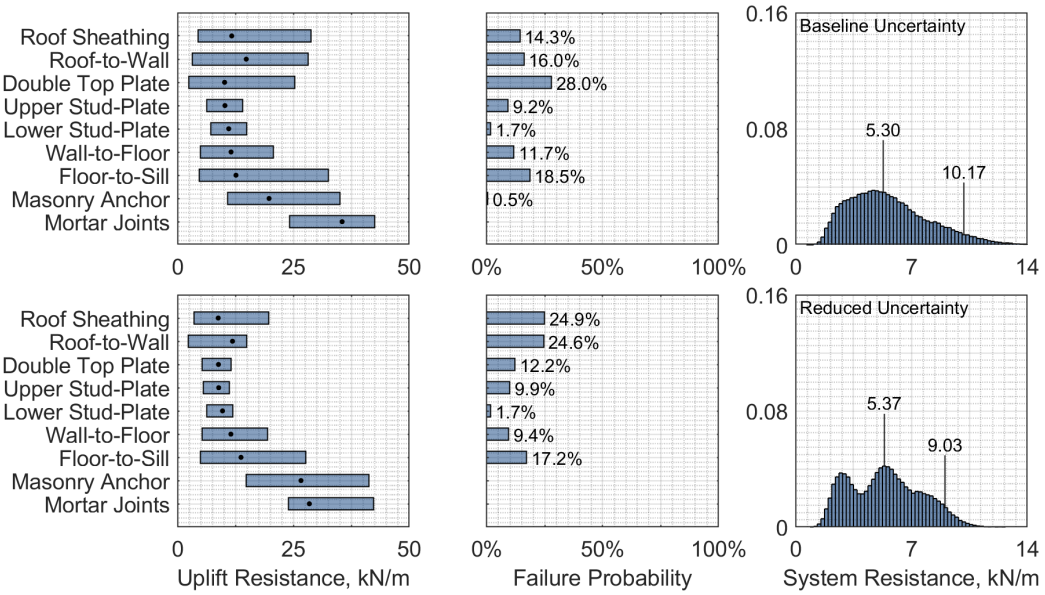


**Figure 2.7.** Uplift resistance in an Archetype B load path. The reduced uncertainty case is informed by field surveys conducted in Cookeville, Tennessee following the tornado outbreak of March 3, 2020. System resistance annotations indicate the 50th and 95th percentile values. Results are based on 50,000 random samples.

### 2.4. Summary and Applications

This chapter has presented a general method for evaluating the relative wind uplift resistance of light wood-frame load paths. The proposed approach has sought to build on earlier probabilistic studies by taking a more systematic account of load path connections and the underlying structural attributes, in order to capture the uncertainty in uplift resistance more fully. The method relies primarily on design equations for wood, concrete, and masonry connections as a time-efficient basis for modeling uplift capacities. The reasonableness of the capacity modeling approach has been verified for several connection types by comparison to experimental uplift test data, principally for roof sheathing, toe-nail, and hurricane tie connections. The method in its present form may be strengthened along several lines:

1. Since experimental uplift tests have largely focused on roof sheathing and roof-to-

wall connections, validation of the capacity models adopted for other load path connections requires additional test data. Wall sheathing edge-nail connections and wall-to-foundation connections are two areas of special interest.

2. Uplift testing of complete load paths, similar to the work of Riley and Sadek, is warranted to validate system resistance predictions and guide model refinements to account for non-linear behavior.

3. In conjunction with the preceding points, capacity models may be improved by introducing finite-element approaches or other more detailed capacity formulations. The counter-limitation here is that any new formulation would need to be time-efficient enough to be serviceable within a probabilistic framework.

4. An expansion of the method to evaluate lateral load path resistance would complement the vertical load path analysis and remove the approximation associated with defining system resistance only in terms of uplift.

Subject to further validation and refinement, the proposed analysis method lends itself to several areas of application. The central concept of the method — modeling the load path as a series system — provides a straightforward basis for assessing disparities in connection strength. The limited value of a strongly reinforced connection joined in series with one or more weaker connections can be clearly understood in these terms. The method also establishes probable failure sequences. It can be applied, for example, to prescriptive designs to ensure that roof sheathing loss is the most likely failure mode and wall-to-foundation failure the least likely, or applied to existing buildings to guide retrofit decisions. A primary purpose of the method is to serve as an uncertainty analysis tool. It provides, for instance, a rational basis for evaluating whether insurance incentives offered for certain structural improvements are commensurate with the reduced risk of damage at the system level. The method can also support post-event

damage surveys and wind speed estimation by rapidly generating a likely resistance distribution for a building and updating it as field observations are entered. [33] Lastly, sensitivity analyses based on this modeling approach can help prioritize collection of perishable field data by identifying the factors that contribute substantial uncertainty to uplift resistance. This application is considered at length in Chapter 4.

[33] Since the method takes only uplift into account at present, it may overestimate failure wind speeds in cases where significant lateral wind loads act in combination with uplift loads.

# Chapter 3

## Indexing Aerodynamic Vulnerability in Low-Rise Buildings

The preceding chapter examined wood-frame structural resistance apart from all other factors that determine wind performance. The guiding question there was: given two low-rise buildings, identical except in terms of construction quality, how much more vulnerable to wind damage is one than the other? In this chapter, our attention turns to a complementary question: if two buildings differ only in terms of geometry, how much more vulnerable is one than the other? The focus of this chapter is aerodynamic vulnerability, the level of wind vulnerability associated with such factors as roof shape, roof slope, eave height, roof overhang depth, and building plan. As the previous chapter evaluated how structural factors contribute to wind uplift resistance, this chapter considers how aerodynamic factors determine wind uplift loads.

In the case of rectangular-plan buildings with common roof shapes, no novel procedure is required to address the question of aerodynamic vulnerability. All that is needed is a means to estimate aerodynamic demand, in terms of envelope pressures, as a function of building geometry and wind direction. Numerous studies have trained machine-learning models on experimental datasets for just this purpose. Chen *et al.* (2003) developed some of the earliest of these models, training neural networks to predict mean and root-mean-squared pressures on regular gable roofs as a function of building height and incident wind angle. The training data in that study were drawn from wind tunnel experiments conducted at the University of Western Ontario, which were later supplemented by additional gable-roof test cases and published as

the first component of the NIST aerodynamic database. [1] Drawing from this expanded dataset, Gavalda *et al.* (2011) generalized the work of Chen *et al.* to include roof slope and building plan dimensions in the set of predictor variables. More recently, Ding *et al.* (2022) trained an array of neural networks on the NIST dataset with an interest in comparing various ways to optimize model hyperparameters. Following the initial release of the NIST database, Tokyo Polytechnic University published its catalog of wind tunnel measurements, encompassing various gable, hip, and flat-roof building models in isolation and in group configurations. [2] Relying on a subset of the TPU isolated buildings data, Bre *et al.* (2018) developed neural networks to predict surface-averaged mean pressures as a function of plan aspect ratio, roof slope, and wind direction. Meddage *et al.* (2022) and Weng and Paal (2022) separately applied TPU data for non-isolated buildings to train decision-tree-based prediction models that take account of spacing between neighboring buildings. Another wind tunnel dataset of gable-roof building models collected at the University of Florida [3] formed the basis of studies by Fernández-Cabán *et al.* (2018), whose roof pressure models account for the influence of free-stream turbulence intensity, and Tian *et al.* (2020), who also leveraged the NIST dataset to explore multiple neural-network approaches for roof and wall pressure prediction. The full-scale field measurements of Texas Tech University [4] and large-scale wind tunnel tests conducted at Florida International University [5] have similarly supplied data for machine-learning prediction efforts, including Weng and

[1] Ho *et al.* (2005) describe the development of the NIST database; see also St. Pierre *et al.* (2005). The aerodynamic data can be accessed at `https://www.nist.gov/el/`.

[2] The TPU datasets are available at `https://db.wind.arch.t-kougei.ac.jp/`.

[3] This dataset is available in Fernández-Cabán and Masters (2018).

[4] The TTU datasets are accessible at `https://doi.org/10.17603/DS24D68`. A guide to the datasets is found in Smith *et al.* (2017).

[5] Gan Chowdhury *et al.* (2017) describe the FIU test methodology.

Paal (2023). The presently available datasets and the associated body of prediction methodologies provide more than enough information to interpolate wind pressure distributions on practically any rectangular-plan building with a gable, hip, or flat roof. Merely evaluating and spatially averaging pressures over a range of wind directions offers an intuitive solution to the aerodynamic vulnerability problem for these cases.

For buildings that are not rectangular in plan, however, the task is not so straightforward. [6] The number of possible complex geometries is vast, and though wind tunnel studies like Shao *et al.* (2018) and Dev Sarma *et al.* (2023) have been carried out for some irregular-plan geometries, data for such buildings remain sparse. The project of compiling a thorough database of envelope pressures for complex low-rise buildings will undoubtedly require a great deal of time and expense to complete. Recognizing this challenge, as well as the reality that most of the North American light wood-frame building inventory is not rectangular in plan, the present study proposes a method to estimate the relative vulnerability of various building geometries, inclusive of irregular plans and one or both of gable and hip roof shapes. Like the pressure prediction studies surveyed above, the proposed analysis procedure employs machine learning to interpolate experimental wind pressures, but unlike any previous study, predicted pressures are processed into geometry-specific estimates of wind vulnerability. The vulnerability indexing system presented here may serve useful purposes in wind engineering research, especially in connection with post-event analysis.

[6] The terms *complex* and *irregular* are used interchangeably throughout this chapter to refer to building or roof geometries that are non-rectangular in plan.

### 3.1. Analysis Method

The following three modeling premises shape the development of the analysis procedure:

($a$) Many low-rise buildings, especially residential buildings, are made up of some combination of essentially gable-roof and hip-roof sections.

($b$) The wind vulnerability of a low-rise building is closely tied to the intensity of uplift pressures acting on the roof.

($c$) Roof uplift pressures are typically most severe on the upwind side of the building, where *upwind* refers to the portion of the building most directly exposed to incident wind. [7]

The steps in the procedure are summarized in Figure 3.1. Complex geometries are first broken down into regular gable or hip-roof sections according to premise ($a$). For all wind directions, roof pressures are predicted in the upwind section of the building following premise ($c$). The most extreme uplift pressure, averaged over an appropriate area, is recorded for each wind angle, representing the uplift intensity at that angle. Wind vulnerability is then computed from the uplift intensity data in accord with premise ($b$). The sections that follow describe how each of these tasks is carried out.

#### 3.1.1. Defining Building Geometry and Identifying Upwind Sections

The procedure begins by defining the geometry of the building under study. Programmatically this requires (1) outlining the projected roof plan, (2) designating the

[7] Figure 3.2 illustrates the definition of *upwind* as it is used throughout this chapter. This term is chosen to avoid confusion with the term *windward*, which in ASCE 7 and elsewhere refers to any roof surface that faces toward the incident wind direction. Roof sections A and C in Figure 3.2 possess windward and leeward surfaces, but the sections as a whole make up the upwind portion of the roof for the indicated wind angle.

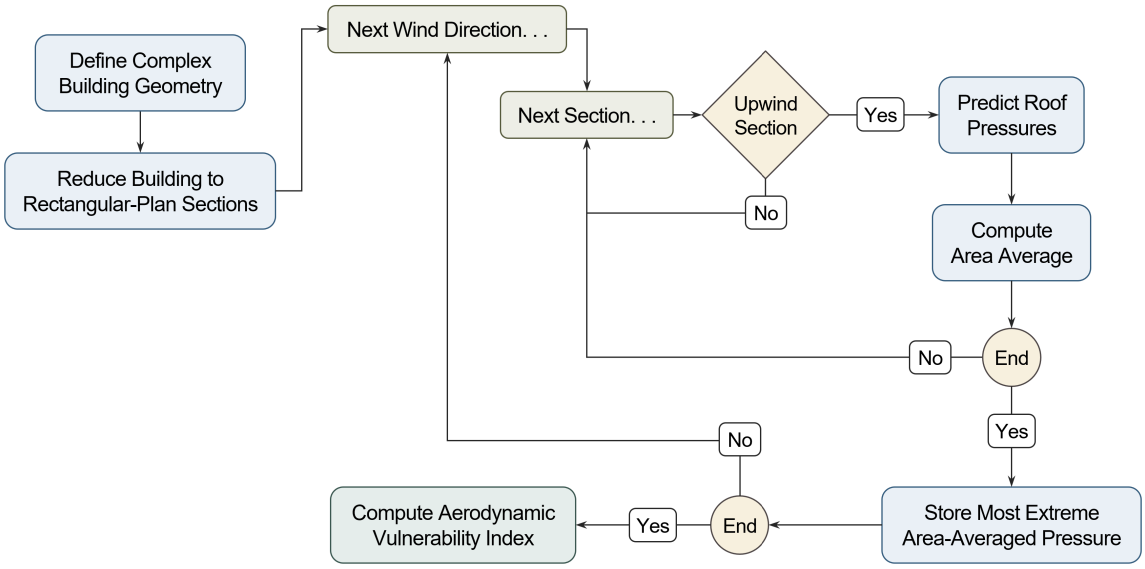


**Figure 3.1.** Steps in the aerodynamic vulnerability analysis procedure.

various roof regions as gable or hip, and (3) assigning the slope, eave height, and overhang depth in each portion of the roof. A wide array of complex geometries can be specified in this way, and from the perspective of modeling premise ($a$) stated above, any geometry so generated can be subdivided into sections defined by the presence of either a gable-end or a hip-end. As an example, the combination gable-hip building depicted in Figure 3.2 is made up of two hip-roof sections and an intersecting gable-roof section. In general, the extent of a section is bounded by symmetry lines or adjacent valleys. The basic purpose of section subdivision is to decompose irregular plans into regular-plan units on which roof pressures can be reasonably estimated from available wind tunnel data.

Subsequent tasks are carried out as a function of wind direction. The initial task is to identify the upwind section or sections for a certain wind angle $\theta$. Limiting analysis to upwind sections defined as such is based on modeling premise ($c$), that roof uplift pressures are generally most intense in the part of the building that is most directly exposed to incident wind. To the degree that the premise is true, the wealth of data

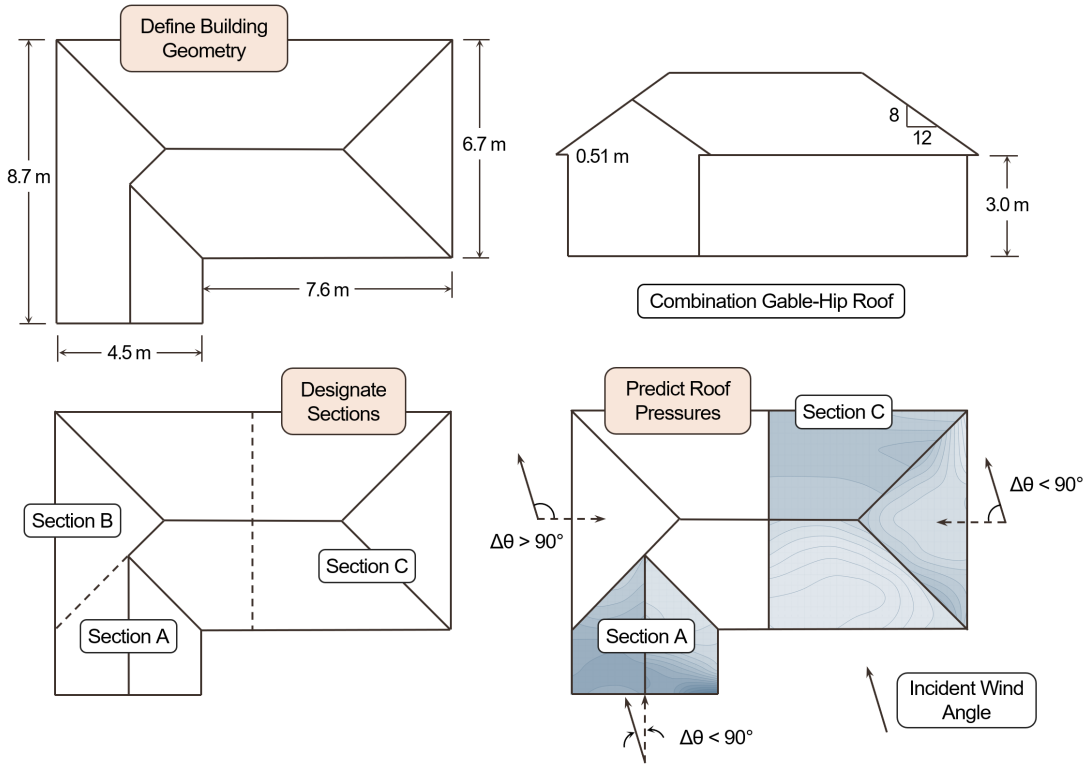


**Figure 3.2.** Example of the geometry generation, section subdivision, and upwind section recognition steps in the analysis procedure.

available for regular gable and hip roofs can be applied to complex roofs by analyzing the constituent regular-plan sections in virtual aerodynamic isolation from the rest of the building. The lower right-hand portion of Figure 3.2 illustrates the criterion for identifying upwind sections. The dashed arrows define the orientation of each roof section, where the arrow is drawn parallel to the section ridgeline and points toward the interior of the building plan. For an incident wind angle $\theta$, the relative wind angle $\Delta\theta$ is computed for each section as the difference of $\theta$ and the section orientation. Any section where $\Delta\theta \leq 90°$ is counted as upwind at that wind direction. Sections A and C would be considered upwind for the wind angle indicated in Figure 3.2.

**Table 3.1.** Aerodynamic Database Test Cases: Low-Rise Buildings, No Eaves

| Roof Type | Roof Slope | Aspect Ratio | | Wind Direction |
|---|---|---|---|---|
| | $\beta$ | $d/b$ | $h/b$ | $\theta$ |
| Flat | 0° | 1:1, 3:2, 5:2 | | |
| Gable | 4.8°, 9.4°, 14°, 18.4°, 21.8°, 26.7°, 30°, 45° | 1:1, 3:2, 5:2 | 1:4, 1:2, 3:4, 1:1, | 0°, 15°, 30°, 45°, 60°, 75°, 90° |
| Hip | 26.7°, 45° | 3:2 | | |

### 3.1.2. Wind Tunnel Databases

Pressure prediction models in this study are trained on wind tunnel data available in the Tokyo Polytechnic University aerodynamic databases, specifically the databases for isolated low-rise buildings without eaves and with varied eaves. Selection of these datasets is driven primarily by the wide range of models tested. The scope of the without-eaves buildings database, summarized in Table 3.1, encompasses numerous gable-roof building geometries as well as several representative hip-roof geometries, which is especially valuable considering the prevalence of hip roofs in high-wind regions. Test models in the varied-eaves database, summarized in Table 3.2, feature roof overhangs in multiple configurations and at several height aspect ratios. [8] Though the varied-eaves building models have only gable roofs at a 26.7° slope and only one overhang depth is tested, these data nonetheless provide a basis for estimating lower surface pressures on both gable and hip-roof overhangs of typical depth.

Test case parameters are defined in Figure 3.3. Depth $d$ and breadth $b$ are measured parallel to and normal to the roof ridgeline respectively. For hip-roof test models,

[8] This database also contains a fourth model type, designated Type O, that does not have eaves; no training data have been drawn from Type O cases in this study.

**Table 3.2.** Aerodynamic Database Test Cases: Low-Rise Buildings, Varied Eaves

| Model Type | Eave Placement and Orientation | Roof Type | Roof Slope | Aspect Ratio | | Wind Direction |
|---|---|---|---|---|---|---|
| | | | $\beta$ | $d/b$ | $h/b$ | $\theta$ |
| A | Side walls only, lower surfaces sloped. | Gable | 26.7° | 6:5 | 3:10, 3:5, 9:10 | 0°, 22.5°, 45°, 67.5°, 90° |
| B | Side walls only, lower surfaces horizontal. | | | | | |
| C | Gable-end and side walls, lower surfaces sloped. | | | 7:5 | | |

all roof surfaces have the same slope. It should be noted that geometry parameter definitions adopted in this study differ slightly from their usage in the TPU database documentation. Throughout this chapter, $h$ always designates eave height, not mean roof height, and $d$ and $b$ always refer to the projected plan dimensions of the roof rather than of the building footprint. (In other words, roof overhang depth is included in $d$ and $b$ for any case.) The aspect ratios reported in Table 3.2 are based on these definitions. Further, the $x$-$y$ coordinate system used throughout this chapter is located on the perimeter of the roof plan as in Figure 3.3, rather than at the centroid of the roof plan as in the TPU databases.

For both wind tunnel datasets, the wind field characteristics correspond to suburban terrain. At a length scale of 1:100, all test models have a building footprint breadth of 16 m in full scale, with pressure taps distributed across all roof and wall surfaces at a typical full-scale spacing of 2 m between adjacent taps and 1 m between surface boundaries and the outermost row of taps. Models in the varied-eaves database have a roof overhang depth of 2 m in full scale, and lower surfaces of overhangs are instrumented with a single row of pressure taps spaced at 2 m. The time series dataset for each test case contains the pressure history at each tap location over ten minutes in full scale. Static pressure readings are normalized by a reference wind pressure for

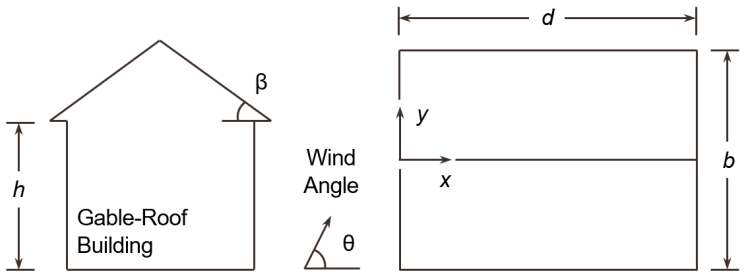


**Figure 3.3.** Building geometry definitions on a regular gable-roof building model shown in elevation and plan view.

a full-scale wind speed of 22 m/s in the without-eaves database and 23.4 m/s in the varied-eaves database, corresponding to the ten-minute average wind speed at model mean roof height. Local pressure histories are moving-averaged over a full-scale time duration of 1 s for buildings without eaves and 0.2 s for buildings with eaves. In this analysis, the mean $C_p$ of the entire ten-minute time history serves as the response variable in prediction model training. [9] Since the analysis is primarily interested in relative comparison of different geometries, the time series mean is arbitrarily chosen as the basis for comparison.

### 3.1.3. Pressure Prediction

The proposed framework makes use of trained pressure prediction models to generalize the wind tunnel test data to untested cases. In line with the consensus of previous roof pressure studies, the prediction models developed for this analysis are feed-forward regression neural networks. Nine regression models have been trained for use in this study, summarized in Table 3.3. One departure from the approach of previous studies is that dedicated models are trained for specific roof surfaces. Gable roof pressures

[9] Wherever $C_p$ appears without qualification in this chapter and the next, it refers to the *mean* of the pressure time history unless the context indicates otherwise.

**Table 3.3.** Regression Models

| Type | Surface | Model | Predictor Variables |
|---|---|---|---|
| Gable Roofs | Windward | G5 | Coordinates $x/b$ and $y/b$, aspect ratio $h/b$, roof slope $\beta$, and wind direction $\theta$. (5) |
| | Leeward | G6 | |
| Hip Roofs | End | H5 | |
| | Windward | H6 | |
| | Leeward | H8 | |
| Roof Overhangs | Leeward Side | S6 | Eave coordinate $x/b$ or $y/b$, aspect ratio $h/b$, and wind direction $\theta$. (3) |
| | Windward Side | S7 | |
| | Hip End | S71 | |
| | Gable End | S8 | |

are predicted by two models separately trained on windward and leeward roof surface data, rather than one larger model trained on data for both surfaces together; three independent models are similarly trained for the windward, leeward, and end surfaces of hip roofs. The rationale behind this approach is that the reduced training time and narrowed scope of surface-specific models allow for more tailored optimization of model hyperparameters, tending to improve prediction accuracy. Another element not considered in most past studies is the inclusion of roof overhang effects. Four regression models are respectively trained to estimate lower-surface pressures on leeward and windward side eaves parallel to ridgeline, hip-end eaves normal to ridgeline, and gable-end rakes. Model identifiers in Table 3.3 follow the numbering system used in the TPU databases and refer to the roof or eave surface from which training data for that model are primarily drawn.

The independent variables in the wind tunnel tests determine the predictor variables for each model. Gable and hip roof pressures are predicted as a function of five variables: roof coordinates $x/b$ and $y/b$, measured parallel to and normal to ridgeline respectively and normalized by roof plan breadth $b$; ratio of eave height to breadth $h/b$; roof slope $\beta$; and wind direction $\theta$. Only three predictors are applicable to roof overhangs:

coordinate $x/b$ or $y/b$ depending on the orientation of the eave, height aspect ratio $h/b$, and wind direction $\theta$. Models are trained on the whole range of applicable combinations of $h/b$, $\beta$, and $\theta$ shown in Tables 3.1 and 3.2. Models G5 and G6 are trained only for a $d/b$ ratio of 3:2. Removing this aspect ratio as a model feature and including data for only one value of $d/b$ simplifies the model structure and substantially improves training efficiency at negligible cost to prediction accuracy. [10] Discussions in past pressure prediction studies demonstrate that the translation of experimental parameters into an appropriate set of model predictors is a matter of reasoned judgment. One of several variables could be selected as the normalizing parameter for spatial quantities, for example. The breadth parameter $b$ serves that purpose here, presenting itself as a convenient option since $b$ is constant across all test models in each of the two databases and therefore cannot serve as a predictor variable itself. [11]

*Dataset Preprocessing*

Wind tunnel time series data are preprocessed into model datasets by the following steps:

1. Mean $C_p$ is computed for each pressure tap as the ten-minute average of the time history.

2. Tables of mean $C_p$ are compiled as a function of all applicable predictor variables for all test cases; test data are aggregated by roof type and segregated by surface number.

[10] Inspection of the wind tunnel data indicates that local gable-roof $C_p$ for $x/b \leq 1$ are relatively insensitive to $d/b$, especially for $\theta \leq 60°$. Further, for analysis of building sections rather than whole buildings, $d/b$ ratios beyond 3:2 often do not even come into view.

[11] Height is also sometimes used as the normalizing parameter; see Gavalda *et al.* for example.

3. Pressure tap coordinates $x$ and $y$ and eave height $h$ are normalized by the full-scale roof plan breadth $b$, 16 m for the gable and hip surface datasets and 20 m for the overhang datasets.

4. Within each surface-specific dataset, predictors are standardized by centering variable data on the mean value and normalizing by the standard deviation to remove any influence of the absolute scale of the predictors.

Model datasets for gable and hip roof surfaces are supplemented with $C_p$ for flat-roof cases at all tested combinations of $h/b$ and $\theta$, limited to a $d/b$ ratio of 3:2. Flat-roof data are apportioned to the surface-specific gable and hip datasets on the basis of coincident projected plan area; flat-roof data for $y/b < 0$ are added to the G5 dataset, data for $y/b > 0$ are added to G6, data for $x/b + y/b > 0.5$ are added to H8, and so on. Incorporating flat-roof data enforces an appropriate lower bound on predictions for gable roof slopes $< 4.8°$ and makes a profound difference to predictions for hip roof slopes $< 26.7°$. The gable and hip datasets are also truncated to limit data to $x/b \leq 1$. Since upwind building sections, not standalone buildings, are the object of analysis, predicted pressures at locations $x/b > 1$ are unlikely to be meaningful to the final result of the vulnerability evaluation.

Datasets for models S6 and S7 are respectively built from leeward and windward overhang pressure data for Type B cases in the varied-eaves database, summarized in Table 3.2, on the view that the horizontal lower surfaces of Type B eaves are more representative of typical roof overhangs than the sloped eaves of Types A and C. However, because Type B eaves do not project beyond the gable-end wall, data for the corner eave pressure taps of Type C cases are also supplied to the S6 and S7 datasets. The data are then restricted to $x/b \leq 1.05$, effectively removing data for the last three pressure taps on each side-wall eave in an effort to limit downstream end effects, which would be appropriate for whole buildings but not for upwind sections

of buildings. The model dataset for S71 is similarly made up of Type B windward overhang data supplemented with Type C windward corner eave data, but wind directions are reversed and pressure tap coordinates are transposed and renormalized by roof depth $d$, so that tap locations are defined on $-0.5 < y/b < 0.5$. For a $d$ and $b$ of 28 m and 20 m in full scale, this transformation effectively rescales the windward side-wall overhang $C_p$ distribution by a factor of 5:7, and as such, model S71 predictions are an approximate extrapolation of the wind tunnel data. Type C gable-end rake data furnish the S8 model dataset on the same $y/b$ domain as in model S71.

The preprocessed, unpartitioned datasets contain 8,064 observations each for models G5 and G6, 1,568 observations for model H5, and 1,960 observations each for models H6 and H8. The relative sizes of these datasets are primarily a consequence of the eight roof slopes considered in the gable-roof test series, compared to only two for hip roofs. The data for roof overhangs are still more scant since the number of varied-eaves test cases is far fewer, and the overhang surfaces have fewer pressure taps, than is true of roof surfaces in the without-eaves database. After taking the preprocessing steps described above, the roof overhang datasets contain 165 observations each for models S6 and S7, 210 observations for model S71, and 150 observations for model S8. Because of the training challenges presented by such a low volume of data, synthetic observations are generated for these four datasets by smooth interpolation in $x/b$ or $y/b$ as applicable. This approach is justified by recognizing that the analysis framework as a whole requires nothing more of the overhang regression models than a reasonable one-dimensional interpolation of $C_p$ between adjacent pressure tap locations. Spatial interpolation in this case amounts to giving the model *a priori* instructions regarding how to generalize to untested coordinates while relying on the training process to discern an effective generalization strategy for untested $h/b$ and $\theta$. In these datasets,

nine evenly spaced synthetic observations are sampled by Akima interpolation between each pair of adjacent tap locations, excluding the corner taps in models S6, S7, and S71. The refined datasets contain 1,380 observations each for models S6 and S7, 1,695 observations for model S71, and 1,365 observations for model S8.

*Regression Model Development*

Following the standard practice of earlier studies, each regression model is designed as a bilayered neural network, composed of two fully connected hidden layers of neurons between the input and output layers. A more thorough treatment of neural network theory is available in other works, Mehlig (2021) for example. As a brief sketch, the input layer contains neurons that represent the model predictor variables. The input value of each predictor is conveyed to all neurons in the first hidden layer, which apply multiplicative weights and additive bias terms to the input values. Outputs from the first hidden layer are forwarded through a transfer or activation function and received as input to the second hidden layer, which applies a second set of weights and biases followed by another activation function. Outputs from the second layer are then processed through a final set of weights and biases and a linear activation function to arrive at the output layer value, which is the predicted response. Models are trained by generating predictions for a set of training observations and iteratively adjusting the weights and biases on the basis of error, expressed by a loss function, between the predicted response and the true or observed response.

The preceding description applies in general to any neural network of bilayered architecture, but networks vary widely in terms of model hyperparameters, which constrain the weights and biases and control how they are updated during training. Among these is layer width, or the number of neurons in each hidden layer, which strongly influences predictive capacity. Layer widths determine the size of the weight

**Table 3.4.** Regression Model Training Summary

| Model | Architecture | $\lambda$ | Observations | | | Iterations | MSE | $R^2$ |
|---|---|---|---|---|---|---|---|---|
| | | $1/10^{-4}$ | *Train* | *Validate* | *Test* | | $1/10^{-3}$ | |
| G5 | 5-28-28-1 | 1.669 | 6,451 | 807 | 806 | 456 | 3.887 | 0.982 |
| G6 | 5-27-28-1 | 0.467 | 6,451 | 807 | 806 | 408 | 2.424 | 0.971 |
| H5 | 5-25-19-1 | 1.886 | 1,254 | 157 | 157 | 396 | 4.270 | 0.978 |
| H6 | 5-28-18-1 | 0.767 | 1,568 | 196 | 196 | 176 | 3.689 | 0.984 |
| H8 | 5-22-12-1 | 1.190 | 1,568 | 196 | 196 | 198 | 1.664 | 0.967 |
| S6 | 3-11-25-1 | 1.313 | 1,104 | 138 | 138 | 115 | 0.248 | 0.984 |
| S7 | 3-16-12-1 | 2.284 | 1,104 | 138 | 138 | 126 | 0.582 | 0.998 |
| S71 | 3-28-22-1 | 3.002 | 1,356 | 170 | 169 | 202 | 0.504 | 0.998 |
| S8 | 3-12-28-1 | 2.448 | 1,092 | 137 | 136 | 257 | 0.623 | 0.998 |

and bias arrays in the model. Increasing layer width raises the number of adjustable parameters, enabling the model to capture more complex relationships in the source data, but overly wide layers can produce a model that so closely adheres to the training data that it does not generalize well to new cases. Layer widths that strike a proper balance are dependent on the data. The architectures assigned to the models in this study are listed in Table 3.4, where the first digit is the number of predictor variables, the last digit is the number of output variables (1), and the intermediate numbers are the widths of the first and second hidden layers.

Besides limiting layer width, another measure often used as a safeguard against model overfitting is regularization, which places an indirect constraint on the values assigned to model weights. A common regularization approach is to add a weight-dependent penalty term to the error computed by the loss function, so that the training algorithm attempts to minimize the prediction error together with the weight penalty. In this study, a regularization term $0.5\lambda w^{\mathrm{T}}w$ is added to the loss term, where $\lambda$ is the regularization rate and $w$ is a vector containing the model weights. This is a form of $L_2$ regularization in which the penalty is a function of the sum of squares of the weights, and the regularization rate $\lambda$ is a key model hyperparameter that determines

how much influence the penalty term exerts on the training algorithm relative to training loss. The summary in Table 3.4 notes the regularization rate used to train each model in the analysis.

Other hyperparameters do not vary across the models developed here. Most notably:

1. The rectified linear unit function serves as the activation function after both hidden layers in all models. Since the weighting operations are strictly linear, activation functions facilitate nonlinear learning in the training process and are commonly selected as some combination of $(a)$ the standard logistic, or sigmoid, function, $(b)$ the hyperbolic tangent function, and $(c)$ the rectified linear unit function, which leaves positive values unchanged and maps all negative values to zero.

2. Initial values of weights are assigned by Glorot initialization, whereby the weights in a certain layer are sampled from a uniform distribution centered on zero with a variance of $2/(n_i + n_{i+1})$, where the terms in the denominator denote the number of neurons in that layer and the successive layer respectively. [12] Biases are assigned an initial value of zero.

3. Model training is carried out using a limited-memory Broyden-Fletcher-Goldfarb-Shanno algorithm, which performs iterative gradient descent to minimize loss. [13] The algorithm uses a line-search method to estimate an appropriate learning rate at each training iteration and thus does not require that a learning rate

[12] The mathematical basis for this method is found in Glorot and Bengio (2010).

[13] The limited-memory BFGS method is described in Nocedal (1980); see also Liu and Nocedal (1989).

be specified in advance. As a full-batch method, predictions are generated for the entire training set in each iteration. The loss function computes the mean squared error between the predicted and observed $C_p$ in the training set.

The data splitting strategy is also the same across all models. The preprocessed dataset for each model is partitioned at random into a training set containing 80% of the observations, with the other 20% evenly divided between a validation set and a test set. Since the original datasets contain no duplicate entries, the partitioned subsets have no observations in common. Random partitioning preserves a roughly equal distribution of each predictor variable across subsets; a wind direction of 60°, for example, appears in about one out of seven entries in the training, validation, and test sets for model G5, and so for all predictors. This approach supports a robust test of the generalization power of the model by removing suspicion of selection bias.

The partitioned datasets serve complementary purposes in model development. Models are trained by minimizing loss on the training set. At each training iteration, model loss is also computed on the validation set; since the observations in the validation set are new to the model, validation loss gauges how well the model generalizes to untried cases as training progresses. After so many iterations, validation loss no longer improves, signaling that further training will not strengthen prediction accuracy on new cases. For this study, model training is suspended once validation loss reaches a minimum and does not improve on that minimum for twenty iterations afterward. The trained model is then evaluated on the test set as a final check of the model's capacity to generalize to new data, since the test set has no direct or indirect influence on model training. The quality of different model configurations is then judged on the basis of the mean squared error and coefficient of determination $R^2$ computed on the test set, which are scale-sensitive and scale-insensitive measures of prediction accuracy. Partitioned dataset sizes, number of training iterations, and test

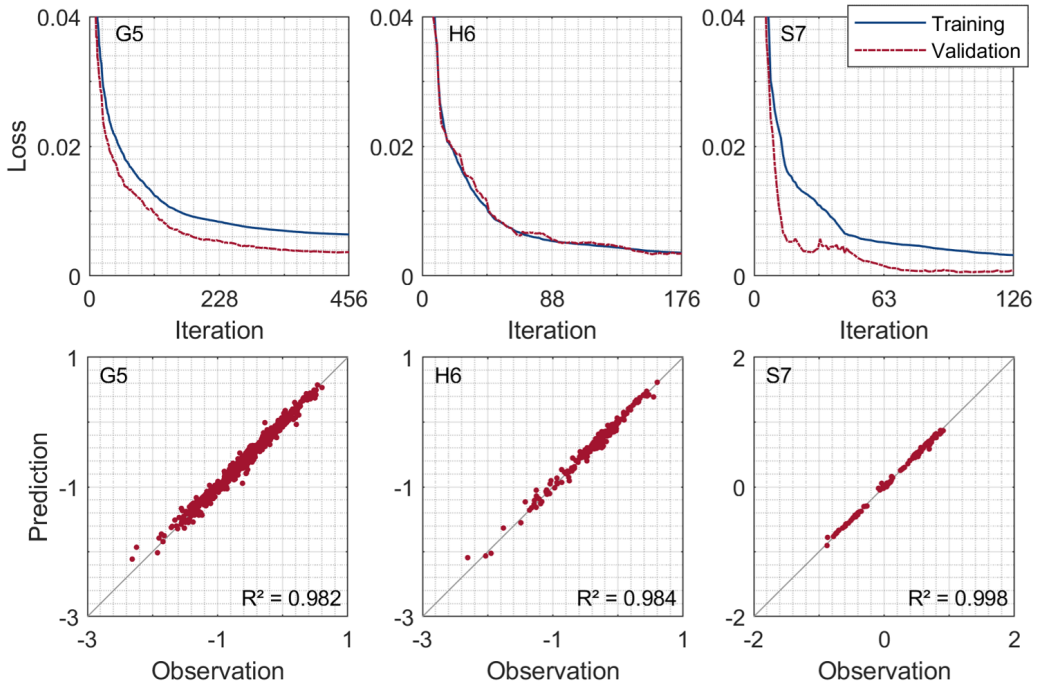


**Figure 3.4.** Generalization curves and prediction accuracy on the test set for the G5, H6, and S7 regression models. Validation loss curves plot only mean squared error while training loss curves add the regularization term to the error; when adjusted for regularization, training loss is less than validation loss.

set accuracy metrics are summarized for all models in Table 3.4. Loss curves and test set accuracy plots for models G5, H6, and S7 are shown in Figure 3.4.

Because optimal model configurations are determined by the nature of the data, satisfactory models can only be found by a trial-and-error procedure of repeated training and testing, whether by hand or by an iterative automated approach. One challenge to hyperparameter optimization is that the training process itself is not deterministic. Random dataset partitioning and random initialization of model weights can lead to wide variation in outcomes across otherwise identical training routines. In general, a satisfactory hyperparameter configuration must produce models that achieve a sufficient level of test accuracy at an acceptable rate over a number of random trials. Minimum accuracy and robustness thresholds are arbitrary and depend on how strongly one expects the model predictions to influence the output of the

broader analysis. Models in this study are optimized by the following steps:

1. The regularization rate $\lambda$ and the widths of the first and second hidden layers are selected as the optimizing variables on the assumption that these alone exercise such influence on model performance that other hyperparameters do not need to be tuned.

2. Layer width is represented by a discrete uniform distribution bounded between 10 and 30 neurons; $\log_{10} \lambda$ is drawn from a uniform distribution centered on $\log_{10} 1/n$ with a variance of $1/3$, where $n$ is the number of observations in the training set.

3. One hundred random combinations of layer width and $\lambda$ are sampled from the assumed distributions; the widths of the two hidden layers are sampled independently.

4. Each hyperparameter combination is used to train a model five times, subject to a minimum $R^2$ threshold of 0.90 computed on the test set; if $R^2 < 0.90$ for any trained model, that combination is discarded.

5. From the combinations that meet the $R^2$ threshold five times, the combination with the least mean squared error, averaged across the five trials, is selected as the best candidate; one hundred models are trained with this combination to verify its insensitivity to the random elements of the training process.

The hyperparameter combinations listed in Table 3.4 are the best candidates identified by this stochastic optimization procedure. The distributions of $R^2$ across one hundred realized models are summarized in Table 3.5. Some cases required the steps to be repeated, sometimes with adjustment of the layer width bounds, to find a suitable

**Table 3.5.** Robustness of Optimized Hyperparameter Combinations

| Dataset | Minimum $R^2$ | Median $R^2$ | $R^2 > 0.90$ | $R^2 > 0.95$ |
|---|---|---|---|---|
| G5 | 0.965 | 0.981 | 100% | 100% |
| G6 | 0.946 | 0.968 | 100% | 99% |
| H5 | 0.905 | 0.964 | 100% | 90% |
| H6 | 0.965 | 0.984 | 100% | 100% |
| H8 | 0.906 | 0.957 | 100% | 71% |
| S6 | 0.778 | 0.973 | 90% | 75% |
| S7 | 0.854 | 0.986 | 95% | 84% |
| S71 | 0.959 | 0.997 | 100% | 100% |
| S8 | 0.904 | 0.989 | 100% | 89% |

combination. The lower percentile $R^2$ for datasets S6 and S7 illustrate that a hyperparameter combination which performs well on average might still occasionally generate a model that tests far below median if the stochastic aspects of the training fall out unfavorably. This does not require that model S6 or S7 as trained according to Table 3.4 be rejected outright, but it tempers our confidence that the generalizations will always be as good as the test loss suggests. Beyond these rare outcomes, the results are satisfactory, with a substantial majority of realized models, or in some cases all realized models, returning an $R^2 > 0.95$, verifying that the accuracy of the study models is not a product of mere chance.

The reasonableness of model predictions can be checked at a glance by plotting predicted $C_p$ alongside the mean $C_p$ of the wind tunnel time series data as a function of the predictor variables. One approach is to predict $C_p$ at all pressure tap locations associated with a model, average the predictions, and plot the predicted and measured $C_p$ as a function of wind direction for various combinations of roof slope $\beta$ and aspect ratio $h/b$. The resulting plots, presented in Figure 3.5 for gable roofs and Figure 3.6 for hip roofs, illustrate the dependence of surface-averaged $C_p$ on roof geometry and how this dependence changes with wind direction. Every value of $\beta$ and $h/b$ listed in Table 3.1, except 9.4° and 30° gable roof slopes, is represented in these plots. Predictions

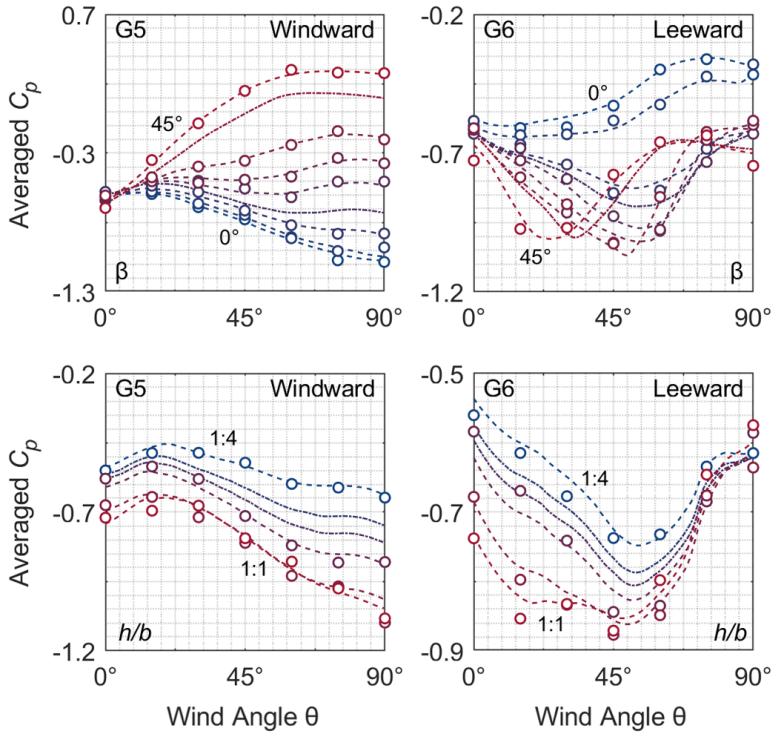


**Figure 3.5.** Surface-averaged $C_p(\theta)$ predictions for gable-roof models G5 and G6. Markers indicate surface-averaged wind tunnel data; dot-dash curves signify cases not found in the TPU database. Wind angle is relative to ridgeline. The top row plots various roof slopes at an $h/b$ of 1:2. The bottom row plots various $h/b$ at a roof slope of 14°.

follow the general shape of the experimental data but do not always precisely intercept them, as would be expected of an overfitted model. Predictions for a few variable combinations not present in the wind tunnel database are plotted here as well: 16° and 37° gable roof slopes, 4.8°, 14°, and 37° hip roof slopes, and 0.36 and 0.42 $h/b$ ratios for both roof types. In every case, predictions form a sort of weighted average between adjacent curves; for geometries within the $h/b$ and $\beta$ test ranges in Table 3.1, the task of pressure prediction is tantamount to multivariate interpolation in the wind tunnel data. Results of the same surface-averaging procedure for roof overhang models S6, S7, and S8 are plotted in Figure 3.7 in terms of various $h/b$. The three tested $h/b$ of 3:10, 3:5, and 9:10 appear together with untested ratios 9:20, 3:4, and

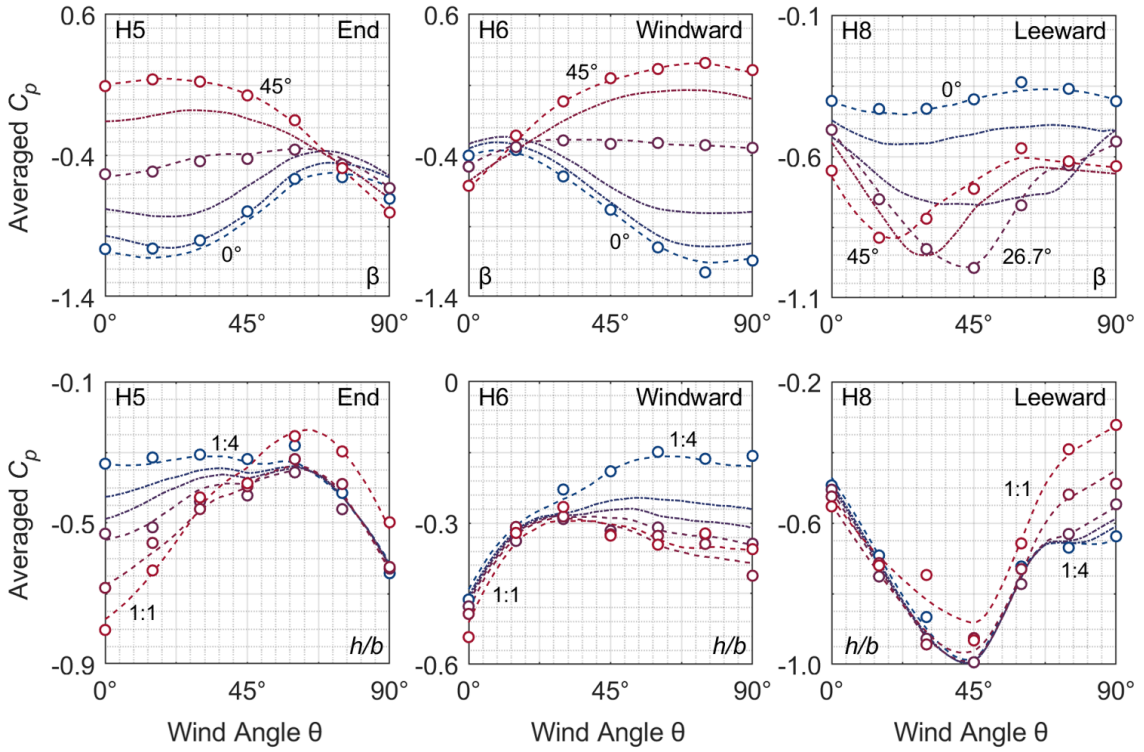


**Figure 3.6.** Surface-averaged $C_p(\theta)$ predictions for hip-roof models H5, H6, and H8. Markers indicate surface-averaged wind tunnel data; dot-dash curves signify cases not found in the TPU database. Wind angle is relative to ridgeline. The top row plots various roof slopes at an $h/b$ of 1:2. The bottom row plots various $h/b$ at a roof slope of 26.7°.

1:1. Model predictions appear to offer reasonable interpolations for the 9:20 and 3:4 ratios as well as a reasonable extrapolation for 1:1.

*Predicted Pressure Distributions*

The output of the pressure prediction step in the procedure is a contour map of $C_p$ on all roof surfaces of the building section under study. Though in principle the trained regression models can generate pressure predictions at any point on the roof plan, predictions are expected to be most accurate at points that coincide with pressure tap locations, where interpolation in $x$ and $y$ is unnecessary, and least accurate at points between roof surface boundaries and the outermost tap locations, which require

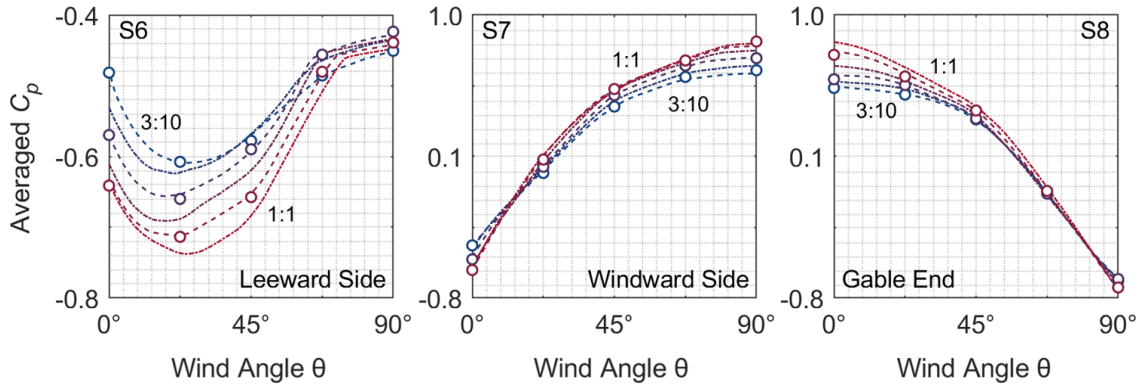


**Figure 3.7.** Surface-averaged $C_p(\theta)$ predictions for roof overhang models S6, S7, and S8 at various $h/b$. (Results for S71 are a mirror of S7 since both are trained on the same data with $\theta$ reversed for S71.) Markers indicate surface-averaged wind tunnel data; dot-dash curves signify cases not found in the TPU database. Wind angle is relative to ridgeline.

extrapolation beyond the pressure tap grid. For this reason, the regression models are used to predict $C_p$ on a grid of points that is similar in extent and density to the roof pressure tap layout on the wind tunnel test models, on the view that this approach affords sufficient prediction resolution and avoids propagating unnecessary error. Predicted pressures are then interpolated on a refined grid as in Figure 3.8, where the contour is developed using modified Akima interpolation. [14] All results presented in this chapter likewise rely on the modified Akima method primarily on the strength of its extrapolations in flow separation regions at eaves and ridgelines, which tend not to be rendered well by lower-order methods like linear or nearest-neighbor extrapolation. [15] For analyses that consider roof overhang effects, lower-surface $C_p$ are similarly predicted at approximate pressure tap resolution and interpolated along

[14] The mathematical formulation of this algorithm, as it is implemented in MATLAB, is documented at `https://www.mathworks.com/help/matlab/ref/makima.html`.

[15] Contours formed by modified Akima interpolation compare well to local $C_p$ contours retrievable from the TPU databases, though it is unclear which interpolation method has been used to generate those contours.

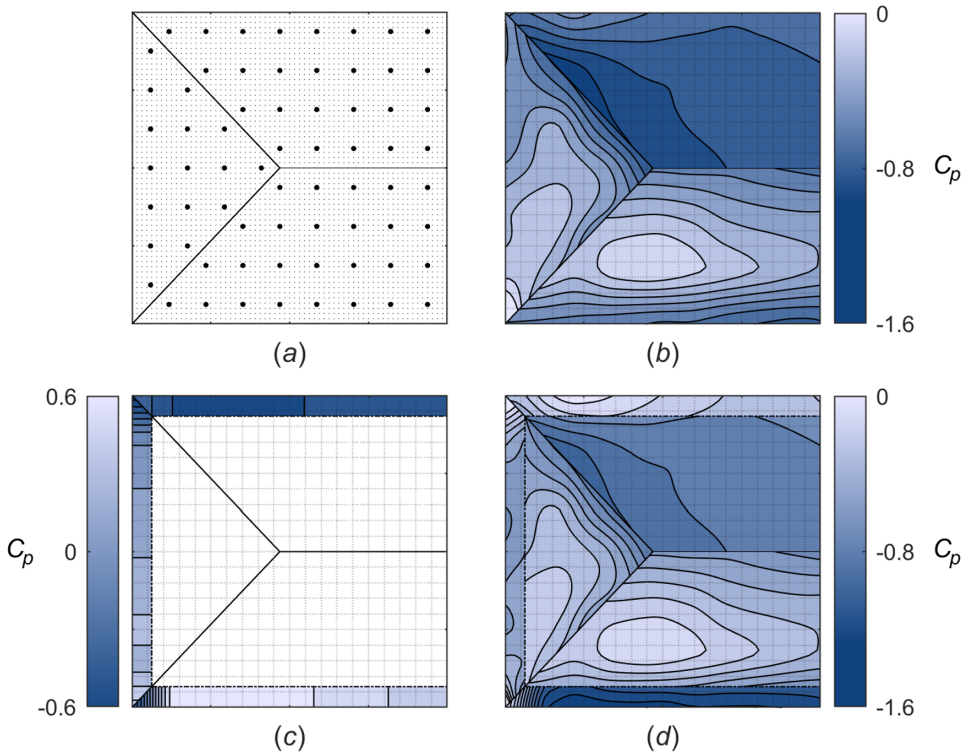


**Figure 3.8.** Pressure contour development for a hip roof with a 26.7° slope and an $h/b$ ratio of 1:2. The wind angle is 60° relative to ridge. ($a$) $C_p$ are predicted on the coarse grid of points and interpolated on the fine grid, spaced at $b/8$ and $b/160$ respectively. Predicted $C_p$ on ($b$) roof upper surfaces and ($c$) lower surfaces of overhangs are ($d$) superimposed to estimate net uplift.

the length of the eave. Overhang pressures are assumed invariant along the depth of the eave, since test data are limited to a single row of pressure taps. The contour of lower-surface $C_p$ is then subtracted from the upper-surface contour as in Figure 3.8. The resulting superposition represents the net uplift due to the presence of the overhang. [16]

[16] This superposition approach follows the reasoning of the procedure for estimating roof overhang design pressures described in ASCE 7-22, Section C30.3.2.

### 3.1.4. Spatial Averaging and Indexing Approaches

Following modeling premise ($b$) previously stated, roof uplift pressure intensity is regarded as a bellwether of a low-rise building's aerodynamic vulnerability as a whole. Once the distribution of time-averaged $C_p$ has been predicted at wind angle $\theta$, uplift intensity at that wind angle can be estimated by computing a spatial average of $C_p$ across the roof plan and returning the most extreme value. This worst-case spatial average is designated $\bar{C}_p$. Over what areas should pressures be averaged? It seems best to describe wind vulnerability in terms of multiple averaging areas. Analogous to the distinction in ASCE 7 between component and cladding elements and the main wind force resisting system, analysis options fall into two basic categories:

1. For component-scale vulnerability, pressures are averaged within windows that correspond to the area of a roof component or cladding element, such as a roof shingle or sheathing panel.

2. For structure-scale vulnerability, pressures are averaged within the tributary areas of one or more roof framing members or across the entire roof surface, depending on the degree of load-sharing behavior assumed.

At a minimum, an informative vulnerability analysis should include averaged pressures representative of framing member loads and roof substrate loads. From the perspective of the load path resistance model laid out in Chapter 2, these pressures would correspond to those directly resisted by the roof-to-wall connection and roof sheathing panel connections respectively. An evaluation at the scale of roof cover could also be of practical use for assessing risk of rainwater ingress, for example.

Beyond the question of scale, area averaging can be implemented programmatically in at least two ways. (1) The roof surface can be subdivided into fixed, non-overlapping averaging windows representing, for instance, a typical staggered array of sheathing

panels. (2) A two-way moving average can be computed within a certain $x$ and $y$ distance of each point on the roof surface, effectively using overlapping averaging windows. The second approach would in general return a more conservative load estimate by locating $\bar{C}_p$ more precisely. By either approach, a further question to address is how to average along diagonal roof surface boundaries. Taking roof sheathing panels as an example, how should the analysis handle partial panels installed along hip rafter lines? The evaluation could be limited to full-size panels, but since uplift pressures are often most severe in the lee of hip rafters, disregarding the presence of partial panels there risks substantial underestimation of uplift intensity and would be out of step with a central premise of the analysis. Yet merely averaging $C_p$ within each panel without some adjustment for reduced area would produce inconsistent results in an analysis that is meant to be universally referenced to the size of a standard sheathing panel. One possible solution is to down-weight the averaged $C_p$ of a partial panel by the ratio of its area to the area of a full-size panel. Using averaging approach (2) described above, this would be equivalent to drawing a bounding box around the roof surface, computing a two-way panel-sized moving average within the bounding box, and multiplying each averaged result by the percent overlap between the averaging window and the actual roof surface. For components and cladding, this operation implicitly assumes that the uplift demand-to-capacity ratio decreases as component area decreases, an approximation that is qualitatively justified by recognizing that the tributary area of the controlling fastener tends to grow smaller as the component as a whole becomes smaller. The down-weighting operation involves less approximation for structural loads, where the uplift demand on a roof-to-wall connection is effectively scaled in proportion to its tributary area.

Once the pressure prediction and spatial averaging steps have been carried out for all wind directions, the analysis procedure concludes by deriving an index from

the $\bar{C}_p(\theta)$ uplift intensity curve that represents the aerodynamic vulnerability of the building. Numerous index definitions are possible, and at this stage the best formulation remains a question for later study and validation. On the view that the index should convey a sense of both the expectation and uncertainty in the predicted uplift intensities, it is proposed here that the product of the median and an upper percentile value of the $\bar{C}_p(\theta)$ distribution lends itself to a useful index.

### 3.2. Comparison to Design Values

Before turning to a survey of analysis results, it may be helpful first to consider how the proposed method's area-averaged $C_p$ predictions compare to design values for wind uplift. The design pressure coefficients for components and cladding provided in ASCE 7-22 are referenced to the three-second gust pressure at mean roof height and assume open terrain. [17] Predicted pressure coefficients are referenced to a ten-minute average wind speed at mean roof height and assume suburban terrain. Further, the prediction models developed in this study are trained on the mean of the ten-minute TPU time histories, while the design values of ASCE 7-22, Chapter 30, are based on spatially averaged peaks from the underlying time histories. The net effect of these differences is that $C_p$ predicted in this study tend to trail behind the corresponding design $GC_p$, though not always to the same degree. Design $GC_p$ also represent worst-case pressures enveloped over ranges of roof slopes, further widening the gap between predictions and design values.

The comparisons in Figure 3.9 illustrate the characteristic margin between uplift design values and model predictions for standard roof sheathing panels. Comparisons

[17] Open terrain here refers to Exposure C. Some design $GC_p$ values also apply to Exposure B; see ASCE 7-22, p. 915.

are made for gable and hip roofs at 5:12 and 8:12 slopes and assume a rectangular plan measuring 9.14 m normal to ridgeline, with 1.22 m by 2.44 m sheathing panels arranged in a staggered layout to a depth of 8.53 m parallel to ridgeline. Predictions assume a 4.57 m eave height and are swept across a 180° range of wind directions in 22.5° increments, starting at 90° relative to ridgeline on the windward side and moving to the leeward side. The color gradient in Figure 3.9 is a function of wind direction, where blue markers represent windward-side pressures and red leeward. Predicted $C_p$ are averaged within each panel regardless of panel area. For the hip roof cases, panel-averaged $C_p$ on the hip-end surface are plotted on the left-hand side of the vertical dashed line and side-surface panels on the right. Cross-circle markers denote negative $GC_p$ design values provided in ASCE 7-22, Chapter 30. The design $GC_p$ of each panel is an average of zone-specific $GC_p$ weighted by the relative panel area present within each roof zone. The effective wind area is taken as the geometric area of the panel up to a maximum of 2.23 $m^2$. [18] Design values for areas less than 0.93 $m^2$ are not extrapolated beyond the truncation point, and panels less than 0.37 $m^2$ in area are left out of the comparison.

Though far from exhaustive, these four cases demonstrate a general correlation between negative design $GC_p$ and the most negative $C_p(\theta)$ predicted by the models across nine representative wind directions. A search for the wind angle producing the worst-case predicted uplift in each panel would yield a somewhat closer match. Because ASCE 7 necessarily groups similar geometries together and limits the number of roof pressure zones to reduce complexity in the design procedure, perfect correlation is not to be expected. The degree of correlation observed nevertheless may be taken

[18] For standard 1.22 m by 2.44 m panels, Szilagyi (2022) has found 2.23 $m^2$ to be a suitable effective wind area.

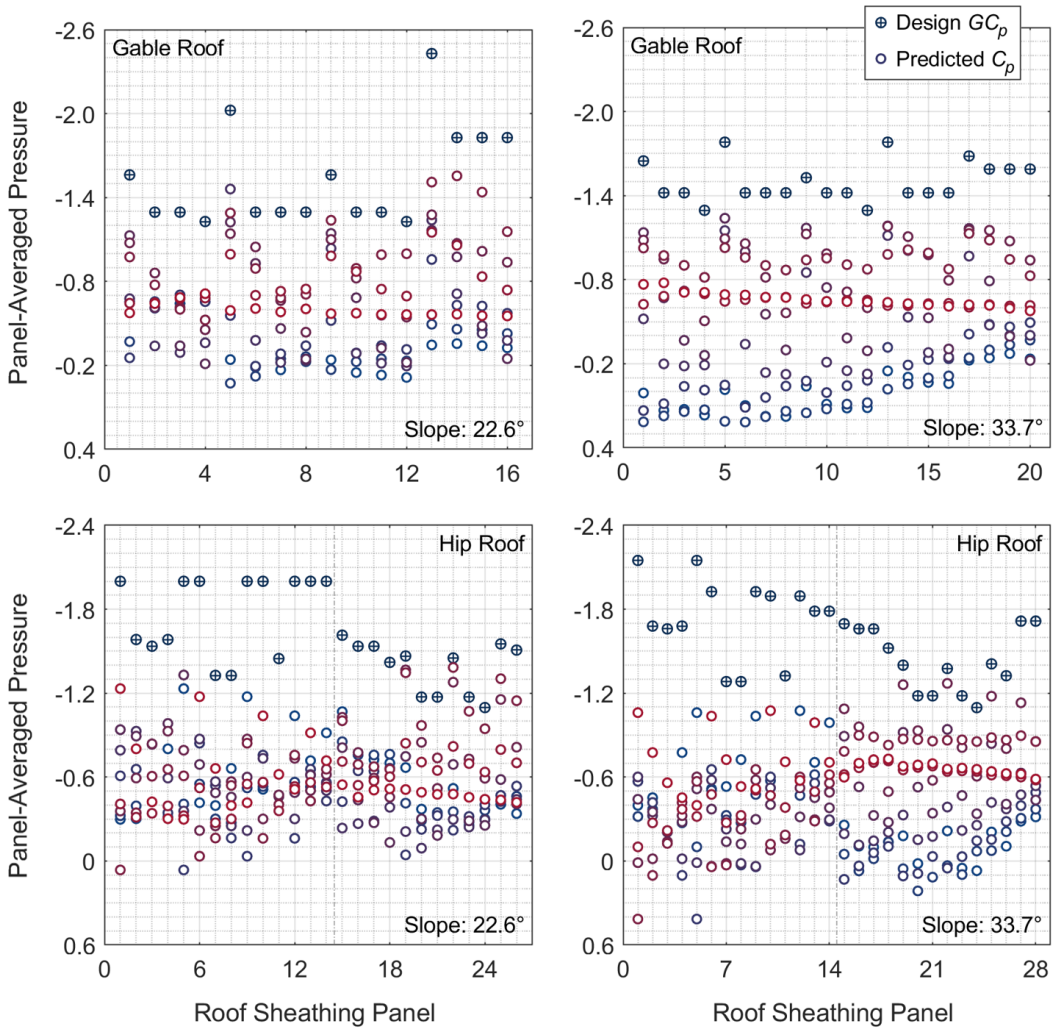


**Figure 3.9.** Comparison of negative design $GC_p$ to panel-averaged $C_p$ predicted for various wind directions for typical roof sheathing panel layouts on gable and hip roofs at 5:12 and 8:12 roof slopes. The predicted $C_p$ color gradient is a function of wind direction. Design values are from ASCE 7-22, Chapter 30, where $GC_p$ are area-averaged by roof zone within each panel.

as a secondary form of model validation. Further, since the ASCE 7 design values presuppose the worst-case wind direction, comparisons like those in Figure 3.9 suggest the value of a generalized method by which the expected pressure demands for a known wind angle may be predicted in a manner that is broadly consistent with ASCE 7, especially for post-windstorm investigation of building performance. The prediction framework presented here may be readily applied to this purpose.

**Table 3.6.** Example Building Geometries

| | G | G1 | G2 | H | HG1 | HG2 |
|---|---|---|---|---|---|---|
| Principal Roof Shape | Gable | Gable | Gable | Hip | Hip | Hip |
| Intersecting Gables | None | One | Two | None | One | Two |
| Footprint Area, $m^2$ | 139 | 153 | 179 | 139 | 153 | 179 |

### 3.3. Analysis Results

The analysis procedure is applied now to a set of example buildings that are intended to represent a broad subset of single-family residences, summarized in Table 3.6. Cases G and H are regular gable and hip-roof buildings 9.1 m by 15.2 m in plan. An intersecting gable-roof section is added along the length of G and H to form cases G1 and HG1; cases G2 and HG2 similarly have two intersecting gables on opposite elevations. Eave height and roof slope are identical across all cases. Roof overhang effects are not considered.

Uplift intensity curves for the example cases are plotted in Figures 3.10 and 3.11 along with roof geometry diagrams. Comparing cases within each figure illustrates the effect of increasing roof complexity, all else being equal. Comparing like cases across the two figures illustrates the relative vulnerability of predominantly gable and hip roof shapes at three levels of roof complexity. Predicted $C_p(\theta)$ are moving-averaged at three scales. The roof cover and roof substrate curves are respectively developed using 0.30 m by 0.91 m and 1.22 m by 2.44 m averaging windows, where in both cases the averaging window is oriented as a typical roof shingle or sheathing panel would be installed. The roof structure curves use a variable-length averaging window that measures 0.61 m in width along the wall and spans from eave to ridgeline. The structure-scale averaging method approximates the tributary load to a single underlying roof-to-wall connection, assuming that uplift is resisted only by roof-to-wall connections distributed along the exterior walls at a 0.61 m spacing. $\bar{C}_p(\theta)$ are evaluated in 10° increments, and intensity

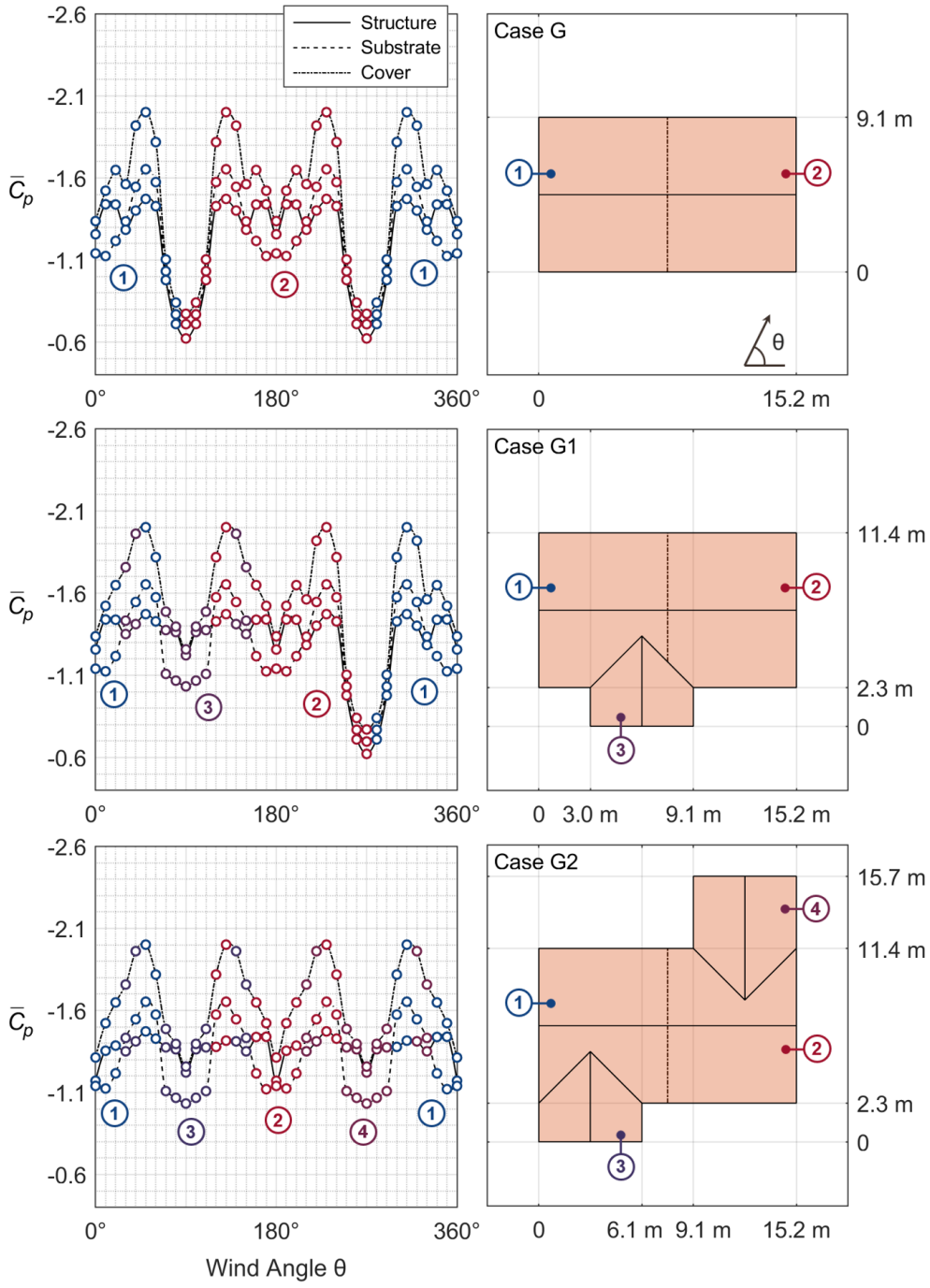


**Figure 3.10.** Uplift intensity predictions for a regular-plan gable roof and two cross-gable roofs. $C_p$ are evaluated within the upwind roof section(s) for each wind direction and averaged at scales representative of roof structure, roof sheathing, and roof cover loads. All cases assume a 5:12 roof slope and an eave height of 2.74 m.

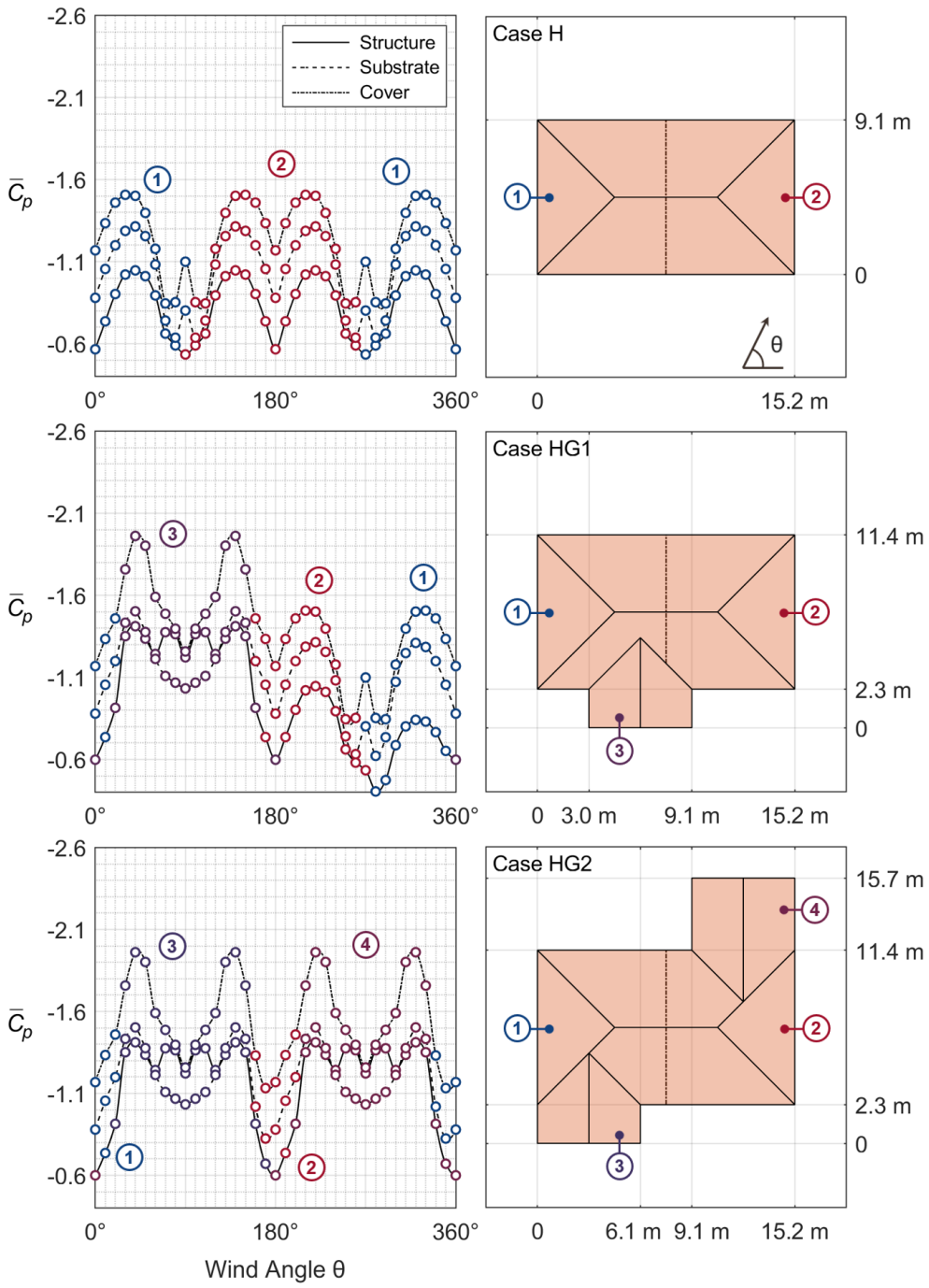


**Figure 3.11.** Uplift intensity predictions for a regular-plan hip roof and two combination hip-gable roofs. $C_p$ are evaluated within the upwind roof section(s) for each wind direction and averaged at scales representative of roof structure, roof sheathing, and roof cover loads. All cases assume a 5:12 roof slope and an eave height of 2.74 m.

curves are smoothly interpolated between evaluations. The numbered annotations and color palette of the plot markers indicate the upwind section of the building in which $\bar{C}_p$ occurs at each $\theta$.

Case G in Figure 3.10 exhibits the characteristic aerodynamics of gable roofs. At all spatial scales, uplift pressures are least intense for winds normal-to-ridge, moderate for parallel-to-ridge, and most intense for quartering winds. The presence of an intersecting gable in case G1 blunts the normal-to-ridge aerodynamic advantage for wind angles between 70° and 110°, and the additional gable section in G2 does likewise between 250° and 290°. One perhaps counterintuitive feature of the gable-roof results is that the averaged roof structure load is greater at many wind angles than the averaged load for roof substrate. The reason is that the substrate-scale averaging window is oriented more favorably than the structure-scale averaging window for $\theta$ within 20° of parallel-to-ridge, where the strongest uplift occurs along the gable-end rakes. In sections (3) and (4), the 2.98 $m^2$ averaging area for substrate is also greater than the 2.01 $m^2$ structure-scale averaging area. In general, the severity of predicted roof sheathing loads increases relative to roof structure loads as the footprint of the building increases.

The fundamental aerodynamic advantage of hip roofs can be seen by comparing case G in Figure 3.10 to case H in Figure 3.11. Uplift intensities in case H fall below those of case G for all wind directions except normal-to-ridge, where the analysis finds more severe substrate and cover-scale uplift in the lee of the hip rafters. Peak intensities at all scales in H are 20–30% less than in G, though these margins would be smaller for a less steep roof. Intersecting gable (3) in case HG1 has an intensifying effect between 20° and 160° similar to that seen in G1, but the structure-scale intensity in HG1 is slightly attenuated between 270° and 350° relative to H. This occurs because the presence of section (3) reduces the area of the adjacent hip surface in section (1).

Whenever section (1) is upwind, pressures are predicted on the section surfaces as if gable (3) were absent, but the polygonal area of gable (3) is subtracted from section (1) before averaging. The resulting averaged pressures on the leeward surface of section (1) are approximate, since the controlling flow separation behavior along the hip rafter is likely altered to some degree by the presence of the downstream intersecting gable. Lacking a better estimate, the analysis supposes the state of pressure near the hip rafter and ridgeline to be the same as in case H but averages only within the surface area not intersected by gable (3). The substrate and cover-scale averages are unaffected, but the now-constrained structure-scale average finds lower roof framing loads than before. The second intersecting gable in HG2 amplifies uplift pressures between 200° and 340°. The strongest uplift occurs along the hip rafters only near 0° and 180°. The controlling uplift is found in one of the intersecting gables at all other wind directions.

### 3.3.1. Parameter Dependence

How would the analysis results presented above change if the roof slope or eave height of the example buildings were different? The question of building attribute influence on wind vulnerability is explored more thoroughly in Chapter 4, but a partial answer is given here in Figure 3.12, which plots the $\bar{C}_p(\theta)$ intensity curves for building HG2 at various roof slopes and eave heights. The left-hand column keeps the eave height at 2.74 m and plots $\bar{C}_p$ at six common roof slopes between 1:12 and 12:12. The right-hand column considers 2.44, 3.66, 4.88, and 6.10 m eave heights while holding the roof slope at 5:12. The associated $h/b$ aspect ratios are between 0.27 and 0.67 for the hip-roof sections of HG2 and between 0.40 and 1 for the intersecting gables, which remain within the prediction model training bounds. The color gradient moves from blue to red as the parametric variable rises in value. In the case of variable roof slope, the

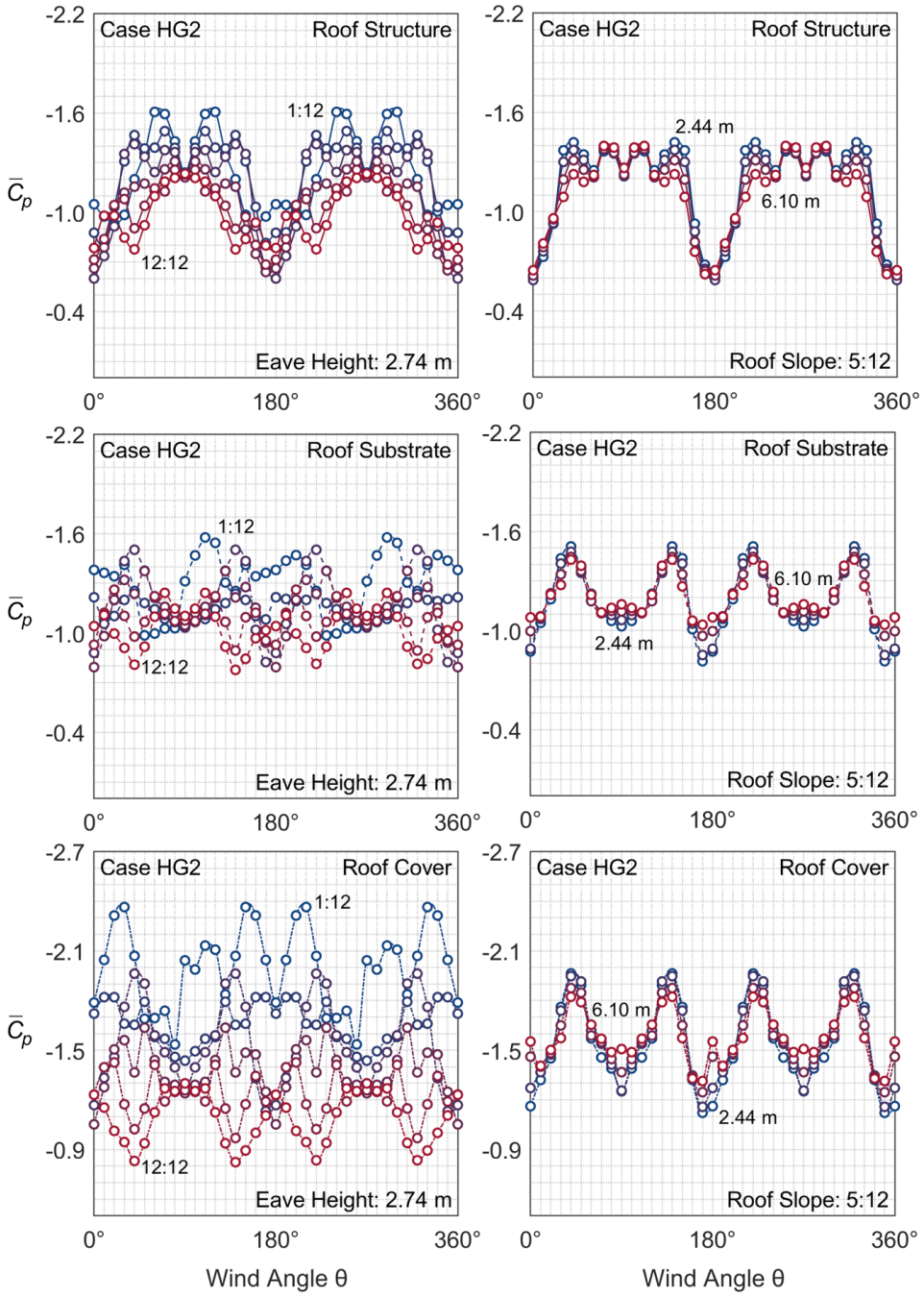


**Figure 3.12.** Dependence of uplift intensity predictions on roof slope and eave height for building HG2. The left-hand column plots various roof slopes at constant eave height; various eave heights at constant roof slope are plotted at right.

results agree with intuition in several respects. Roof slope dependence, visualized by vertical dispersion in the intensity curves, is strongest for quartering-wind directions

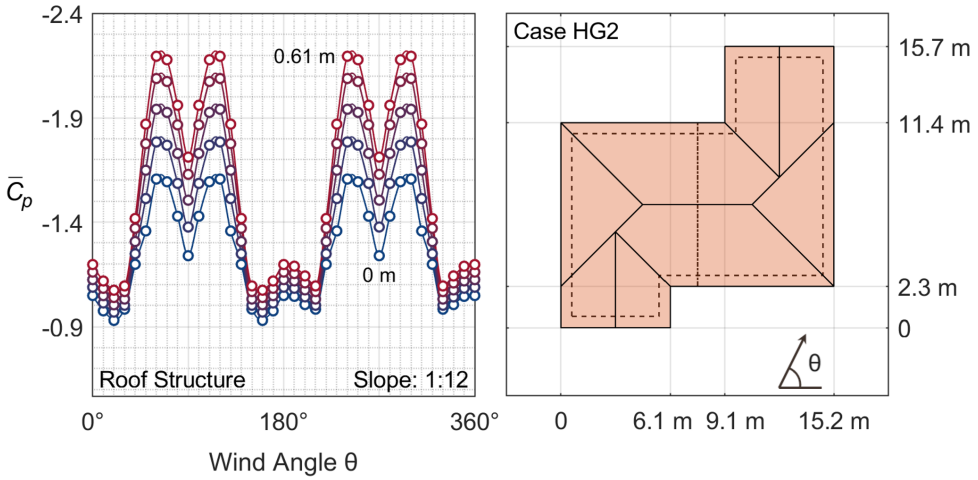


**Figure 3.13.** Effect of roof overhang depth on uplift intensity. Predictions are averaged at roof structure scale for building HG2, assuming a 1:12 roof slope and a 2.74 m eave height.

across all spatial scales. Conversely, uplift intensity is least sensitive to roof slope for winds parallel to the intersecting gable ridgelines at 90° and 270°. The analysis also expects median and peak uplift intensities to decrease with rising roof slope at all spatial scales and especially so at roof cover scale. The slope-uplift relationships are not strictly monotonic however, and the plotted distributions make clear that the real advantage of one slope over another is dictated by the prevailing wind direction. Looking to the right-hand side of Figure 3.12, uplift intensity is seen to be far less sensitive to eave height than to roof slope. At substrate and cover scales, predicted median intensity increases by less than 5% as eave height rises from 2.44 m to 6.10 m, but peak intensity decreases by about the same amount. At structure scale, median intensity decreases by 8% over the same eave height range, a consequence of gable-roof quartering-wind behavior in the 45° and 225° sectors whereby uplift along the rake of the leeward gable surface becomes less severe as height increases. The relationships vary somewhat for other roof slopes, but the relatively weak uplift-height dependence holds true in general.

How does consideration of roof overhang pressures affect the vulnerability analysis? First, it is expected that overhang pressures are meaningful only to roof structure load estimation, on the view that attic pressure equalization inhibits loading of sheathing panels from the inside of the overhang but does not preclude load transfer between the soffit and the adjoining roof framing members. Following the $C_p$ superposition procedure described previously and depicted in Figure 3.8, geometry HG2 is evaluated at roof structure scale for five overhang depths evenly spaced between 0 and 0.61 m, assuming a roof slope of 1:12 and an eave height of 2.74 m. The results are plotted in Figure 3.13. The impact is minimal for the hip-controlled wind directions — within 30° of parallel to the hip ridgeline — but the effect on gable roof structural loads is substantial. The analysis expects peak structure-scale intensities in case HG2 to be amplified by 21% by the presence of a 0.30 m overhang and by 36% by a 0.61 m overhang. This relative sensitivity to overhang depth can be considered characteristic of gable roofs. For winds oriented within about 40° of parallel to the gable ridgeline, the controlling flow separation zone typically forms near the rake regardless of roof slope. The roof-to-wall connection that resists the most negative upper-surface pressure load thus often resists the greatest positive lower-surface pressure load at the same time, a correlation that does not occur in hip roofs. One additional observation to note here is that the results in Figure 3.13 approach a worst-case outcome. Though overhang pressures are not predicted as a function of roof slope, their effect is greatest for shallow roofs where uplift is controlled by flow separation near the eaves rather than at ridgelines. Increasing the roof slope beyond the 1:12 slope selected for this example dampens, but never eliminates, the gable-roof amplifying effect. It is noted as well that the wind tunnel models on which the pressure predictions are based have impermeable overhang surfaces. Far more often than not, overhang soffits installed on homes are air-permeable to allow attic ventilation, relieving soffit pressure and

reducing the load transferred to the roof framing. For these reasons the Figure 3.13 uplift intensities are best interpreted as representative upper-bound results.

### 3.3.2. Vulnerability Indexes

Returning to the series of results presented in Figures 3.10 and 3.11, it is clear that different levels of aerodynamic demand characterize the various geometries. The relative vulnerability of these buildings can be judged from the data in two ways. (1) If conditioned on a known or presupposed wind direction, relative vulnerability can be read directly from the intensity curves. This would be the approach of post-event analysis. In a population of buildings subject to peak wind speeds at a certain prevailing wind direction, some part of the variability in observed performance can often be traced to a more or less favorable aerodynamic setting. Even two homes that are built to identical specifications, both in structure and in shape, may come to different damage states merely for being located on opposite sides of the street. (2) To answer the vulnerability question more generally, wind direction must be considered unknown. From this perspective, a useful vulnerability measure must in some way take account of the load intensity distribution with respect to wind angle. Comparing only median-to-median or peak-to-peak across cases, for example, is informative but by itself does not tell the whole story, since it offers no sense of the range of outcomes.

If all wind angles are assumed equally likely, the Figure 3.10 and 3.11 uplift intensity curves follow the cumulative distributions depicted in Figure 3.14, where the markers indicate the minimum, 50th percentile, 90th percentile, and peak intensities. As expected, comparing the distributions in this form clearly distinguishes the basic hip-roof shape of case H as the least vulnerable of the example geometries. It also supports some perhaps less intuitive conclusions. The statistical similarity across cases G, G1, and G2, in terms of median and upper percentile values, suggests that

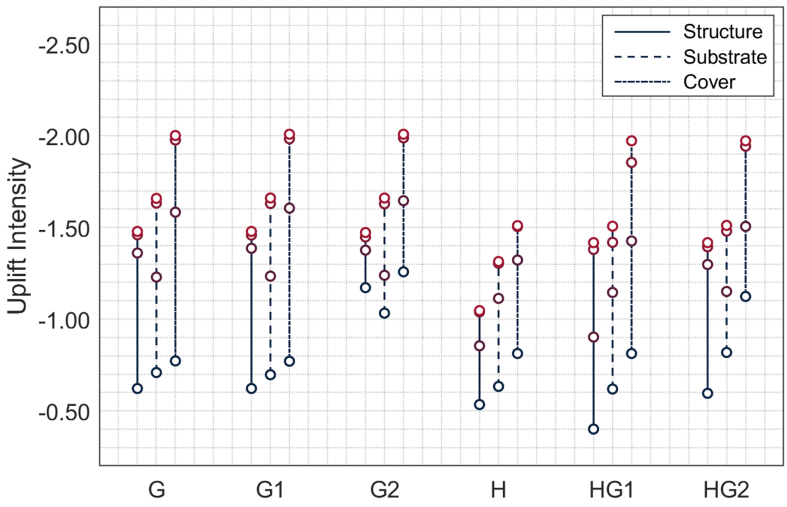


**Figure 3.14.** Predicted uplift intensity distributions $\bar{C}_p(\theta)$ averaged at roof structure, roof sheathing, and roof cover scales for the example geometries, assuming a 5:12 roof slope and an eave height of 2.74 m without roof overhang effects. Lines indicate the range of values across all wind angles; markers denote the minimum, 50th percentile, 90th percentile, and peak intensities.

a basic gable-roof shape is, on average, not disadvantaged by the addition of one or more intersecting gables. The presence of intersecting gables has a clear effect on the vulnerability of the regular hip roof however. Relative comparison of different cases requires a holistic consideration of the load intensity distributions. It is suggested here that a robust vulnerability index can be found in the product of uplift intensities at two specified percentiles. If the 50th and 90th percentiles are used, for instance, the example buildings would be indexed as summarized in Table 3.7. The rationale behind this selection is that the median intensity represents a most-likely outcome while the 90th percentile intensity represents a near-worst-case outcome, both of which should inform the vulnerability estimate. This formulation also comports well with the magnitude of the $C_p$ predictions to generate numerically convenient indexes that loosely fall in the range 0.9–2.0 at roof structure scale, 1.5–2.0 at substrate scale, and 2.0–3.3 at roof cover scale.

**Table 3.7.** Suggested Vulnerability Indexes

| Index Scale | Averaging Area | G | G1 | G2 | H | HG1 | HG2 |
|---|---|---|---|---|---|---|---|
| Roof Structure | *Variable* | 1.99 | 2.02 | 1.99 | 0.89 | 1.24 | 1.81 |
| Roof Substrate | 1.22 m × 2.44 m | 2.01 | 2.01 | 2.02 | 1.45 | 1.62 | 1.70 |
| Roof Cover | 0.30 m × 0.91 m | 3.13 | 3.18 | 3.27 | 1.99 | 2.64 | 2.92 |

### 3.4. Comparison to Wind Tunnel Studies

As a closure to this analysis, we consider two irregular buildings for which high-resolution wind tunnel data are available. Peng *et al.* (2014) document the wind tunnel test procedure and the building geometries, which are based on two residences located in the Florida panhandle. [19] The experimental $C_p$ values in this dataset are referenced to mean roof height and assume suburban terrain as in the TPU datasets. The geometries, designated FL-27 and FL-30, are depicted in the upper row of Figure 3.15. FL-30 is a regular gable-roof building with two intersecting gables on the front elevation. FL-27 features a secondary gable-end on each side elevation and two nested gables at front. The middle and lower rows in Figure 3.15 present the predicted uplift intensity curves for these geometries, averaged at the scale of roof structure and roof sheathing loads, alongside experimental pressures spatially averaged at the same scales. The experimental averages are obtained by computing the mean $C_p$ of the time series for each pressure tap and interpolating on a fine grid within each roof surface. The experimental value at any wind direction represents the greatest measured uplift intensity anywhere on the roof. The model uplift intensity, as before, considers only upwind roof sections as defined in Figure 3.2.

[19] The analysis of Peng *et al.* relies on test data collected at only three wind directions, but the complete wind tunnel dataset includes measurements at all directions in 10° increments. The present comparison uses this larger dataset.

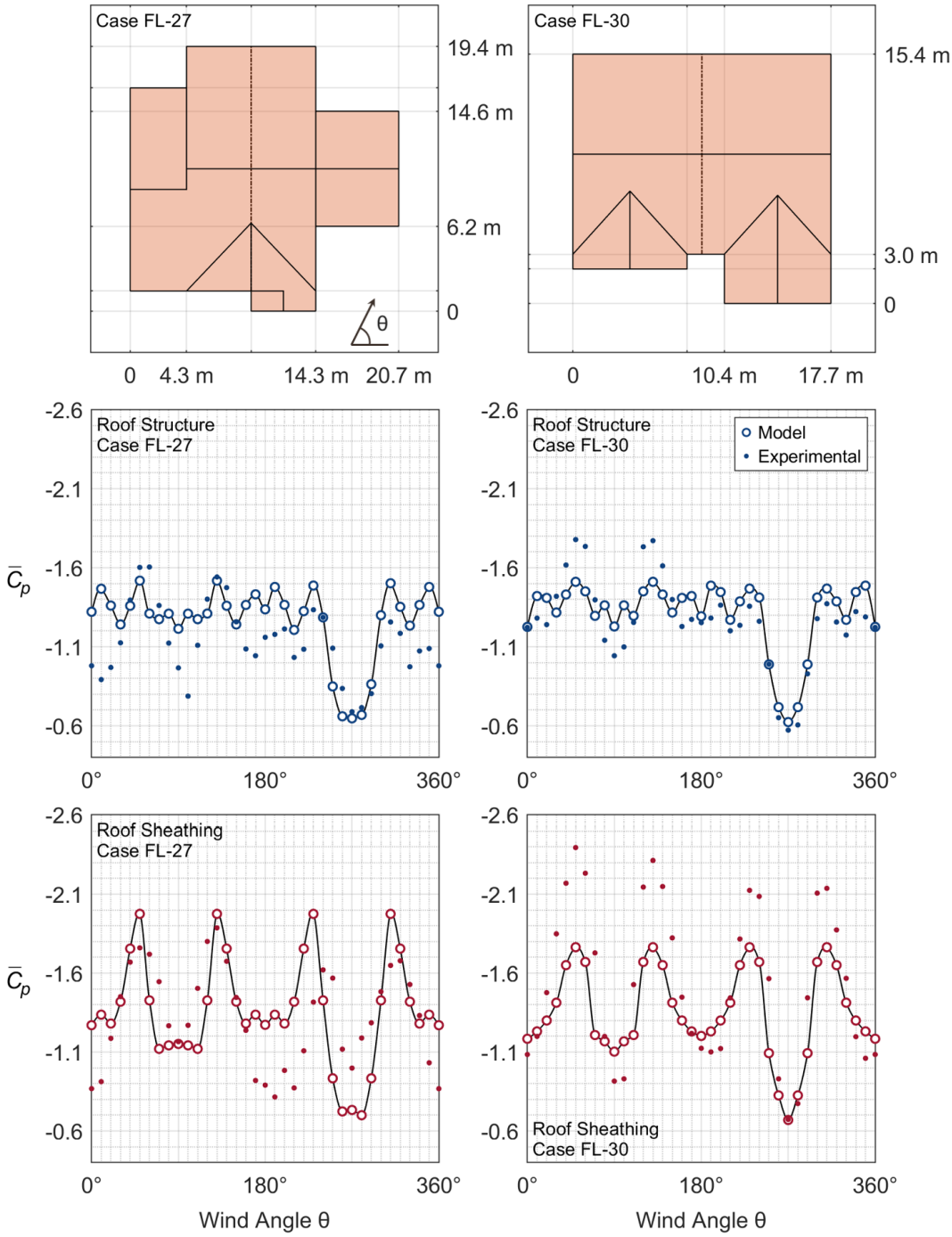


**Figure 3.15.** Uplift intensity predictions for two irregular buildings, averaged at roof structure scale and roof sheathing scale. Dot markers indicate corresponding spatial averages of time-series mean $C_p$ collected from wind tunnel studies of these geometries, described in Peng *et al.* (2014).

Inspection of the experimental roof pressure distributions bears out the expectation, stated earlier as modeling premise ($c$), that the most severe uplift occurs in upwind roof sections. [20] This is true for cases FL-27 and FL-30 at all wind angles. Error between the model predictions and the experimental values is therefore not in principle driven by premise ($c$). Instead the error primarily arises because the predictions rely on regular-plan aerodynamic data. This appears to be why, for example, the model underpredicts the uplift intensities near 50° and 130° in FL-30. The model and the experimental results locate the controlling uplift in the same region near the main gable ridgeline, but the experimental data indicate stronger local uplift than the model expects, which seems a likely consequence of the front-facing secondary gables altering the aerodynamics. For both buildings, predicted $\bar{C}_p(\theta)$ are more accurate when averaged at roof structure scale than at sheathing scale, due at least in part to the larger averaging area, but the experimental intensities tend to follow the general shape of the predicted intensity curve at both spatial scales. Overall the comparison appears to support the reasonableness of the model as a means to estimate uplift intensity.

### 3.5. Summary

This chapter has presented a general analysis method to assess aerodynamic vulnerability in low-rise buildings with arbitrary footprints and any combination of gable and hip roof shapes, demonstrated its use on several representative buildings, and proposed a vulnerability indexing system tied to predicted roof uplift intensities. This method has been developed to address a present need in wind performance research —

[20] In other words, uplift intensity is greatest along eaves or ridgelines of roof surfaces located on the upwind side of the building.

a way to quantify and compare the aerodynamics of a wide array of realistic low-rise buildings — that existing methods cannot at this stage thoroughly and economically meet. The catalog of published wind tunnel studies is continually growing, including tests of irregular building models, but a vast number of geometries remain to be tested. The same is true of computational fluid dynamics, where computational cost constrains the development of an extensive library of envelope pressures at sufficient resolution. The method proposed here is offered not as a permanent alternative to either of these avenues of analysis, but as a time-efficient means to an approximate solution. At the same time, the method is complementary to wind tunnel and CFD approaches in the sense that its predictive capacity can be continually broadened and strengthened by training on new aerodynamic data, and more powerful prediction models can in turn augment aerodynamic datasets by filling in the parametric gaps.

The modeling premises behind the proposed method, stated at the outset of this chapter, point to the primary ways in which the method's accuracy and scope can be improved, namely ($a$) training on data for other roof shapes and common roof features like stepped gables, ($b$) accounting for combined uplift and lateral wind forces in the vulnerability estimate, and ($c$) expanding pressure prediction to the whole building rather than restricting it to the upwind section. Addressing premise ($c$) likely presents both the greatest potential for advancement and the greatest challenge, since there is no rational basis for estimating downwind pressure distributions in complex geometries apart from tailored CFD or wind tunnel data. It is expected that the upwind-section assumption will eventually no longer be needed as realistic irregular plans are systematically represented in aerodynamic datasets. Continuing development of such datasets would eventually open the door to new machine learning models that can directly generalize to untested complex geometries.

The method has been designed primarily with post-windstorm applications in mind.

One intended use is to estimate relative aerodynamic vulnerabilities in a population of buildings subject to a certain wind field. In other words, given the conditions of a certain wind event, how much variability in performance can be attributed to differences in aerodynamics? An uplift intensity analysis like that demonstrated for the example buildings in this study can be completed for hundreds of geometries with a run-time on the order of minutes. [21] An analysis conditioned on a specified wind sector requires far less time, generating rapid vulnerability estimates for even large hurricane-scale swaths of impacted buildings. Another planned application is dimensionality reduction in post-event datasets. As part of a broader effort to develop a statistical inference framework for understanding windstorm performance of residential buildings, the proposed indexing system suggests a rational way to condense several aerodynamic factors into a single latent variable. Pending validation against observed performance data and iterative reformulation as needed, the aerodynamic vulnerability index may be a strategic means to reduce the large number of variables presently reflected in windstorm performance datasets.

[21] This approximate processing time does not include the time required to encode building geometries into input files. The method in its current form requires data entry by hand, but a computer-vision utility for automated roof geometry processing is an anticipated near-term development task.

# Chapter 4

## Sensitivity Analysis of Structural and Aerodynamic Vulnerability

The previous two chapters addressed structural and aerodynamic vulnerability as separate questions, examining (1) how the properties of the structural load path in a building determine its resistance to wind uplift and (2) how building geometry affects the intensity of wind uplift loads. These complementary analyses operated on models of resistance and load that were developed to take a more systematic account of structural and aerodynamic factors than prior studies have done. This chapter now applies a sensitivity analysis method to these load and resistance models to examine the nature of uncertainty in wind vulnerability. The motivating question up to this point has been: if two buildings are identical in terms of structural character but different in aerodynamics, or *vice versa*, how much more vulnerable to wind damage is one than the other? At this stage the question becomes: how do uncertainties in structural and aerodynamic characteristics drive uncertainty in wind performance?

Sensitivity analysis may be broadly defined as an effort to understand how the output of a model is influenced by one or more input parameters to the model. Methods differ in scope and in mathematical basis. The basic line of distinction with respect to scope is between *local* and *global* methods. [1] The results of a local analysis are valid for a limited subset of model input conditions; global analyses take account of the entire parameter space and so provide a more robust picture of model behavior. The concept of conditional variances forms the mathematical basis of one class of global methods known as variance-based methods, whereby the variance in the output of

[1] Refer to Saltelli *et al.* (2008), pp. 10ff, for an introduction to the local-global distinction.

a model is apportioned to the input parameters according to how much uncertainty each contributes to the model. [2] Many studies across a range of disciplines have applied variance-based methods to numerical models of physical processes, including structural performance studies. As a few examples, variance-based analyses have been carried out by Wan *et al.* (2017) to examine how the density and elasticity of cable-stayed bridge components influence dynamic response and by Khaneghahi *et al.* (2019) to study the importance of various mechanical properties to tensile stress and displacement in concrete arch dams. Metwally *et al.* (2022) similarly analyzed how the mechanical properties of reinforced concrete masonry walls influence out-of-plane load and deformation capacity. Variance-based methods have also been applied to study uncertainty in loss prediction models, as Cremen and Baker (2021) have done, and to guide retrofit decisions on the basis of expected infrastructure disruption costs as in Bhattacharjee and Baker (2021). This survey of examples, to which more could be added, suffices to illustrate the usefulness of variance-based sensitivity analysis in the domain of structural performance and justifies adoption of the same approach in the present work.

This chapter first presents separate sensitivity analyses of the resistance and load models developed in earlier chapters. The sensitivity of uplift resistance to the underlying structural parameters is investigated for roof sheathing and roof-to-wall connections in Sections 4.2.1 and 4.2.2, while Section 4.2.3 explores the sensitivity of system-level resistance to the constituent connection resistances in a typical load path. The analysis next considers the influence of building geometry on uplift load intensity; Section 4.3.1 conditions the analysis on specific wind directions and Section 4.3.2 con-

[2] Saltelli *et al.* make a summary argument for the advantages of measuring sensitivity in terms of variance on pp. 157–158.

siders the influence of geometry and wind direction together. The analysis concludes by joining the load and resistance models together in a wind performance model and evaluating the sensitivity of failure wind speed to both structural and aerodynamic factors for roof sheathing connections, roof-to-wall connections, and a complete load path.

### 4.1. Variance-Based Sensitivity Analysis

In a variance-based method, the importance of a parameter is measured as a ratio of variance, ordinarily called a sensitivity index. For a model that returns output $y$ as a function of input parameters $\{x_1, x_2, \ldots, x_k\}$, Saltelli *et al.* (2008) define the first-order sensitivity index for input $x_i$ as:

$$S_i = \frac{V[E(y|x_i)]}{V(y)} \tag{4.1}$$

In this definition, $V[E(y|x_i)]$ is the conditional variance of $y$ with respect to $x_i$. The argument $E(y|x_i)$ is the expectation of $y$ conditioned on $x_i$, which is the mean value of $y$ if $x_i$ is kept constant while the other input parameters vary. The conditional variance captures how the expectation changes across all possible values of $x_i$. Saltelli *et al.* demonstrate that computing the conditional variance is tantamount to generating a scatter plot of $y(x_i)$ for $n$ random samples, segregating the scatter points into thin vertical bins over the range of $x_i$, computing the mean model output $\bar{y}$ within each bin, and taking the variance of all $\bar{y}$. Graphically, the conditional variance measures non-uniformity in the scatter-point average as a gauge of the influence of $x_i$ on $y$. Dividing the conditional variance by the unconditioned variance $V(y)$ yields the first-order index $S_i$, which represents the average proportion of model uncertainty that would be removed if $x_i$ were constant. A comparatively high value of $S_i$ definitively identifies $x_i$ as an important parameter.

The sensitivity analyses presented in this chapter apply the random balance design method of Tarantola *et al.* (2006) to compute sensitivity indexes. [3] The method relies on Fourier spectra computed on $n$ model evaluations, where the input factors are sampled from a parametric curve $G_i(\sin \omega s_i)$. Here $G_i$ is selected based on the intended probability distribution of input $x_i$, and the parametric variable $s_i$ is a random permutation of $n$ points sampled on the domain $[-\pi, \pi]$. The frequency $\omega$ can be any positive integer $\leq (n-1)/2m$, where the number of harmonics $m$ is commonly set to six. In this analysis, input factors are sampled according to:

$$x_i(s_i) = F_i^{-1}\left[\frac{1}{2} + \frac{\sin^{-1}(\sin \omega s_i)}{\pi}\right] \tag{4.2}$$

where $\omega$ is set to 1 and $F_i^{-1}$ represents the inverse cumulative distribution function of $x_i$. The argument to $F_i^{-1}$ maps $s_i$ to the unit domain $[0, 1]$. Each input $x_1, x_2, \ldots, x_k$ is sampled for a unique random permutation, and the model is evaluated on the $n$ by $k$ sample set to compute output vector $y$. The first-order index for input $x_i$ is then derived from the discrete Fourier transform of $y_i^r$ for the first six harmonics, where $y_i^r$ is formed by sorting $y$ according to the ascending order of parametric variable $s_i$.

Saltelli *et al.* note that the value of $S_i$ is always between 0 and 1, and that the sum of $S_i$ for all input parameters is at most 1. The first-order index by definition does not capture the effects of interaction between parameters, which would appear for example in a model composed of terms involving products of input parameters. [4] In the absence of interaction effects, $S_i$ sum exactly to 1, and the sum of $S_i$ decreases as interactions become more consequential to model variability. In cases where $S_i$ sum

[3] Saltelli *et al.* provide a summary of this method and sample code on pp. 167–169.

[4] Refer to Saltelli *et al.*, pp. 25ff, for an example of such a model.

to a value substantially less than 1, higher-order indexes can be computed by other methods to determine the sensitivity behavior conclusively. If the sum is sufficiently large, however, indexes that include higher-order terms do not overturn the importance rankings established on the basis of first-order effects, especially where $S_i$ clearly mark out one or two parameters as most influential. For this reason, the results in the following sections are presented primarily in terms of $S_i$ determined using the random balance design method described above. Of the thirty cases analyzed, $\sum S_i > 0.75$ in all but four. For these four cases, where $\sum S_i > 0.58$, total-effect indexes $S_{T_i}$ have also been computed by means of a Monte Carlo procedure described in Saltelli *et al.* to verify the sensitivity behavior indicated by $S_i$. [5] The total-effect index includes the first-order effect of $x_i$ and all higher-order terms and is defined by Saltelli *et al.* as:

$$S_{T_i} = 1 - \frac{V[E(y|\mathbf{x}_{\neg i})]}{V(y)} \tag{4.3}$$

where $\mathbf{x}_{\neg i}$ is the set of all input parameters except $x_i$. The sum of $S_{T_i}$ is exactly 1 in the absence of parameter interactions and rises with increasing interaction.

### 4.2. Analysis of Structural Factors

The sensitivity analysis method is applied first to uplift resistance. The analysis independently considers roof sheathing and roof-to-wall connections to examine the importance of the associated structural factors. The section concludes with a system-level analysis to demonstrate how the relative importance of the various connections

[5] Saltelli *et al.* describe this procedure on pp. 164–167, and the reader is referred here for the details of implementation. The method of Tarantola *et al.* has been favored in this study for its time efficiency, since each analysis requires only $n$ model evaluations rather than $n$ by $k$ evaluations as in the method of Saltelli.

**Table 4.1.** Roof Sheathing Parameters: Normal Distributions

| Parameter | Units | $\mu$ | $\sigma/\mu$ | Truncation |
|---|---|---|---|---|
| Overdriving Factor | | 0.90 | 0.10 | [0.75 1.00] |
| Roof Cover Weight | kPa | 0.10 | 0.05 | |
| Roof Framing Specific Gravity | | 0.42, 0.50, 0.55 | 0.12 | |
| Sheathing Specific Gravity | | 0.42, 0.50 | 0.10 | |

in a load path can be determined.

### 4.2.1. Roof Sheathing Resistance

Uplift resistance of roof sheathing is evaluated as a function of nine structural factors. Fastener field spacing is sampled from an unweighted multinomial distribution with outcomes 15, 20, and 30 cm. Fastener size encompasses diameter and length and is evenly weighted between $2.87 \times 50.8$ mm and $3.33 \times 63.5$ mm; corresponding head diameters are 6.76 and 7.14 mm. Fastener type is selected as *smooth* or *annular* with equal probability. Roof member spacing is selected from 0.30, 0.41, 0.49, and 0.61 m, where 0.41 and 0.61 m are four times as likely as the other two spacings. Sheathing thickness is uniformly sampled from 11.1, 12.7, 14.3, and 15.9 mm. The remaining parameters, summarized in Table 4.1, follow either normal distributions or mixtures of normal distributions. Roof framing specific gravity is sampled from a mixture representing three common wood species, where the species are evenly weighted; the distribution assigned to sheathing specific gravity represents plywood and oriented strand board in equal proportions. Connection capacity is evaluated according to Section 2.1 as the lesser of nail withdrawal and nail head pull-through. The dead load is the combined weight of the sheathing panel and roof cover, where panel weight is computed from the sheathing density and thickness. Resistance is the sum of capacity and dead load.

The results of the sensitivity analysis are reported in Figure 4.1 for three cases.

The baseline uncertainty case assumes the parameter distributions defined above. On these assumptions, fastener field spacing and roof member spacing together constitute about 63% of the uncertainty in uplift resistance. [6] The densities of framing and sheathing make up another 22% of the uncertainty, and the other five factors together contribute the remaining 15%. From this epistemic starting point, the clear first step to reduce uncertainty would be to determine the true fastener field spacing and roof member spacing, which on average would remove more than half the variance from the resistance distribution. On the other hand, the results assign low importance to factors like fastener overdriving, roof cover weight, and sheathing panel thickness. Even though annular nails are substantially stronger in withdrawal than smooth nails, only about 6% of model uncertainty is associated with fastener type in this case.

How does the sensitivity behavior change as epistemic uncertainty is reduced? The results in the center column of Figure 4.1 presuppose a 0.41 m roof member spacing and a typical fastener field spacing of 30 cm, with a 5% probability of a 46 cm spacing. [7] The roof framing and sheathing densities are based on unmixed specific gravity distributions centered on 0.50 and 0.42 respectively. The sheathing thickness is constrained to 12.7 mm, and fasteners are assumed to be smooth nails measuring $2.87 \times 50.8$ mm. The right-hand column depicts the same case except that fasteners are assumed to be annular. The histograms in Figure 4.1 demonstrate the effect these presuppositions have on model uncertainty. If the sheathing nails are known to be smooth, roof framing density becomes the most important of the remaining variables,

[6] Throughout this chapter, the percentage of model uncertainty contributed by parameter $x_i$ is computed as $S_i / \sum S_i$. Reported percentages are approximate since they do not take higher-order effects into account. The estimate becomes more precise as $\sum S_i$ approaches 1.

[7] A missing field nail would increase the geometric tributary area of the critical fastener by 50%. See p. 20.

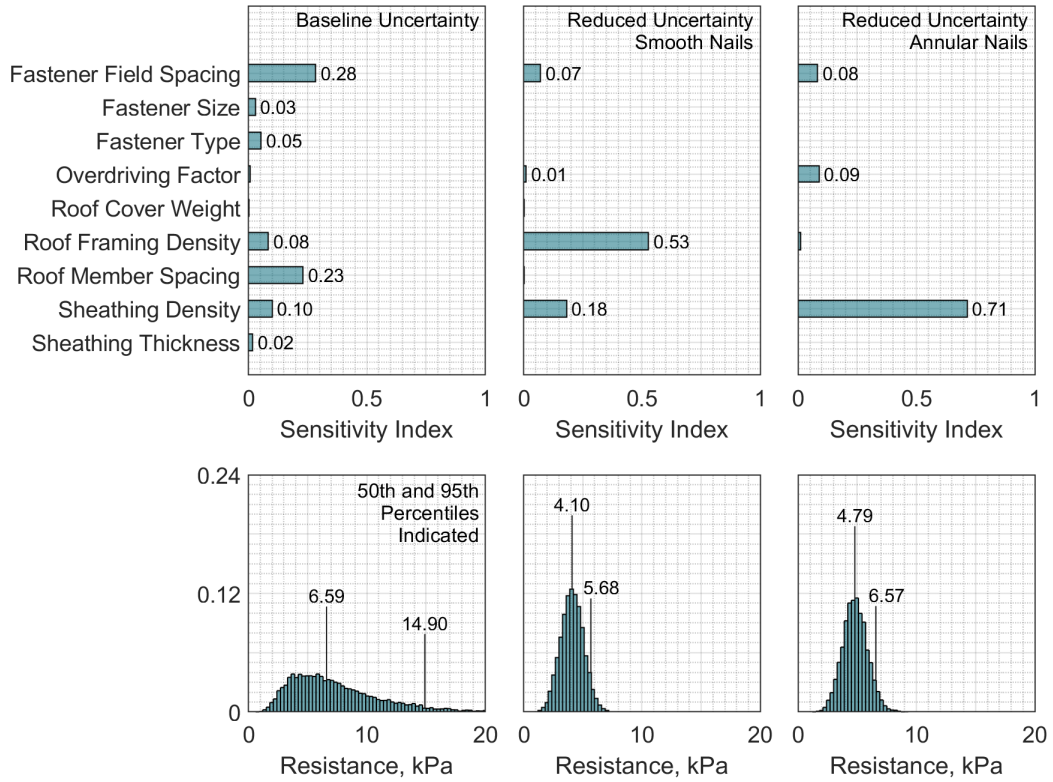


**Figure 4.1.** Sensitivity analysis of roof sheathing resistance for a case of broad uncertainty and two cases of reduced uncertainty. Results are based on 10,000 random samples. (Index values less than 0.01 are not labeled.)

responsible for about 66% of the uncertainty in resistance even after the wood species has been determined. If the nails are annular, sheathing density contributes 79% of the reduced uncertainty, and the influence of roof framing density vanishes. The reason is that smooth nails, in general, are limited by withdrawal capacity, while annular nails are limited by pull-through capacity. The relative importance of framing and sheathing densities corresponds to the relative frequency of withdrawal and pull-through failure. In the context of a post-event field study, *in situ* density testing would be the only way to reduce uncertainty further in either case, and fastener type would dictate whether framing or sheathing density data would be more useful.

**Table 4.2.** Roof-to-Wall Parameters: Normal Distributions

| Parameter | Units | $\mu$ | $\sigma/\mu$ |
|---|---|---|---|
| Roof Components Weight | kPa | 0.17 | 0.10 |
| Roof Framing Specific Gravity | | 0.42, 0.50, 0.55 | 0.12 |
| Tie Dowel Bearing Strength | GPa | 0.43 | 0.05 |
| Tie Tensile Strength | GPa | 0.31 | 0.05 |
| Wall Framing Specific Gravity | | 0.42, 0.50, 0.55 | 0.12 |

### 4.2.2. Roof-to-Wall Connection Resistance

The roof-to-wall resistance evaluation involves the eleven structural parameters listed in Figure 4.2. Roof member spacing follows the same distribution as in the roof sheathing analysis. For the dead load calculation, roof slope is uniformly sampled from nine discrete values between 4.8° and 45°, and roof member span is sampled from a continuous uniform distribution bounded at 6.10 and 11.58 m. A hurricane tie is installed in 50% of outcomes. The number of toe-nails in the connection is either two or three, with the three-fastener option assigned a 90% probability. Toe-nail size is set to $3.76 \times 76.2$ mm or $3.43 \times 88.9$ mm in equal proportions. The other parameters follow normal distributions or mixtures thereof according to Table 4.2. Resistance of the roof-to-wall connection is evaluated by the following steps:

1. Compute the withdrawal capacity of the toe-nailed connection as in Section 2.1, multiplying the result of Eq. (2.1) by the number of toe-nails and a deterministic factor of 0.67. The specific gravity in Eq. (2.1) is that of the wall framing.

2. If a hurricane tie is installed, compute the lateral capacity as in Section 2.1. The evaluation assumes shear is resisted by five fasteners measuring $3.33 \times 63.5$ mm. The specific gravity is taken as the lesser of roof framing and wall framing. The lateral capacity is checked against the ultimate tensile capacity of the tie computed on an approximate net section of 49 mm$^2$.

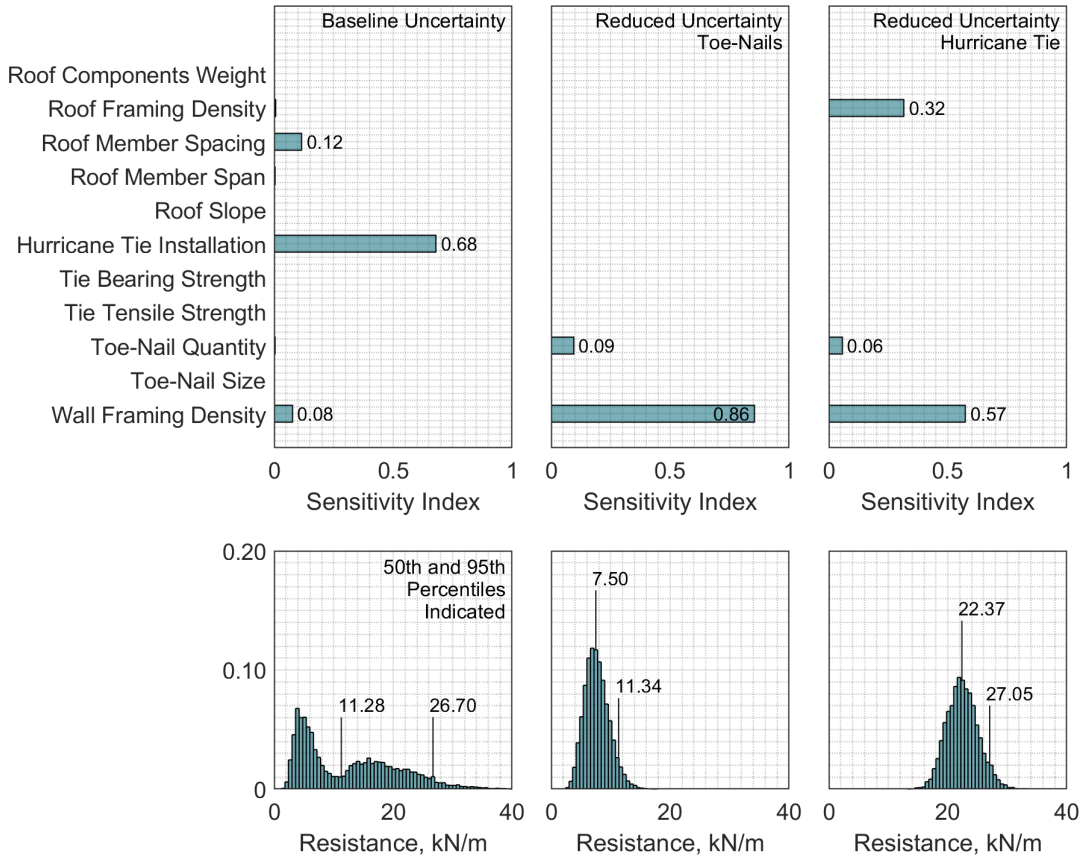


**Figure 4.2.** Sensitivity analysis of roof-to-wall connection resistance for a case of broad uncertainty and two cases of reduced uncertainty. Results are based on 10,000 random samples.

3. Compute the roof framing weight as a function of roof slope and roof member span, assuming rafter-and-joist framing with nominal $2 \times 6$ members. The dead load is the combined weight of the roof framing and roof components that are tributary to the roof-to-wall connection.

4. Resistance is obtained as the sum of the toe-nail and hurricane tie capacities and the dead load, divided by the roof member spacing — the result is an equivalent linear resistance along the wall.

As with roof sheathing, the roof-to-wall analysis considers a baseline uncertainty case, defined by the parameter distributions specified above, and two cases of reduced

uncertainty. In the baseline case, the presence or absence of a hurricane tie accounts for 75% of the model uncertainty. The remaining uncertainty is explained by roof member spacing and wall framing density. The strong influence of hurricane tie installation is visible in the resistance histogram at lower-left in Figure 4.2, where the two distinct modes in the distribution clearly correspond to the relatively weak toe-nailed connection and the far stronger tie-reinforced connection. These two modes are separately depicted in the center and right-hand cases in Figure 4.2. Uncertainty in these cases is further reduced by presupposing a 0.41 m roof member spacing, a 7.9 m roof member span, an 18.4° roof slope, and 3.43 × 88.9 mm toe-nails. The specific gravities of roof and wall framing are also sampled from unmixed normal distributions centered on 0.42 and 0.55 respectively. For connections composed only of toe-nails, about 90% of the outstanding uncertainty is found in the wall framing density. For connections with both toe-nails and a hurricane tie, roof and wall density together explain 93% of the uncertainty, with greater importance attached to wall framing density since it is the core factor in toe-nail capacity and limits hurricane tie capacity whenever it is less than the roof framing density.

### 4.2.3. System Resistance

The preceding analyses examined the sensitivity behavior of single connections. The load path resistance modeling approach proposed in Chapter 2 can be applied to generalize the sensitivity analysis to a system of connections. Once the load path is formulated as a series system, the analysis may be predicated on the minimum series resistance for $n$ load path realizations. Sensitivity indexes can then be computed for the applicable structural parameters as in the roof sheathing and roof-to-wall analyses, an approach that would be especially useful for tracing the influence of factors that affect resistance in multiple connections. As a more compact alternative, indexes may

instead be computed by generating connection-level resistance distributions *a priori* and sampling connection resistance directly, rather than sampling from the underlying structural factors. The resulting indexes indicate the proportion of uncertainty each connection contributes to system-level resistance.

The cases in Figure 4.3 demonstrate this compact approach for a single-story home with a slab-on-grade foundation. [8] The first row reports $S_i$ computed on connection resistances; subsequent rows present the connection resistance distributions, the probability of system failure initiating in each connection, and the system-level resistance distribution in each case. The left-hand column depicts a reference case with relatively wide uncertainty in several connections. Specifically, the roof-to-wall connection may be composed of toe-nails alone or of toe-nails accompanied by an H2.5A tie or an H8 tie, with all three options evenly weighted. The face-nail connection between the top plates is strengthened by overlapping wall sheathing in 50% of outcomes and is also strengthened by the H8 tie whenever it is installed. The wall-to-slab connection is subject to uncertainty both in anchor spacing and in washer diameter. The characteristic weak outcomes in these connections make them the three most likely failure points in the load path, responsible for system failure in a combined 83% of realizations. The sensitivity behavior indicated by $S_i$ resembles the failure probabilities, but the proportions are not the same — the clearest difference is that the wall-to-slab connection, though its 43% failure rate makes it, on average, the weakest connection in the load path, is identified only as the second-most influential connection in the sensitivity analysis. [9] The two measures serve related but distinct purposes.

[8] Connection resistances in Figure 4.3 are evaluated as described in Section 2.1.

[9] Since $\sum S_i < 0.75$ for this case, the total-effect indexes have been computed as well to verify that higher-order effects do not change the relative rankings: $S_{T_i}$ are found to be 0.47 for the double top plate connection, 0.40 for wall-to-slab, 0.29 for roof-to-wall, 0.13 for roof sheathing, and $< 0.03$

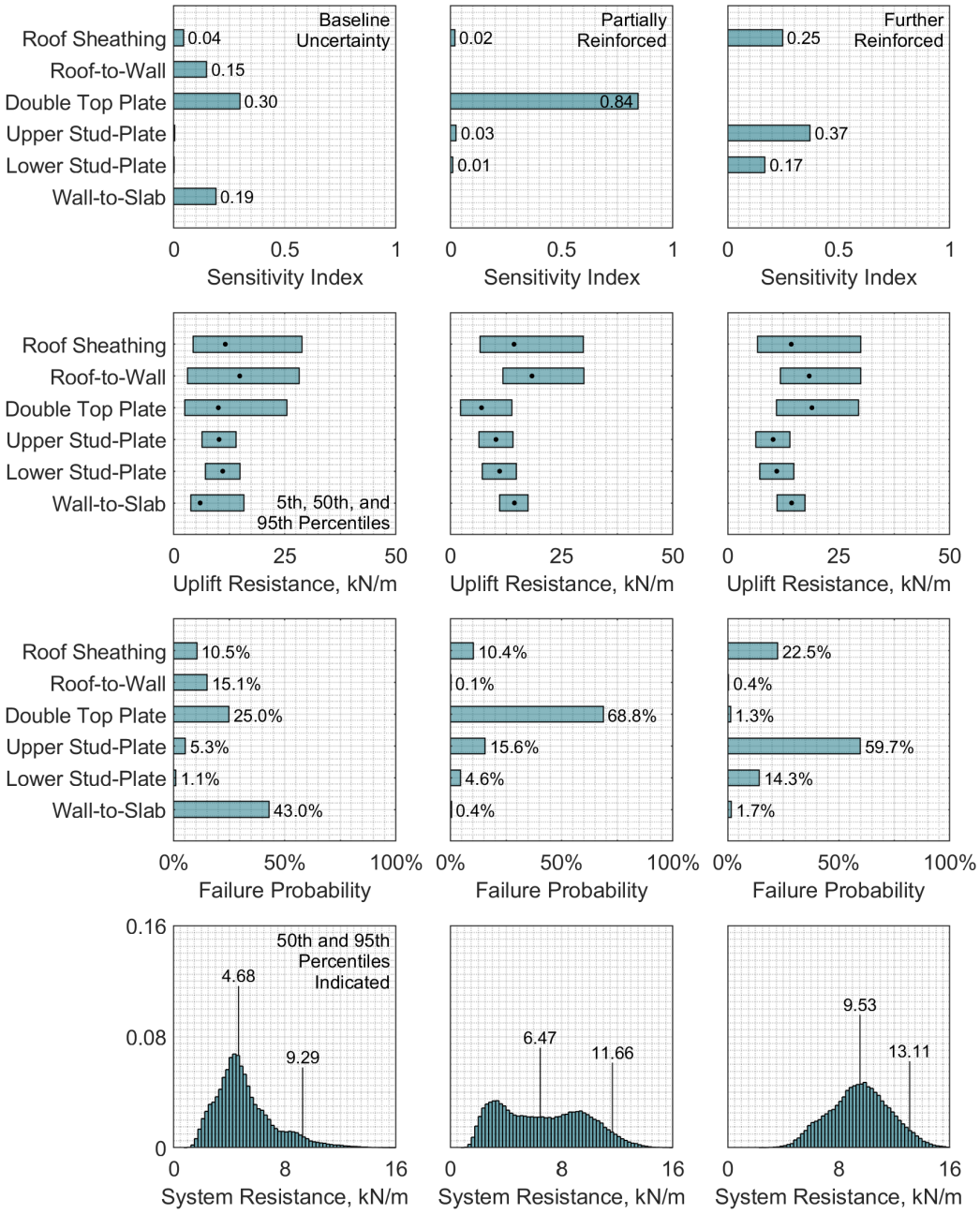


**Figure 4.3.** Sensitivity analysis of system resistance in the load path of a single-story home with a slab-on-grade foundation, considering various levels of load path reinforcement. Results are based on 50,000 random samples.

for the stud-plate connections.

System-level failure probabilities tell the analyst how best to improve mean system resistance; sensitivity indexes tell the analyst how best to reduce the uncertainty in system resistance.

The center column in Figure 4.3 represents a partially reinforced load path with respect to the baseline case. The roof sheathing connection has been constrained to stronger fastener options, though uncertainty in the roof member spacing is retained. The wall-to-slab connection is limited to large anchor bolt washers 7.6 cm in diameter. Most consequentially, the roof-to-wall connection now always consists of an H2.5A hurricane tie. The result of these constraints is an acute weakness in the double top plate connection, since the option of reinforcement by an H8 tie has been removed. The sensitivity behavior and the failure probabilities clearly signal this weakness, with $S_i$ indicating that the double top plate by itself contributes about 93% of the uncertainty in system resistance in this case. If the roof-to-wall connection instead features an H8 tie in all outcomes, as in the right-hand column of Figure 4.3, the double top plate weakness is relieved, and system resistance realizes a 43% increase in the mean and a 50% reduction in variance. [10]

### 4.3. Analysis of Aerodynamic Factors

The preceding section investigated the importance of various structural factors to uplift resistance; this section presents a complementary analysis of the factors that determine uplift pressure intensity. The aerodynamic factors of interest here are roof eave height, roof shape, roof slope, depth of roof overhangs, length and breadth of the roof plan, and wind direction. Uplift pressure intensity is measured in terms of

[10] The reduction in variance is computed as $(\sigma^2 - \sigma_0^2)/\sigma_0^2$, where $\sigma$ and $\sigma_0$ are the standard deviations of the 'fully reinforced' and 'partially reinforced' resistance distributions.

$\bar{C}_p$, defined in Chapter 3 as the most negative spatial average of time-averaged $C_p$ at any location on the roof plan. [11] As in the previous chapter, the area of the spatial average depends on whether roof structure loads or roof component loads are in view. A variance-based sensitivity analysis of uplift intensity requires a model that evaluates $\bar{C}_p$ as a continuous function of the aerodynamic factors of interest. The pressure prediction method described in Chapter 3 was developed for exactly this purpose and serves as the analysis model here.

Before turning to the formal sensitivity analysis, it may be helpful first to examine the variation of $\bar{C}_p$ over a subset of the parameter space to form some initial impressions of the sensitivity behavior. The profiles in Figure 4.4 depict $\bar{C}_p$, averaged at the scale of roof structure loads, as a function of wind direction for gable and hip roof shapes at nine common roof slopes. Here the model results assume a rectangular-plan building 12.2 m in length by 6.1 m in breadth with a mean roof height of 4.3 m, and the spatial averaging window for $\bar{C}_p$ measures 0.61 m along the exterior wall and spans from eave to ridgeline, representing the typical tributary area of a roof-to-wall connection. For each case, the corresponding design $C_p$ obtained from Chapter 27 of ASCE 7-22 are also indicated at 0° and 90° for winds parallel to and normal to ridge respectively. [12] Model predictions have been multiplied by a factor of 1.06/1.52 to re-reference $\bar{C}_p$ from a ten-minute average wind speed to a three-second gust as in ASCE 7. The comparison suggests close agreement between predicted $\bar{C}_p$ for gable roofs and the corresponding design values along the principal wind directions, but the model elucidates what cannot be seen at a glance in the Chapter 27 design provisions, namely $(a)$ the effect

[11] See p. 70.

[12] Design $C_p$ are found by interpolation in Fig. 27.3-1 as a function of roof slope and aspect ratio. For roof slopes $> 10°$, the plotted value represents the lesser of the windward and leeward-side uplift $C_p$. For winds parallel to ridge and for roof slopes $< 10°$, the worst-case uplift $C_p$ is used.

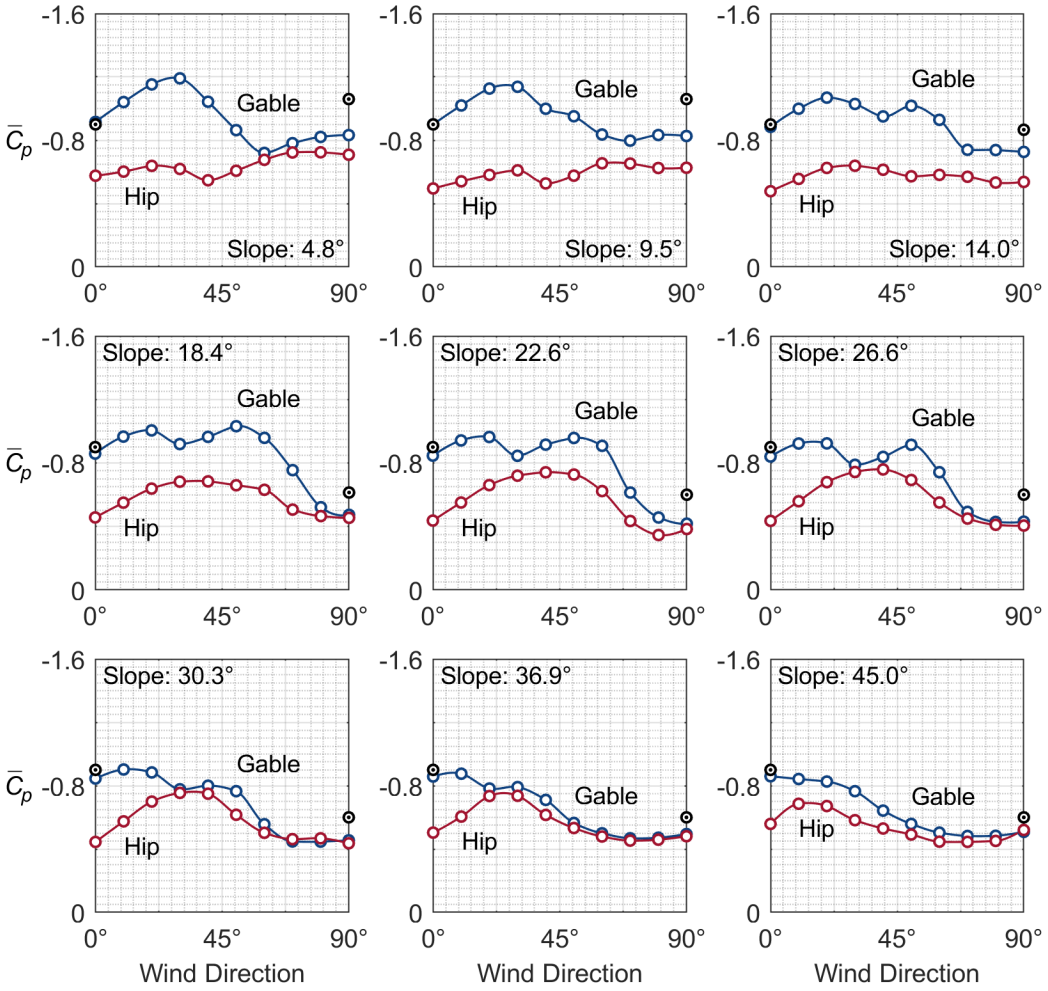


**Figure 4.4.** $\bar{C}_p(\theta)$ averaged at roof structure scale. Design $GC_p$ from Chapter 27 of ASCE 7-22 are indicated by markers at 0° and 90°.

of roof shape, clearly reflecting the more favorable aerodynamics of hip roofs, and $(b)$ the uplift intensities produced by wind directions other than 0° and 90° relative to ridge. The same cases are evaluated at the scale of roof sheathing in Figure 4.5, where $\bar{C}_p$ are based on a 1.22 m by 2.44 m averaging area representative of a standard roof sheathing panel. A comparison to ASCE 7 is not made here, since the design $GC_p$ supplied in Chapter 30 for roof components are the product of a peak estimation

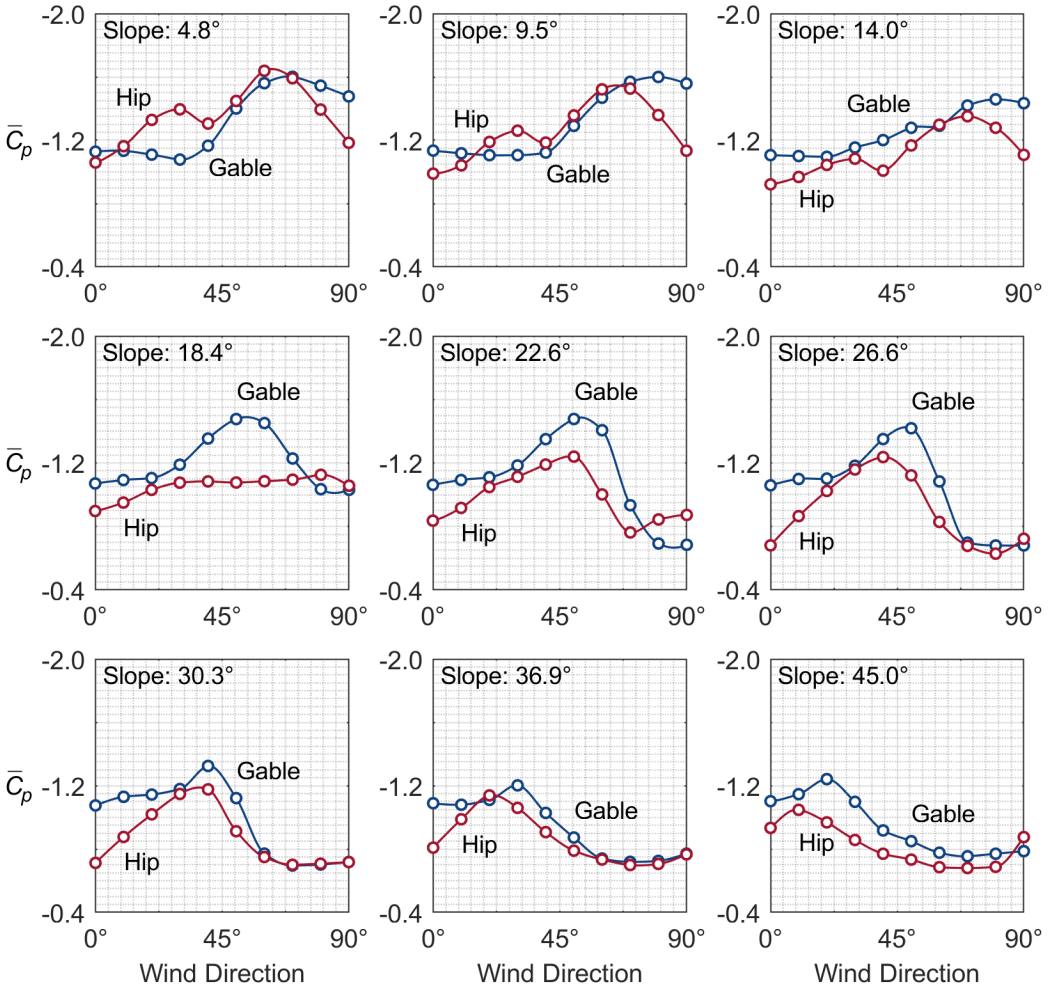


**Figure 4.5.** $\bar{C}_p(\theta)$ averaged at roof sheathing scale.

procedure that has not been replicated in this work. [13] For this reason, $\bar{C}_p$ have not been re-referenced to a three-second gust wind speed as in Figure 4.4.

Taken together, both sets of results warrant an expectation that roof shape, roof slope, and wind direction will be found influential in the global analysis. Further, it seems that the relative importance of roof shape and roof slope is dependent on wind direction, since $\bar{C}_p$ appears more sensitive to roof shape for winds parallel to ridge

[13] But refer to Figure 3.9 on p. 74 for an indirect comparison between model predictions and design $GC_p$ for an array of roof sheathing panels.

and more sensitive to roof slope if normal to ridge. These expectations agree with intuition. As an average across all wind directions, we might also anticipate that roof shape will prove more important than roof slope in the case of roof structure loads and that the reverse will be true for roof sheathing, with wind direction contributing a commensurate level of uncertainty at both scales. The following analysis formally tests these suspicions along two lines: what is the sensitivity behavior of $\bar{C}_p$ (1) if conditioned on a specific wind direction and (2) if wind direction is unconstrained?

### 4.3.1. Analysis Conditioned on Wind Direction

Roof height and roof plan measurements were assumed constant in the model results presented above. To measure their importance, these factors are here sampled from continuous uniform distributions, where roof eave height is bounded between 2.44 and 6.10 m, plan breadth between 6.10 and 11.58 m, and plan length between 12.19 and 24.38 m. Roof shape and roof slope follow multinomial distributions. Roof shape is evenly weighted between gable and hip; roof slope is sampled from $\tan^{-1}(r/12)$, where $r$ takes an integer value from 1 to 12 with all outcomes equally likely. In cases that consider roof overhang effects, the overhang depth also follows a multinomial distribution with evenly weighted outcomes 0.30, 0.41, 0.51, and 0.61 m; overhang depth is zero otherwise.

The analysis is carried out for ($a$) roof structure loads, ($b$) roof structure loads with overhang effects, ($c$) and roof sheathing loads. The left-hand column of Figure 4.6 reports the sensitivity indexes $S_i$ computed for these three cases conditioned on winds parallel to ridge. The results verify the expectation stated earlier that $\bar{C}_p$ for winds parallel to ridge is controlled by roof shape, which is found to be responsible for more than 60% of model uncertainty for roof sheathing and for nearly all uncertainty at roof structure scale, irrespective of overhangs. In the center column, the analysis finds that

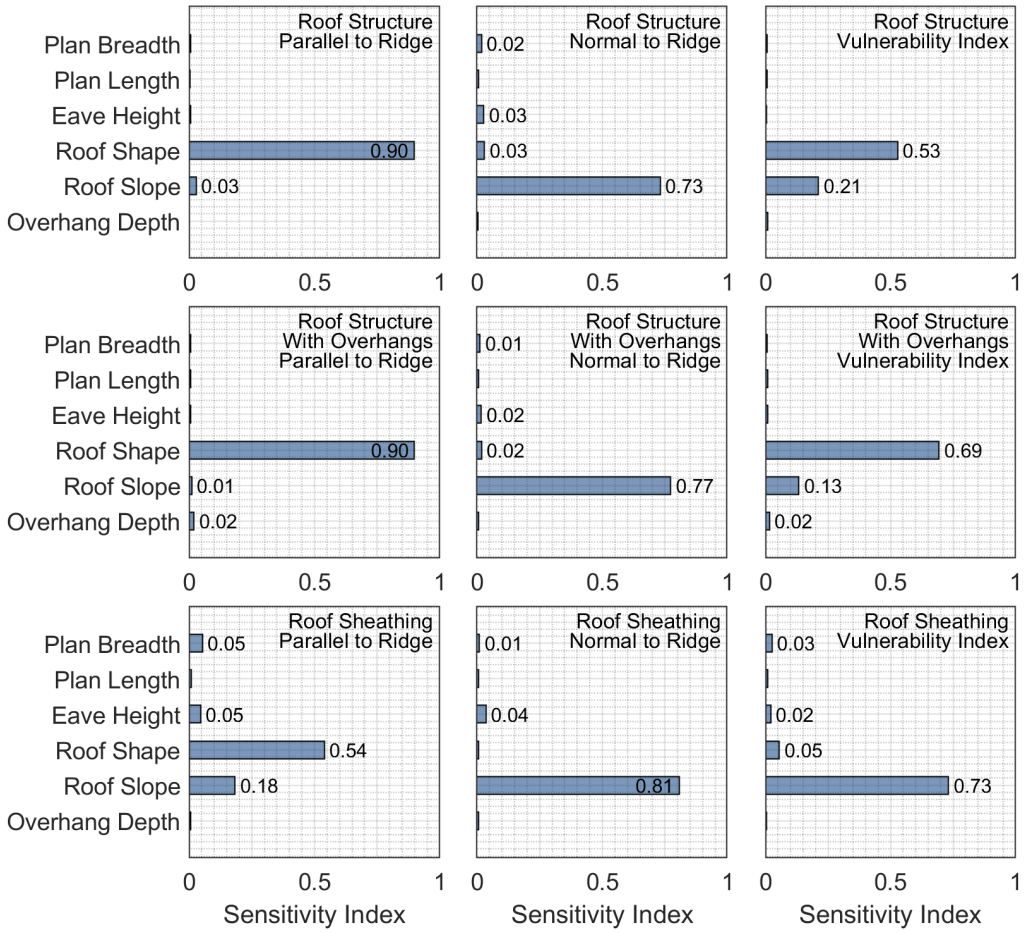


**Figure 4.6.** Sensitivity analysis of $\bar{C}_p$ conditioned on specific wind directions. Results are based on 2,000 random samples.

roof slope controls to a similar degree for winds normal to ridge, attributing about 90% of model uncertainty to roof slope in all cases. This is also as expected, since the aerodynamic advantage of hip roofs over gable roofs largely vanishes at this wind direction, and roof slope determines whether uplift is controlled by flow separation at the windward eave or at the ridgeline. The results in the right-hand column of Figure 4.6 are conditioned on wind direction in a different way; the sensitivity analysis is predicated on the aerodynamic vulnerability index, defined in Section 3.3.2 as the product of the 50th and 90th percentile values of the $\bar{C}_p(\theta)$ distribution for all wind directions $\theta$. In this calculation $\bar{C}_p$ is evaluated from 0° to 90° in 22.5° steps for each of

the $n$ geometry realizations, and the percentiles are taken from a smooth interpolation in $\theta$ to determine the vulnerability index for each realization. This procedure effectively conditions the analysis on a median-severity and high-severity wind direction at the same time and draws out the aggregate influence of the aerodynamic factors without explicitly defining wind direction as a parameter. The results support what appeared to be true in Figures 4.4 and 4.5 — in terms of overall vulnerability, roof shape has primary influence at structure scale, and roof slope has primary influence at sheathing scale. Moreover, though the sensitivity index registers low for overhang depth, the presence of roof overhangs heightens the importance of roof shape. The reason is that overhangs have a meaningful effect on $\bar{C}_p$ only for gable roofs, so that the additional uncertainty brought into the model by including overhang effects is always associated with the gable roof shape and is thus removable from the model by constraining the roof shape to hip. [14] Lastly, regardless of how the analysis is conditioned, the results find that eave height and roof plan dimensions have at most marginal significance to $\bar{C}_p$. Eave height and plan breadth both appear to have slightly more importance at sheathing scale than at structure scale, but each never contributes more than about 6% to the total uncertainty.

### 4.3.2. Unconditioned Analysis

Conditioning the sensitivity analysis on the aerodynamic vulnerability index is one method of arriving at a direction-independent influence pattern behind $\bar{C}_p$. Another method is to regard wind direction as a random variable alongside the geometry factors. The results presented in Figure 4.7 take this approach. The columns, from left

[14] The correlation between overhang effects and the gable roof shape can be seen in Figure 3.13 on p. 81.

to right, correspond to roof structure loads, roof structure loads with overhang effects, and roof sheathing loads. The first row depicts the first-order sensitivity behavior expressed by $S_i$. Since $\sum S_i < 0.75$ in these analyses, the total-effect indexes $S_{T_i}$ are reported for the same cases in the second row. Histograms of $\bar{C}_p$ are plotted in the third row to convey a sense of model variability. The parameter distributions are the same as those assumed in the conditioned analysis above, joined now by wind direction which follows a continuous uniform distribution bounded between 0° and 90°. The results support the following inferences:

1. Eave height and roof plan measurements are decisively unimportant to $\bar{C}_p$ for both roof structure and roof sheathing loads. Low-valued $S_{T_i}$ rule out the possibility of substantial interaction effects with other factors. Fixing these parameters at any constant value in their distributions would have little effect on model uncertainty.

2. The relative importance of roof shape to roof slope in each case is largely the same as in the conditioned analysis, with the exception that the interaction effects revealed by $S_{T_i}$ raise the importance of slope relative to shape for roof structure loads, especially in the absence of overhang effects.

3. The presence of roof overhangs increases the significance of roof shape, for the same reason as in the conditioned analysis. The low value of $S_{T_i}$ found for overhang depth does not signal that the presence or absence of overhangs is unimportant, since the inclusion of overhangs has a clear effect on the distribution of $\bar{C}_p$. Rather it proves that uncertainty in the overhang depth over the assumed range 0.30 to 0.61 m contributes little uncertainty to the model as a whole. The implication is that the existence of roof overhangs is of some importance, but the precise depth of overhangs appears unimportant.

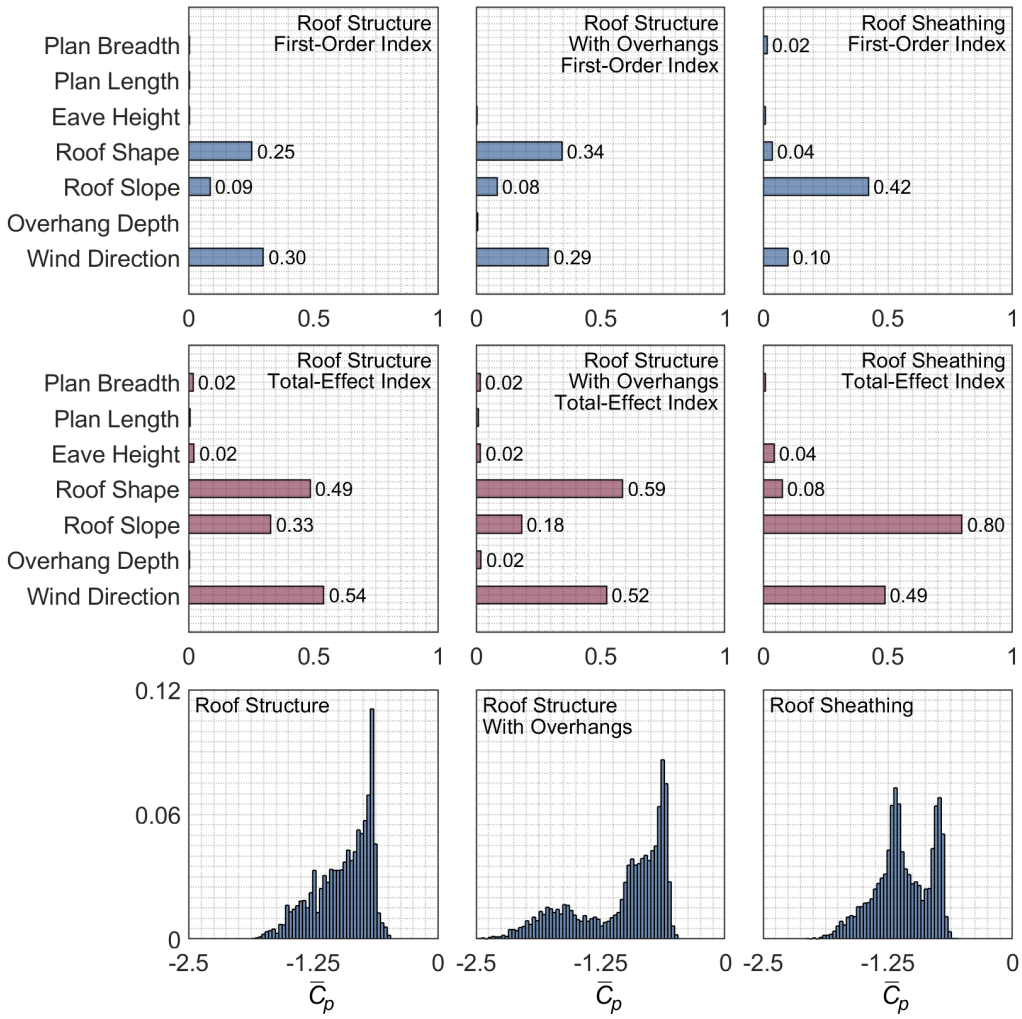


**Figure 4.7.** Sensitivity analysis of $\bar{C}_p$ unconditioned with respect to wind direction. $\bar{C}_p$ in all cases are referenced to a ten-minute average wind speed. Results are based on 4,000 random samples.

4. At roof structure scale, wind direction contributes about the same level of uncertainty to the model as roof shape, irrespective of overhangs. Roof slope is still of first importance at sheathing scale, but the $S_{T_i}$ distribution reveals that wind direction nonetheless contributes substantial uncertainty through interaction with roof slope.

**Table 4.3.** Probabilistic Wind Load Parameters

| Parameter | Distribution | $\mu$ | $\sigma$ |
|---|---|---|---|
| Exposure Coefficient $K_z$ | | 0.79 | 0.11 |
| Gust-Effect Factor $G$ | Normal | 0.83 | 0.08 |
| Internal Pressure Coefficient $GC_{p_i}$ | | 0.15 | 0.05 |

### 4.4. Analysis of Wind Performance

This chapter has so far examined uplift resistance as a function of structural factors and uplift load intensity as a function of aerodynamic factors, in order to discern the sensitivity behavior operating within resistance and load as separate models. In this stage of the analysis, the resistance and load models are brought together to examine how both structural and aerodynamic factors influence wind performance. The procedure involves first drawing $n$ samples of uplift resistance $R$ from the resistance model and $n$ samples of $\bar{C}_p$ from the load intensity model. Then for each pair of $R$ and $\bar{C}_p$ samples, the corresponding failure wind speed $V$ is computed from the following limit state function:

$$0.613K_zV^2(G\bar{C}_p - GC_{p_i}) + R \leq 0 \tag{4.4}$$

The first term is an ASCE 7 wind pressure model, where $V$ in m/s leads to wind pressure in Pa. The analysis assumes a deterministic value of 1 for the topographic, ground elevation, and directionality factors and models the exposure coefficient $K_z$, gust-effect factor $G$, and internal pressure coefficient $GC_{p_i}$ probabilistically according to Table 4.3, where the nominal ASCE 7 values have been adapted as in Ellingwood and Tekie (1999). The calculation of $V$ is illustrated in Figure 4.8 for a toe-nailed roof-to-wall connection. The left-hand histograms contain $n$ samples of resistance and

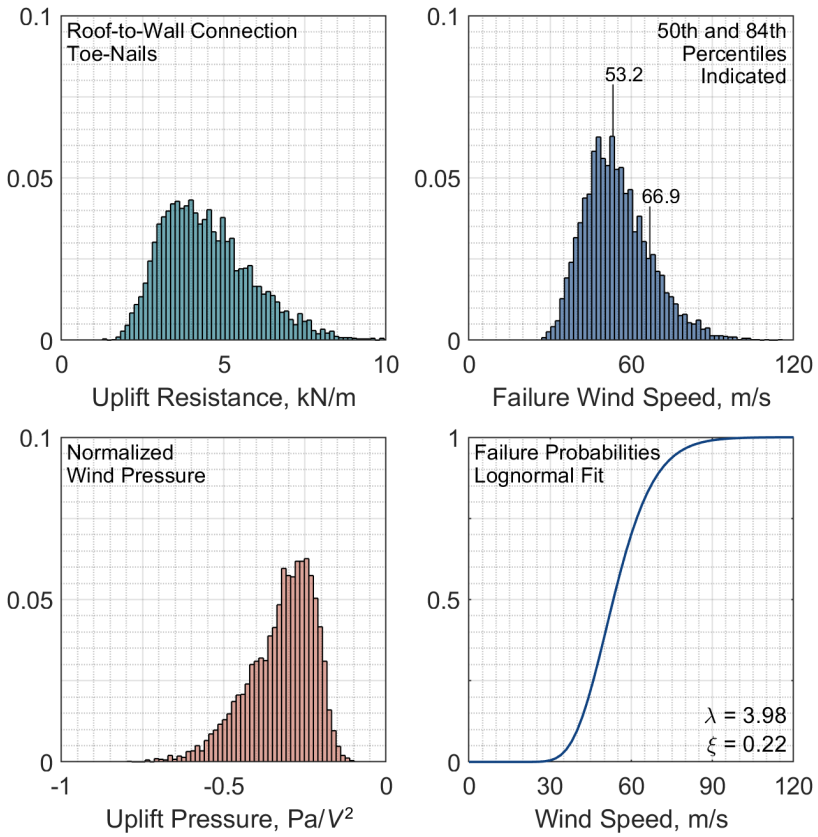


**Figure 4.8.** *Left:* Samples of uplift resistance and normalized wind uplift pressure for a toe-nailed roof-to-wall connection. *Right:* Failure wind speeds $V$ computed from Eq. (4.4) sample by sample. The fragility function is a lognormal fit of the normalized cumulative distribution of $V$, with logarithmic mean $\lambda = \ln V_{50}$ and standard deviation $\xi = \ln V_{84} - \ln V_{50}$, where $V_p$ is the $p$th percentile failure wind speed.

normalized wind pressure. [15] Solving for $V$ in the limit state function for each of the $n$ sample pairs yields the failure wind speed distribution at upper right. A fragility function can be constructed for the connection by fitting a curve to the normalized cumulative distribution of failure wind speeds, depicted in the graph at lower right. The sensitivity analysis is predicated on the distribution of $V$; the resulting indexes $S_i$ thus indicate how much variance each factor contributes to the fragility function. The

[15] Normalized wind pressure is equal to the first term in Eq. (4.4) divided by $V^2$.

same roof sheathing, roof-to-wall, and system resistance cases analyzed in Section 4.2 are now revisited from the perspective of wind performance.

### 4.4.1. Roof Sheathing Performance

The wind performance model for roof sheathing assumes the structural factor distributions specified in Section 4.2.1 and the same roof geometry and wind direction distributions used in Section 4.3. Failure wind speeds are computed according to the procedure described above, except that the gust-effect factor $G$ is replaced by a deterministic coefficient of 1.43, which combines a 0.95 bias factor with a factor of 1.50 to bring predicted $\bar{C}_p$ into closer alignment with design $GC_p$ for roof sheathing panels. [16] The analysis results are presented in Figure 4.9 for the three cases considered in Section 4.2.1. Parameters that influence uplift resistance appear in the upper part of the sensitivity graph, and those in the lower part of the graph determine the uplift load. Compared to Figure 4.1, where $S_i$ are predicated on sheathing resistance, the relative proportions of structural factor importance remain largely the same for all cases. The aerodynamic factors also take the same order of importance as in the right-hand column of Figure 4.7, though wind direction appears to have a greater share of influence on $V$ than was evident in the analysis predicated on $\bar{C}_p$.

In the baseline case, which is intended to represent maximal epistemic uncertainty within the bounds of typical construction practice, resistance factors account for about 80% of the fragility variance. As the true values of the structural parameters are determined, uncertainty is removed from the fragility function; in terms of the

[16] The comparison between predicted $\bar{C}_p$ and design $GC_p$ in Figure 3.9 on p. 74 guides the selection of this factor, which is intended to adjust the worst-case $\bar{C}_p$ for each panel to roughly the same level as the corresponding ASCE 7 design value. This adjustment factor primarily affects the median values of the fragility functions and has little effect on the sensitivity analysis results. The 0.95 bias factor is based on Ellingwood and Tekie (1999).

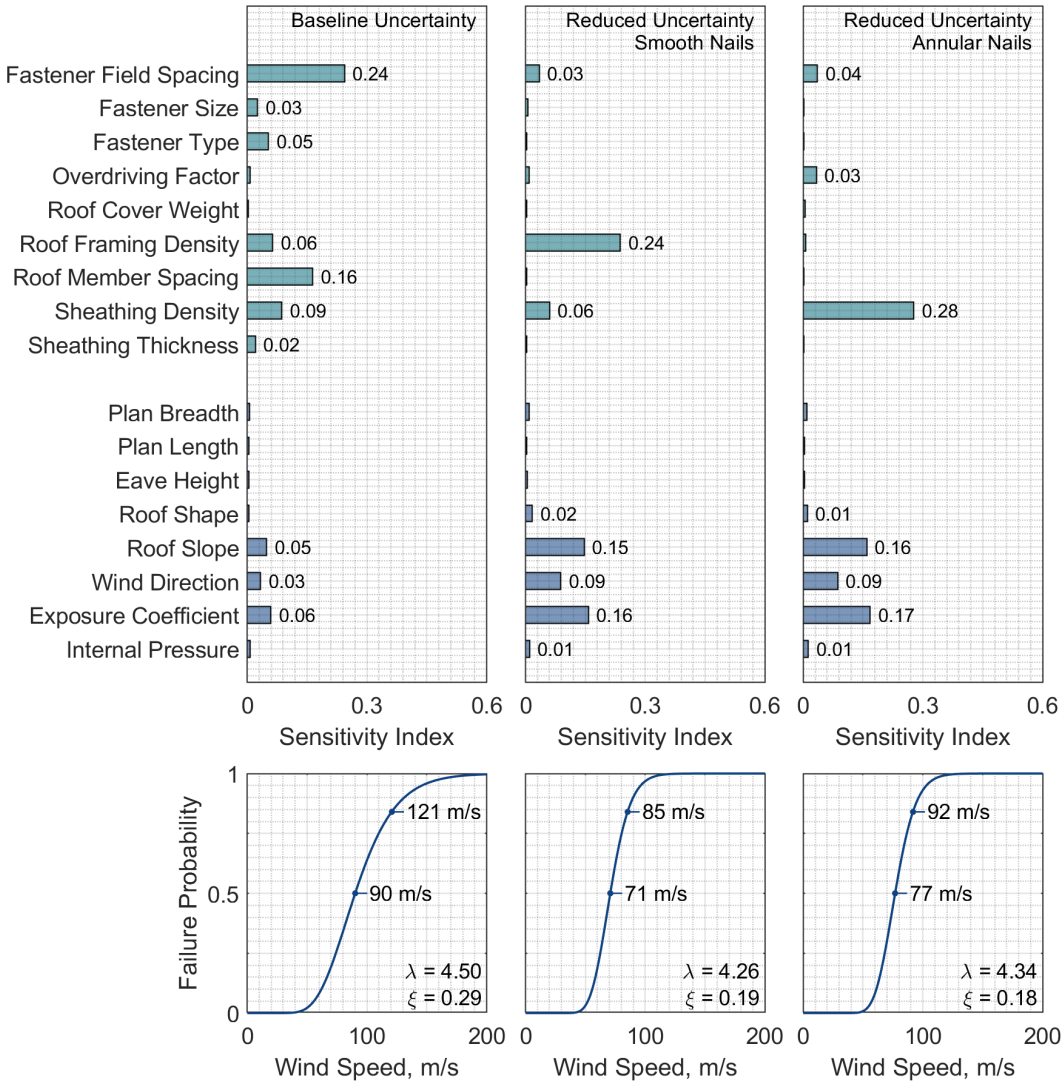


**Figure 4.9.** Sensitivity analysis of roof sheathing performance for a case of broad uncertainty and two cases of reduced uncertainty. Results are based on 4,000 random samples. Fragility function annotations indicate the 50th and 84th percentile failure wind speeds.

logarithmic standard deviation $\xi$, computed from the 50th and 84th percentile failure wind speeds as $\ln V_{84} - \ln V_{50}$, more than 30% of the uncertainty is removed by knowing the nail field spacing, size, and type, the wood species and spacing of roof framing members, and the sheathing panel type and thickness. With these structural data in hand, the balance of uncertainty shifts, and about 55% of the variance arises from load

factors. As the earlier analysis of aerodynamic factors suggested, roof slope appears to be the only geometry factor that exercises substantial influence on roof sheathing performance, though the sensitivity behavior may be different if other damage states are assumed — for example, damage states that involve the failure of more than one sheathing panel in an array of panels. For the failure of a single panel as modeled here, the results identify roof slope, wind direction, and exposure coefficient as the only important load factors.

### 4.4.2. Roof-to-Wall Connection Performance

The wind performance of roof-to-wall connections is evaluated for the same cases and structural parameters described in Section 4.2.2. The aerodynamic factor distributions are drawn from Section 4.3. [17] Failure wind speeds are computed from Eq. (4.4), where $\bar{C}_p$ sampled from the uplift intensity model have been re-referenced to a three-second gust wind speed. [18] The resistance term $R$ is formulated as:

$$R = R_0 \left( \frac{2 \cos \beta}{s_r l_r} \right) \tag{4.5}$$

which converts roof-to-wall resistance $R_0$ from a force to a force per area as a function of roof member spacing $s_r$, roof member span $l_r$, and roof slope $\beta$. The reciprocal of the term in parentheses is the geometric tributary area of a roof-to-wall connection. The results are reported in Figure 4.10. The resistance and load factors are grouped separately as in the roof sheathing analysis, but here the separation is not perfectly strict. Roof member span and roof slope influence resistance by means of Eq. (4.5) as

[17] Roof overhang depth is here sampled from 0, 0.30, 0.41, 0.51, and 0.61 m with equal probability.

[18] $\bar{C}_p$ are multiplied by 0.61, which includes a 1.06/1.52 conversion factor from the Durst curve and a 0.87 bias factor based on Ellingwood and Tekie.

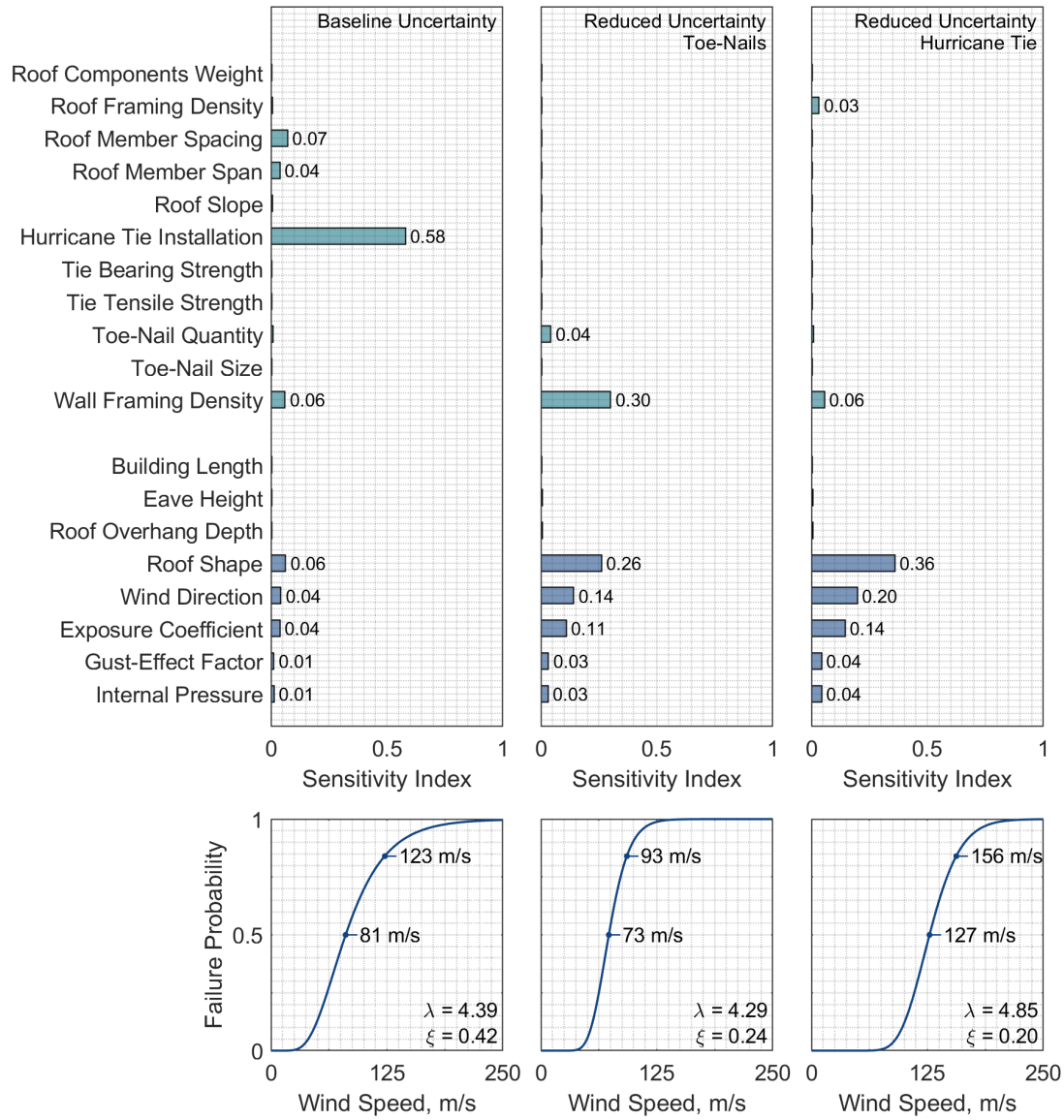


**Figure 4.10.** Sensitivity analysis of roof-to-wall connection performance for a case of broad uncertainty and two cases of reduced uncertainty. Results are based on 4,000 random samples. Fragility function annotations indicate the 50th and 84th percentile failure wind speeds.

well as through the dead load calculation, but they are also predictor variables in the $\bar{C}_p$ model, where roof member span is equivalent to plan breadth. The results indicate the following:

1. The structural factor sensitivity behavior generally retains the proportions seen

earlier in Figure 4.2, except that roof member span registers minor importance because of its role in Eq. (4.5).

2. In the baseline uncertainty case, the presence or absence of a hurricane tie far outweighs every other factor in importance, comprising 63% of the fragility variance by itself.

3. For roof-to-wall connections composed of toe-nails alone, wall framing density appears to be at least as important as roof shape, even once the uncertainty associated with roof member span and spacing, roof slope, toe-nail size, and wood species are removed, in which case the load factors collectively control about 60% of the fragility variance.

4. On the other hand, if the same structural factors listed in the previous point are known *and* a hurricane tie is installed, load factors instead control about 86% of the variance, with the remaining 14% bound up in wood density.

5. Roof shape leads the aerodynamic factors in importance, followed by wind direction, which appears to exercise less influence on the failure wind speed than on $\bar{C}_p$. (See Figure 4.7.) Roof slope is of little consequence in the baseline uncertainty case, but the Figure 4.7 results suggest that it would have some modest influence in the reduced uncertainty cases had it not been set to a constant.

6. As in Figure 4.7, roof overhang depth is of minimal importance, but the presence of overhangs of any depth likely raises the importance of roof shape for the reason stated in Section 4.3.1.

### 4.4.3. System Performance

Lastly, the system of connections considered in Section 4.2.3 is analyzed with respect to wind performance. The analysis assumes the same load parameters as in the baseline roof-to-wall connection case above and adopts the connection resistance distributions of Section 4.2.3 with one difference: roof sheathing resistance is not multiplied by the along-slope distance between eave and ridgeline or the pressure demand ratio defined in Section 2.1.1. This transformation is unnecessary here since the limit state function in Eq. (4.4) can be applied to roof sheathing and to the other load path connections separately, and a composite fragility function can be constructed from the two sets of results as follows:

1. For $n$ randomly sampled realizations of roof geometry and wind direction, compute $n$ values of roof sheathing $\bar{C}_p$ as in Section 4.4.1 and $n$ values of roof structure $\bar{C}_p$ as in Section 4.4.2.

2. For $n$ samples of roof sheathing resistance, evaluate Eq. (4.4) as a function of roof sheathing $\bar{C}_p$ to obtain $n$ sheathing failure wind speeds $V_s$.

3. Draw $n$ samples of resistance $R_0$ for each of the other load path connections, excluding roof sheathing; reformulate $R_0$ as an equivalent distributed resistance $R$ according to Eq. (4.5), where $s_r$ is replaced by the applicable connector spacing.

4. Find the minimum connection resistance $R_{\min}$ in each realization and evaluate Eq. (4.4) as a function of roof structure $\bar{C}_p$ to obtain $n$ failure wind speeds $V_m$ for the main wind force resisting system.

5. Compute $V$ as the minimum of $V_m$ and $V_s$ in each realization and develop the fragility function from the normalized cumulative distribution of $V$.

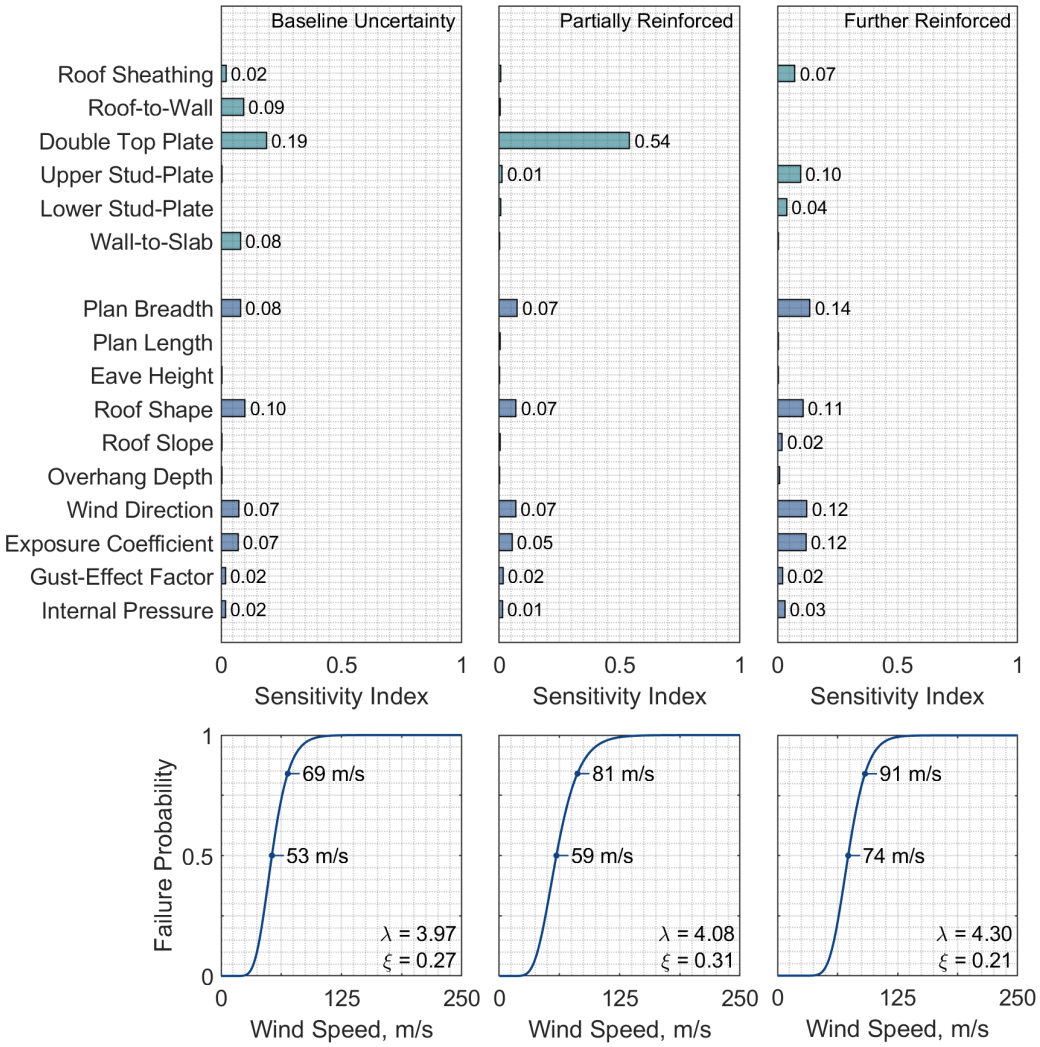


**Figure 4.11.** Sensitivity analysis of load path wind performance for a single-story home with a slab-on-grade foundation. Results are based on 6,000 random samples. Fragility function annotations indicate the 50th and 84th percentile failure wind speeds.

The results in Figure 4.11 are based on this procedure. The importance proportions of the connection resistances are largely unchanged relative to Figure 4.3. In both analyses, $S_i$ may be thought of as a latent variable that reflects both the frequency of failure in a connection and the variance in that connection's resistance. The results suggest that the uncertainty associated with aerodynamics is contributed almost entirely by roof plan breadth, roof shape, and wind direction in roughly equal measure.

The importance of plan breadth may come as a surprise in light of the results presented in Figure 4.7, in which $\bar{C}_p$ is definitively insensitive to plan breadth. In this analysis of performance, plan breadth — which is equivalent to roof member span — exercises influence on the resistance side by means of Eq. (4.5). By determining the extent of the roof-to-wall tributary area, plan breadth influences the total uplift force transferred to the load path. Roof slope, by contrast, is found to be relatively unimportant in these system-level cases. Is this always true? It was determined in the preceding two sections that roof slope is a leading aerodynamic factor for roof sheathing performance but an inconsequential one for the roof-to-wall connection. These findings imply that the importance of roof slope to system-level performance is contingent on how likely it is that roof sheathing will fail before any other load path connection. Since the roof sheathing connection is relatively strong in these example cases, roof slope exerts little influence, with $S_i$ rising to 0.02 only in the 'further reinforced' case, when the roof sheathing connection becomes the second-most likely failure point. [19]

### 4.5. Summary

The sensitivity analyses conducted in this chapter have considered a detailed set of structural and aerodynamic factors that characterize low-rise, wood-frame buildings in order to cast light on the major and minor contributors to uncertainty in wind vulnerability. Beyond the specific cases analyzed here, the approach demonstrated in this chapter may be applied to any connection or system of connections to apportion wind performance uncertainty to the underlying factors. It should be kept in mind that the analysis results are only necessarily valid within the bounds of the model

[19] From the results in Figure 4.3, roof sheathing failure controls in about 23% of outcomes in this case, a distant second to the upper stud-plate connection which controls 60% of the time.

assumptions. Other modeling approaches, such as defining wind vulnerability in terms of lateral pressures as well as uplift, may lead to different conclusions about parameter importance. Sensitivity behavior is also a function of the damage state of interest, such as how many panels must be removed to constitute roof sheathing failure. As with any sensitivity analysis, the results are useful only as far as the input parameter set and the assigned probability distributions accurately represent the facts on the ground. Care must be exercised to ensure all potentially important factors are included and that the distribution of each factor does not materially overstate or understate its uncertainty.

As the preceding discussion has suggested at several points, a central motivation behind the work described in this chapter is the development of a resource for post-event field study and forensic analysis. The primary novel contribution of this work is the integration of sensitivity and fragility analysis in a way that elucidates how much uncertainty various factors impart to a fragility function. Furthermore, the $\bar{C}_p$ regression model embedded within the analysis method allows uncertainty in wind performance to be traced back to the fundamental aerodynamic characteristics rather than to a probabilistic model of external pressure based on design values. By identifying the factors that drive uncertainty in performance, the method provides a basis for setting field data collection priorities that can be iteratively updated as epistemic uncertainties are removed. Such an approach, whereby fragilities are optimized by strategic field observation, could serve as a useful analytical aid to wind speed estimation.

# Chapter 5

## Concluding Summary

This dissertation has aimed to develop a new probabilistic modeling framework for studying wind vulnerability in light wood-frame buildings — a framework that is computationally practical and adaptable to numerous buildings and that takes accounts of an expansive array of building characteristics. Separating wind vulnerability into the major categories of structural and aerodynamic vulnerability, the framework directly examines the influence of various structural factors on wind uplift resistance, the influence of various aerodynamic factors on wind uplift load intensity, and the combined influence of structural and aerodynamic factors on wind performance. The central task of this effort has been the development of a method — or more generally, the articulation of a perspective on evaluating wind vulnerability. In the preceding chapters, this perspective has been sketched out for select analysis cases as illustrations. Certain general conclusions may be drawn from these results. The study of aerodynamic factors in Section 4.3, for example, supports the inference that roof shape exercises more influence on roof structure uplift intensity than roof slope, but that roof sheathing uplift intensity is largely determined by roof slope with far less influence from roof shape. But many other findings are more case-dependent. As with any probabilistic analysis, the results are tied to the distributions one assumes for the model parameters. Drawing broadly applicable conclusions about wood-frame wind vulnerability has been the minor focus of this work; demonstrating the usefulness of a method that can be applied to any number of specific cases has been the major focus.

*Areas of Application*

The analysis framework and its constituent models lend themselves to several areas of application. Practical considerations that shaped the development of the framework include the following:

1. Wind-resistant design: the resistance modeling approach provides a consistent way to identify structural weaknesses, quantify relative failure rates, and estimate system-level wind uplift resistance in numerous wood-frame load paths; new prescriptive designs can be evaluated to ensure acceptable levels of wind resistance.

2. Strategic retrofitting: by revealing characteristic weaknesses in the load path, the resistance model can offer guidance in making cost-effective retrofit decisions.

3. Dimensionality reduction: the proposed aerodynamic vulnerability index presents itself as an intuitive way to condense roof shape, roof slope, eave height, and other attributes into a single latent variable; this index, and others like it, could make high-dimensionality wind performance datasets more amenable to statistical inference.

4. Field data collection: variance-based sensitivity analysis can rapidly identify building characteristics that contribute substantial uncertainty to wind performance; analysis output can advise post-event field personnel of the most important perishable data to collect.

5. Wind speed estimation: the culmination of the framework is the sensitivity analysis of fragility functions, whereby the variance in a fragility function can be traced back to the fundamental structural and aerodynamic factors; in conjunction with prioritized data collection, the integration of sensitivity and

fragility analysis can support wind speed estimation efforts by providing field personnel with a likely range of failure wind speeds that continually recalculates as observations are entered.

*Recommendations for Future Work*

The wind vulnerability framework can be strengthened by additional validation and further development of the underlying resistance and load models. With respect to the structural resistance model, the following points merit attention:

1. Experimental uplift data for certain load path connections are sparse or altogether unavailable. Dedicated tests of wall sheathing edge-nail connections and various wall-to-foundation connections are especially needed to validate the adopted capacity models.

2. Testing of complete load paths, encompassing various common archetypes, is necessary to validate the assumptions involved in system resistance evaluation and to guide incorporation of load-sharing behavior and other nonlinearities into the model.

3. Contingent on the results of experimental testing, existing capacity models may require refinement, and new capacity models may need to be introduced if testing reveals failure modes not presently considered in the model. At the same time, any new capacity models must remain within certain limits of computational expense to keep the method serviceable for its intended applications.

4. Generalization of the model to take account of both the vertical and lateral load paths would improve the absolute accuracy of system resistance estimates.

Similarly, the wind load modeling approach would benefit from the following efforts:

5. As with resistance, a more robust definition of aerodynamic vulnerability would include lateral loads as well as uplift. Evaluating lateral wind pressures in conjunction with lateral load path resistance would support more accurate predictions of wind performance.

6. Additional wind tunnel testing of building models with complex roofs, and especially models with common features like large porch overhangs, would enable the training of more powerful regression models and broaden the predictive range of the aerodynamic vulnerability method.

7. Model predictions presently assume isolated buildings. Wind tunnel data for non-isolated buildings could be leveraged to take approximate account of the effect of neighboring structures.

8. A more comprehensive accounting of building features could be attained by resolving the statistical model of internal pressure into observable characteristics, such as the number of doors and windows and levels of impact protection.

9. Application of the vulnerability model to populations of buildings would be aided by the development of a computer-vision utility to automate geometry data collection and processing.

10. The suggested formulation of the aerodynamic vulnerability index — the product of the 50th and 90th percentile values of uplift intensity $\bar{C}_p(\theta)$ — remains to be validated.

The recommendations above outline a few directions in which the present work may be expanded and improved. There are undoubtedly others. The desire and expectation for this work is that it would serve the wind engineering research community well in its present form, and even more that it would spur the development of new resources

for understanding wind performance in wood-frame structures, to the end of building stronger homes and preserving life.

References

Alhawamdeh, B. and Shao, X. (2020) "Uplift Capacity of Light-Frame Rafter to Top Plate Connections Applied with Elastomeric Construction Adhesives," *Journal of Materials in Civil Engineering*, 32(5), 04020078.

American Concrete Institute (2014) *Building Code Requirements for Structural Concrete*, ACI 318-14, American Concrete Institute, Farmington Hills, Michigan.

American Wood Council (2018) *National Design Specification for Wood Construction*, American Wood Council, Leesburg, Virginia.

Amini, M. O. and van de Lindt, J. W. (2014) "Quantitative Insight into Rational Tornado Design Wind Speeds for Residential Wood-Frame Structures Using Fragility Approach," *Journal of Structural Engineering*, 140(7), 04014033.

Bhattacharjee, G. and Baker, J. W. (2021) "Using Global Variance-Based Sensitivity Analysis to Prioritise Bridge Retrofits in a Regional Road Network Subject to Seismic Hazard," *Structure and Infrastructure Engineering*, 19(2), 164–177.

Bre, F., Gimenez, J. M., and Fachinotti, V. D. (2018) "Prediction of Wind Pressure Coefficients on Building Surfaces Using Artificial Neural Networks," *Energy and Buildings*, 158, 1429–1441.

Canfield, L. R., Niu, S. H., and Liu, H. (1991) "Uplift Resistance of Various Rafter-Wall Connections," *Forest Products Journal*, 41(7–8), 27–34.

Chen, Y., Kopp, G. A., and Surry, D. (2003) "Prediction of Pressure Coefficients on Roofs of Low Buildings Using Artificial Neural Networks," *Journal of Wind Engineering and Industrial Aerodynamics*, 91(3), 423–441.

Cheng, J. (2004) "Testing and Analysis of the Toe-Nailed Connection in the Residential Roof-to-Wall System," *Forest Products Journal*, 54(4), 58–65.

Cremen, G. and Baker, J. W. (2021) "Variance-Based Sensitivity Analyses and Uncertainty Quantification for FEMA P-58 Consequence Predictions," *Earthquake Engineering and Structural Dynamics*, 50(3), 811–830.

Cunningham, T. P. (1993) "Roof Sheathing Fastening Schedules for Wind Uplift," American Plywood Association, Tacoma, Washington.

Datin, P. L., Prevatt, D. O., and Pang, W. (2011) "Wind-Uplift Capacity of Residential Wood Roof-Sheathing Panels Retrofitted with Insulating Foam Adhesive," *Journal of Architectural Engineering*, 17(4), 144–154.

Dev Sarma, H., Zisis, I., and Matus, M. (2023) "Effect of Roof Shape on Wind Vulnerability of Roof Sheathing Panels," *Structural Safety*, 100, 102283.

Ding, Z., Zhang, W., and Zhu, D. (2022) "Neural Network-Based Wind Pressure Prediction for Low-Rise Buildings with Genetic Algorithm and Bayesian Optimization," *Engineering Structures*, 260, 114203.

Edmonson, W. C., Schiff, S. D., and Nielson, B. G. (2012) "Behavior of Light-Framed Wood Roof-to-Wall Connectors Using Aged Lumber and Multiple Connection Mechanisms," *Journal of Performance of Constructed Facilities*, 26(1), 26–37.

Ellingwood, B. R., Rosowsky, D. V., Li, Y., and Kim, J. H. (2004) "Fragility Assessment of Light-Frame Wood Construction Subjected to Wind and Earthquake Hazards," *Journal of Structural Engineering*, 130(12), 1921–1930.

Ellingwood, B. R. and Tekie, P. B. (1999) "Wind Load Statistics for Probability-Based Structural Design," *Journal of Structural Engineering*, 125(4), 453–463.

Enajar, A., Nassef, A., and El Damatty, A. (2023) "Reliability of Toe-Nail Connections in Gable Roof Houses Under Uplift Wind Loads," *Engineering Structures*, 274, 115199.

Fernández-Cabán, P. L. and Masters, F. J. (2018) "Upwind Terrain Effects on Low-Rise Building Pressure Loading Observed in the Boundary Layer Wind Tunnel," DesignSafe Data Depot.

Fernández-Cabán, P. L., Masters, F. J., and Phillips, B. M. (2018) "Predicting Roof Pressures on a Low-Rise Structure from Freestream Turbulence Using Artificial Neural Networks," *Frontiers in Built Environment*, 4, 68.

Forest Products Laboratory (2021) *Wood Handbook: Wood as an Engineering Material*, General Technical Report 282, Forest Service, United States Department of Agriculture, Madison, Wisconsin.

Fusco, G. and Zhu, J. (2023) "Personalized Vulnerability Assessment of Customized Low-Rise Wood-Frame Residential Structures Under Hurricane Wind Loads: A Flexible Scenario-Based Simulation Approach," *ASCE-ASME Journal of Risk and Uncertainty in Engineering Systems, Part A: Civil Engineering*, 9(3), 04023023.

Gan Chowdhury, A., Zisis, I., Irwin, P., Bitsuamlak, G., Pinelli, J., Hajra, B., and Moravej, M. (2017) "Large-Scale Experimentation Using the Twelve-Fan Wall of Wind to Assess and Mitigate Hurricane Wind and Rain Impacts on Buildings and Infrastructure Systems," *Journal of Structural Engineering*, 143(7), 04017053.

Gavalda, X., Ferrer-Gener, J., Kopp, G. A., and Giralt, F. (2011) "Interpolation of Pressure Coefficients for Low-Rise Buildings of Different Plan Dimensions and Roof Slopes Using Artificial Neural Networks," *Journal of Wind Engineering and Industrial Aerodynamics*, 99(5), 658–664.

Glorot, X. and Bengio, Y. (2010) "Understanding the Difficulty of Training Deep Feedforward Neural Networks," *Proceedings of the Thirteenth International Conference on Artificial Intelligence and Statistics*, 9, 249–256.

Guha, T. K. and Kopp, G. A. (2014) "Storm Duration Effects on Roof-to-Wall Connection Failures of a Residential Wood-Frame Gable Roof," *Journal of Wind Engineering and Industrial Aerodynamics*, 133, 101-109.

Henderson, C., Huff, T., and Bouton, G. (2021) "Structural Observations and Tornado Damage Mitigation Concepts: March 2020 Tennessee Tornadoes," *Practice Periodical on Structural Design and Construction*, 26(2), 05021001.

Ho, T. C. E., Surry, D., Morrish, D., and Kopp, G. A. (2005) "The UWO Contribution to the NIST Aerodynamic Database for Wind Loads on Low Buildings: Part 1, Archiving Format and Basic Aerodynamic Data," *Journal of Wind Engineering and Industrial Aerodynamics*, 93(1), 1–30.

Jones, D. T. (1998) "Retrofit Techniques Using Adhesives to Resist Wind Uplift in Wood Roof Systems," M.S. Thesis, Clemson University, Clemson, South Carolina.

Khaneghahi, M. H., Alembagheri, M., and Soltani, N. (2019) "Reliability and Variance-Based Sensitivity Analysis of Arch Dams During Construction and Reservoir Impoundment," *Frontiers of Structural and Civil Engineering*, 13(3), 526–541.

Lee, K. H. and Rosowsky, D. V. (2005) "Fragility Assessment for Roof Sheathing Failure in High Wind Regions," *Engineering Structures*, 27(6), 857–868.

van de Lindt, J. W. and Dao, T. N. (2009) "Performance-Based Wind Engineering for Wood-Frame Buildings," *Journal of Structural Engineering*, 135(2), 169–177.

Liu, D. C. and Nocedal, J. (1989) "On the Limited Memory BFGS Method for Large Scale Optimization," *Mathematical Programming*, 45, 503–528.

Masonry Standards Joint Committee (2013) *Building Code Requirements for Masonry Structures*, TMS 402-13, The Masonry Society, Longmont, Colorado.

Masoomi, H., Ameri, M. R., and van de Lindt, J. W. (2018) "Wind Performance Enhancement Strategies for Residential Wood-Frame Buildings," *Journal of Performance of Constructed Facilities*, 32(3), 04018024.

McDonald, J. R., Mehta, K. C., Smith, D. A., and Womble, J. A. (2009) "The Enhanced Fujita Scale: Development and Implementation," *Proceedings of the Fifth Forensic Engineering Congress*, Washington, D.C., 719–728.

Meddage, D. P. P., Ekanayake, I. U., Weerasuriya, A. U., Lewangamage, C. S., Tse, K. T., Miyanawala, T. P., and Ramanayaka, C. D. E. (2022) "Explainable Machine Learning to Predict External Wind Pressure of a Low-Rise Building in Urban-Like Settings," *Journal of Wind Engineering and Industrial Aerodynamics*, 226, 105027.

Mehlig, B. (2021) *Machine Learning with Neural Networks: An Introduction for Scientists and Engineers*, Cambridge University Press, Cambridge, United Kingdom.

Mehta, K. C. (2013) "Development of the EF-Scale for Tornado Intensity," *Journal of Disaster Research*, 8(6), 1034–1041.

Metwally, Z., Zeng, B., and Li, Y. (2022) "Probabilistic Behavior and Variance-Based Sensitivity Analysis of Reinforced Concrete Masonry Walls Considering Slenderness Effect," *ASCE-ASME Journal of Risk and Uncertainty in Engineering Systems, Part A: Civil Engineering*, 8(4), 04022051.

Mizzell, D. P. (1994) "Wind Resistance of Sheathing for Residential Roofs," M.S. Thesis, Clemson University, Clemson, South Carolina.

Morrison, M. J. and Kopp, G. A. (2011) "Performance of Toe-Nail Connections Under Realistic Wind Loading," *Engineering Structures*, 33(1), 69–76.

National Association of Home Builders Research Center (2002) "Roof Framing Connections in Conventional Residential Construction," Office of Policy Development and Research, United States Department of Housing and Urban Development, Washington, D.C.

Nilforoush, R., Nilsson, M., and Elfgren, L. (2017) "Experimental Evaluation of Tensile Behaviour of Single Cast-in-Place Anchor Bolts in Plain and Steel Fibre-Reinforced Normal and High-Strength Concrete," *Engineering Structures*, 147, 195–206.

Nocedal, J. (1980) "Updating Quasi-Newton Matrices with Limited Storage," *Mathematics of Computation*, 35(151), 773–782.

Peng, X., Yang, L., Gavanski, E., Gurley, K., and Prevatt, D. (2014) "A Comparison of Methods to Estimate Peak Wind Loads on Buildings," *Journal of Wind Engineering and Industrial Aerodynamics*, 126, 11–23.

Reed, T. D., Rosowsky, D. V., and Schiff, S. D. (1997) "Uplift Capacity of Light-Frame Rafter to Top Plate Connections," *Journal of Architectural Engineering*, 3(4), 156–163.

Riley, M. A. and Sadek, F. (2003) "Experimental Testing of Roof-to-Wall Connections in Wood-Frame Houses," NIST IR 6938, National Institute of Standards and Technology, Gaithersburg, Maryland.

Rittelmeyer, B. M. and Roueche, D. B. (2024) "Probabilistic Wind Uplift Resistance Framework for the Relative Evaluation of Wood-Frame Load Paths," *Engineering Structures*, 298, 116984.

Rosowsky, D. V. and Cheng, N. (1999) "Reliability of Light-Frame Roofs in High-Wind Regions II: Reliability Analysis," *Journal of Structural Engineering*, 125(7), 734–739.

Roueche, D. B., Nakayama, J. O., Kijewski-Correa, T., and Prevatt, D. O. (2024) "A Unified Multievent Windstorm Performance Testbed for Single-Family Residential Buildings," *Natural Hazards Review*, 25(2), 04023060.

Saltelli, A., Ratto, M., Andres, T., Campolongo, F., Cariboni, J., Gatelli, D., Saisana, M., and Tarantola, S. (2008) *Global Sensitivity Analysis: The Primer*, Wiley, Chichester, West Sussex, United Kingdom.

Shanmugam, B., Nielson, B. G., and Prevatt, D. O. (2009) "Statistical and Analytical Models for Roof Components in Existing Light-Framed Wood Structures," *Engineering Structures*, 31(11), 2607–2616.

Shao, S., Stathopoulos, T., Yang, Q., and Tian, Y. (2018) "Wind Pressures on 4:12 Sloped Hip Roofs of L and T-Shaped Low-Rise Buildings," *Journal of Structural Engineering*, 144(7), 04018088.

Smith, D. A., Morse, S. M., and Mehta, K. C. (2017) "Wind Engineering Research Field Laboratory Selected Datasets for Comparison to Model-Scale, Full-Scale, and Computational Fluid Dynamics Simulations," Wind Science and Engineering Research Center, Texas Tech University, Lubbock, Texas.

St. Pierre, L. M., Kopp, G. A., Surry, D., and Ho, T. C. E. (2005) "The UWO Contribution to the NIST Aerodynamic Database for Wind Loads on Low Buildings: Part 2, Comparison of Data with Wind Load Provisions," *Journal of Wind Engineering and Industrial Aerodynamics*, 93(1), 31–59.

Standohar-Alfano, C. D. and van de Lindt, J. W. (2016) "Tornado Risk Analysis for Residential Wood-Frame Roof Damage Across the United States," *Journal of Structural Engineering*, 142(1), 04015099.

Standohar-Alfano, C. D., van de Lindt, J. W., and Ellingwood, B. R. (2017) "Vertical Load Path Failure Risk Analysis of Residential Wood-Frame Construction in Tornadoes," *Journal of Structural Engineering*, 143(7), 04017045.

Sutt, E. G. (2000) "The Effect of Combined Shear and Uplift Forces on Roof Sheathing Panels," Ph.D. Dissertation, Clemson University, Clemson, South Carolina.

Szilagyi, N. E. M. (2022) "Effective Wind Area for the Design of Roof Sheathing Under Wind Loading," M.S. Thesis, University of Western Ontario, London, Ontario, Canada.

Tarantola, S., Gatelli, D., and Mara, T. A. (2006) "Random Balance Designs for the Estimation of First Order Global Sensitivity Indices," *Reliability Engineering and System Safety*, 91(6), 717–727.

Tian, J., Gurley, K. R., Diaz, M. T., Fernández-Cabán, P. L., Masters, F. J., and Fang, R. (2020) "Low-Rise Gable Roof Building Pressure Prediction Using Deep Neural Networks," *Journal of Wind Engineering and Industrial Aerodynamics*, 196, 104026.

Wan, H., Todd, M. D., and Ren, W. (2017) "Statistical Framework for Sensitivity Analysis of Structural Dynamic Characteristics," *Journal of Engineering Mechanics*, 143(9), 04017093.

Weng, Y. and Paal, S. G. (2022) "Machine Learning-Based Wind Pressure Prediction of Low-Rise Non-Isolated Buildings," *Engineering Structures*, 258, 114148.

Weng, Y. and Paal, S. G. (2023) "Physics-Informed Few-Shot Learning for Wind Pressure Prediction of Low-Rise Buildings," *Advanced Engineering Informatics*, 56, 102000.

Wind Science and Engineering Center (2006) "A Recommendation for an Enhanced Fujita Scale," Revision 2, Texas Tech University, Lubbock, Texas.